Dynamics of Cellular Communities: Insights from Antibiotic-Induced Biofilms, Self-Replicating Oscillators, and Spatially-Extended Communities

by

Wen Yu

A dissertation submitted in partial fulfillment
of the requirements for the degree of
Doctor of Philosophy
(Physics)
in The University of Michigan
2017

Doctoral Committee:

        Assistant Professor Kevin Wood, Chair
        Professor Charles R. Doering
        Professor Jens-Christian D. Meiners
        Assistant Professor Qiong Yang
        Professor Michal R. Zochowski

Wen Yu

ywenv@umich.edu

ORCID iD: 0000-0002-8128-2016

ACKNOWLEDGEMENTS

I would first like to express my sincere gratitude to my academic advisor, Kevin Wood, for his support and guidance of my doctoral study, for his patience, immense knowledge and encouragement. It has been an honor to be his first graduating Ph.D. student. I appreciate his contributions of time, ideas and funding to make my Ph.D. experience productive and rewarding.

I would also like to thank my fellow lab-mates Kelsey Hallinen, Ziah Dean, Max De Jong, Jason Karslake, Jeff Maltas and many other rotating and undergraduate students in the Wood lab for their cooperation, feedback and friendship. It was great working with all of you during last four years.

Finally, I am grateful to my mother Qin Shen and my dad Shunxi Yu, for giving birth to me, raising me and inspiring me to study abroad for five years. They have provided endless love, moral and emotional support in my life. I am also grateful to my other family members and friends who have encouraged me along the way, despite the long distance between us. This accomplishment would not have been possible without them.

The work in Chapter II is contained, at least in part, in the following: Yu, W. and Wood, K., Synchronization and phase redistribution in self-replicating populations of coupled oscillators and excitable elements, Phys. Rev. E, 91, 062708 (2015).

The work in Chapter III is contained, at least in part, in the following: Yu, W.,

Hallinen, K., and Wood, K., Interplay between antibiotic efficacy and drug-induced lysis underlie enhanced biofilm formation at subinhibitory drug concentrations, In preparation, 2017.

TABLE OF CONTENTS

LIST OF FIGURES

ix

LIST OF TABLES

Table

ABSTRACT

Collective behavior is a fascinating phenomenon occurring at many scales in biology. From flocking of birds to synchronization in neural populations, examples abound where local interactions give rise to "macroscopic", often counterintuitive behavior, at the level of the community. In this thesis, I investigate community behavior in three distinct systems using a combination of theoretical and experimental approaches. The work spans a broad range of topics inspired by dynamics in microbial communities. In Chapter II, we provide a comprehensive theoretical study of synchronization in coupled oscillators, a topic that is among the most widely studied in dynamical systems. However, while past work has focused almost exclusively on populations of a fixed size, I introduce a new model of self-dividing oscillator populations that exhibits a remarkable range of synchronization phenomena as growth rate is varied. Chapter III describes a largely experiment-driven effort to understand a specific and counterintuitive phenomenon: the promotion of microbial community (biofilm) growth by low doses of antibiotic drugs in a medically relevant bacterial species, *E. faecalis*. We show that for cell wall synthesis inhibitors–which have for decades been among the most widely prescribed classes of antibiotics–low doses stimulate cell lysis and are associated with an increase in extracellular DNA, long believed to be an important structural component of biofilms. We also develop a simple mathematical model that highlights the interplay between the toxicity of the drug and

the "beneficial" effects of cell lysis and can be used to predict the impact of various chemical perturbations that impact optimal biofilm growth. Finally, Chapter IV is devoted to ongoing work on spatial pattern formation in two bacterial species, *E. coli* and *E. faecalis*, exhibiting cooperative antibiotic resistance via the production of a community good–an enzyme that targets and degrades antibiotics. The work draws on previous theoretical models to predict pattern formation in simple (non-cooperative) populations, which we quantify using customized experimental tools for quantitatively characterizing colony growth over time and space. In addition, we observe a range of new pattern-formation phenomena driven, in part, by the interplay between cell motility, cooperation, and density-dependent cell growth.

CHAPTER I

Introduction

Collective behavior is an interesting and important phenomenon occurring at many scales in biology [1]. From a city of people or a flock of birds to a swarm of insects or microbial biofilm communities, examples abound where local interactions give rise to group properties in nature. For example, ants and honey bees develop a unique self-organized society in order to work and live together in diverse environments, while single cell and molecular level studies continue to uncover new social behavior [2] of microbial collectives. In many cases, their ability to survive and evolve may come not only from individual adaption to the environment, but also from coordination and cooperation amongst individuals. These collective phenomena underlie fascinating and robust biological behavior while also inspiring new avenues for theoretical work at the interface of statistical physics [3], dynamical systems [4], and microbiology [5].

In this thesis, I investigate community behavior in three distinct systems using a combination of theoretical and experimental approaches. The work spans a broad range of topics inspired by dynamics in microbial communities, though the focus and goals of the investigations vary dramatically. More specifically, Chapter II is devoted to a purely theoretical study of synchronization in coupled oscillators, a

topic that is among the most widely studied in dynamical systems. However, while past work has focused almost exclusively on populations of a fixed size, I introduce a new model of self-dividing oscillator populations that exhibits a remarkable range of synchronization phenomena as growth rate is varied. The goal of this work is not to model a specific microbial system, but rather to investigate the dynamics born from coupling between growth and synchronization in a minimal model. By contrast, Chapter III describes a largely experiment-driven effort to understand a specific and counterintuitive phenomenon: the promotion of microbial community (biofilm) growth by low doses of antibiotic drugs in a medically relevant bacterial species, *E. faecalis*. We show that for cell wall synthesis inhibitors–which have for decades been among the most widely prescribed classes of antibiotics–low doses stimulate cell lysis and are associated with an increase in extracellular DNA, long believed to be an important structural component of biofilms. We also develop a simple mathematical model that highlights the interplay between the toxicity of the drug and the "beneficial" effects of cell lysis and can be used to predict the impact of various chemical perturbations that impact optimal biofilm growth. Finally, Chapter IV is devoted to ongoing work on spatial pattern formation in two bacterial species, *E. coli* and *E. faecalis*, exhibiting cooperative antibiotic resistance via the production of a community good–an enzyme that targets and degrades antibiotics. The work draws on previous theoretical models to predict pattern formation in simple (non-cooperative) populations, which we quantify using customized experimental tools for quantitatively characterizing colony growth over time and space. In addition, we observe a range of new pattern-formation phenomena driven, in part, by the interplay between cell motility, cooperation, and density-dependent cell growth.

In what follows, I provide a brief introduction to each topic and outline the struc-

ture of the thesis.

Chapter II

In nature, collective and coherent groups can generate periodic motion due to weak interactions amongst individuals, a phenomenon called synchronization. In many synchronizing systems–including fireflies or coupled lasers–synchronization occurs in populations of a fixed size. However, if we look at microbial systems, the timescale of oscillations may often be comparable with timescale of whole population growth, intuitively coupling oscillator phase and cell division. In this chapter, we introduce a minimal model of both phase dependent and phase independent population growth in coupled oscillators and excitable systems. We demonstrate how this coupling can lead to a wide range of dynamical behavior, including bistability between oscillatory and asynchronous states, as population growth is modulated.

Chapter III

One of the most striking and important examples of collective behavior occurs in microbial biofilms. Biofilms are densely packed communities of bacterial cells that stick and grow on surfaces and embedded within self-secreted extracellular polymer substance (EPS). In 1991, Lawrence group firstly used confocal laser scanning microscopy to examine hydrated biofilms and found more than 70% of the structure is constitutive of EPS and space [6]. Since then, biofilms have been a subject of intense research interest, in part because they exhibit a wide range of remarkable behavior, including long-range metabolic codependence [7] and electrical signaling [8, 9, 10], phenotypic phase variation [11] and spatial heterogeneity [12], strong ecological competition [13], and multiple types of cooperative behavior, including collective resistance to antimicrobial therapy [14, 15, 16]. Heterogeneity in physiological state and spatial structure has been implicated in bacterial tolerance in biofilms, which

3

ultimately cause bacteria in biofilms to be more resistant to antibiotics than plank-
tonic cells in liquid culture [17]. Biofilms become leading causes of life-threatening
infections which are severe to human lives due to this fundamental feature. Surpris-
ingly, however, recent work has shown that subminimal inhibitory concentrations
(sub-MICs) of some antibiotics were found to promote biofilm formation [18]. Unfor-
tunately, much is still unknown about how low drug doses affect the composition and
spatial structure of the biofilms of many species, especially for *Enterococcus faecalis*,
which remains among the leading causes of hospital acquired infections because of
its ability to form biofilms [19, 20]. In this chapter, we investigated the effects of
sub-MICs of cell wall synthesis inhibitors, for example β-lactam ampicillin, on the
formation of *E. faecalis* biofilms. We found that inhibitors of cell wall synthesis, but
not other classes of antibiotics, induce biofilm formation associated with increased
cell lysis and increased extracellular DNA (eDNA), a known conduit for biofilm for-
mation. Using a range of experimental approaches–from bulk assays to confocal
microscopy–we quantify this effect and develop a simple mathematical model that
predicts changes in biofilm formation due to external perturbations, including the
degradation of eDNA or the addition of cell lysis inhibitors.

Chapter IV

In Chapter IV, we investigate spatial pattern in bacterial populations grown on
agar plates. By using a customized, scanner-based experimental set-up along with
fluorescence microscopy, we were able to measure and quantify the growth of colonies
and track their emergence over time under different antibiotic stresses. In simple non-
cooperative populations, we observe the expected genetic demixing phenomenon due
to genetic drift and reduced population size at the frontier. On the other hand,
mixed populations of sensitive and resistant cells exhibited cooperation and density-

dependence not captured by previous models. In this chapter, we will discuss our ongoing work to quantify these processes in *E. coli* and *E. faecalis* and to adapt theoretical models to account for new spatial phenomena.

Synchronization and Phase Redistribution in Self-replicating Populations of Coupled Oscillators and Excitable Elements

2.1 Introduction

Synchronization phenomena in collections of coupled oscillators and excitable elements are widely studied in statistical physics [21, 22, 23, 24, 1], in part because they represent prototypical nonequilibrium phase transitions exhibiting time-translational symmetry breaking. In addition to their theoretical value, models of synchronization offer insight into a diverse collection of physical, chemical, and biological phenomena [1, 25], ranging from bulk oscillations in chemical reactions to phenotypic or behavioral synchronization in populations of living organisms.

Synchronization plays a particularly important role in biological systems, where coherent oscillations may serve biological or behavioral function. Examples abound, including rhythmic flashing of fireflies [23], coherent behavior of neurons in human neocortex [26] or primate retina [27], circadian oscillations in cyanobacteria [28, 29, 30], vertebrates [31] and mammals [32, 33], and synchronized cell division [34] or protein dynamics [35, 36] in populations of single-cell organisms. In many of these systems, the timescales of the oscillations are well-separated from the timescales of population growth, allowing one to neglect its effects on macroscopic synchrony. In turn, the vast majority of theoretical studies on coupled oscillators have dealt with

a fixed population size. However, this restriction may not always be applicable, as an increasing number of systems have been shown to exhibit oscillations that occur on similar timescales as population growth [37, 38, 34, 35, 36, 28, 29, 30]. This overlap in timescales raises the question of how population growth might affect synchronization, given that the population wide distribution of oscillator phases may be strongly coupled to the growth process.

Several recent studies have illustrated the complex synchronization phenomena that can occur in growing populations. In bacteria populations, an elegant series of experimental studies has recently laid the groundwork for synthetic sensors and logical programming in living systems based on tunable oscillations in growing populations [35, 36]. These studies highlight a wide range of fascinating spatiotemporal behavior. However, the effect of growth rate on the dynamics of these populations is not addressed in detail. In addition, recent theoretical work [39] has demonstrated a rich collection of dynamical behaviors in small chains of coupled oscillators gradually increasing in number. In this work, by contrast, we focus on the large-population limit and the corresponding phase transitions to macroscopic oscillations. To our knowledge, this work is the first to systematically address how coupling between population growth and oscillator phase can effect synchronization.

Specifically, we explore the effects of population growth and the corresponding redistribution of phases on the synchronization properties of a simple class of models for both coupled oscillators and excitable elements. While the paradigmatic Kuramoto model has paved the way to much of our current understanding of synchrony [22, 24], oscillator models with discrete phases have gained increasing attention because of their relative mathematical simplicity [40, 41, 42, 43, 44, 45, 46, 47, 48, 49, 50, 51, 52, 53]. Here, we focus on these discrete phase models because they can be readily

modified to integrate oscillator growth and the potential phase dependence of the division and birth processes.

Using a combination of numerical simulations, mean field theory, and linear stability analysis, we find that the redistribution of phases induced by population growth can disrupt synchronization via either continuous (supercritical) or discontinuous (subcritical) transitions in both discrete phase oscillators and excitable elements. We observe a range of dynamical behaviors, including bistability between two asynchronous states or between asynchronous and oscillatory states, a switch between supercritical and subcritical transitions as growth is increased, the existence of asynchronous states with unequal phase distributions, or modulation of the bulk oscillation frequency. These results demonstrate that even in minimal models, the coupling between population growth and oscillator phase can profoundly affect synchronization and even lead to new dynamical states that do not exist in the absence of this coupling.

This chapter is divided into two sections, with the first devoted to discrete phase oscillators and the second to excitable, discrete phase systems. In Section 2.2.1, we briefly review the discrete phase oscillator model and extend it to capture population growth. In Section 2.2.2, we develop a mean field approximation, and in sections 2.2.3 and 2.2.4 we use linear stability analysis and numerical simulations to explore the effects of growth when division is independent of state or strongly state-dependent, respectively. In Section 2.3.1 we outline a model for growing populations of excitable elements, in Section 2.3.2 we describe numerical simulations of the model, and in Section 2.3.3 we use mean field theory and linear stability analysis to derive complete phase diagrams for the growing populations. We conclude with a discussion of the results in Section 2.4.

8

2.2 Discrete Phase Oscillators

2.2.1 Model for Growing Oscillator Populations

We will model an active oscillator as an m-state system governed by unidirectional transitions between states, $1 \to 2 \to 3... \to m \to 1 \to 2...$ [40]. The states represent a type of discretized phase, and formally, the state space of a single oscillator can be described by a phase variable $0 \leq \phi \leq 2\pi$ in the limit $m \to \infty$. For simplicity, we restrict ourselves here to finite m and study a discrete phase oscillator with the minimum number of states ($m = 3$) required to generate a Hopf bifurcation and, hence, macroscopic oscillations in a coupled population [41, 42, 43, 44]. In addition to their relative simplicity, these discrete phase models are often appropriate descriptions for biological or chemical systems, where the oscillations commonly occur on a discrete state space.

In the absence of coupling, each oscillator transitions irreversibly between states ($1 \to 2 \to 3 \to 1$) with a probability per unit time g, which sets the oscillator's intrinsic frequency. The model is therefore an example of a Markov chain. Coupling between oscillators is achieved by allowing these transition rates to depend on the fraction of the oscillators in each state; hence, g is replaced by a function Γ_i, which is the probability per unit time for a given oscillator to transition from state $i - 1$ to state i (with $i = 1, 2, 3 \pmod 3$). Γ_i also depends on a real parameter $a \geq 0$, which measures the strength of the coupling between oscillators (hence $\partial \Gamma_i / \partial a \geq 0$). While a number of nonlinear coupling functions have been used in previous studies [44, 50], for now we will leave the coupling function unspecified but explicitly note its dependence on the fraction of oscillators P_i in state i, $\Gamma_i = \Gamma_i(P_i)$. The primary requirement for this function is that it facilitates phase coherence between oscillators and leads to a Hopf bifurcation at a positive value of a. We discuss these

constraints in more detail in what follows.

In the mean field limit of all-to-all coupling, the fraction of oscillators P_i in state i is governed by the continuous time master equation,

$$\dot{P}_i = -P_i \Gamma_{i+1} + P_{i-1} \Gamma_i. \tag{2.1}$$

The total number of oscillators is conserved in this model ($\sum_i P_i = 1$), and the fixed point $P_i^* = 1/3$ becomes unstable via a Hopf bifurcation as long as

$$\frac{\Gamma_i'}{\Gamma_i} > 3, \tag{2.2}$$

above some critical value of $a \equiv a_c$ [50] . In Equation 2.2, $\Gamma \equiv \Gamma(x,a)\big|_{x=1/3}$ and $\Gamma_i' \equiv \frac{\partial \Gamma(x,a)}{\partial x}\big|_{x=1/3}$. For larger $a > a_c$, macroscopic oscillations occur. In what follows, we consider the class of oscillator models where Equation 2.2 is satisfied for some $a \geq a_c > 0$.

To incorporate population growth, we introduce two minimal mechanisms by which growth and oscillator phase may be coupled. First, we allow each oscillator in state i to give birth to a new oscillator with probability per unit time $\epsilon_i k$, with $\sum_i \epsilon_i = m = 3$. The dimensionless weighting factors ϵ_i couple the rate of division to the state of the oscillator, and k is a growth rate constant. In this work, we restrict our attention to two limiting cases: phase independent growth, $\epsilon_i = 1$, and strongly phase-dependent growth, $\epsilon_i = 3\delta_{ij}$, where δ_{ij} is the Kronecker delta. In the former case (Case 1), oscillators in all states are equally likely to divide, so division itself is independent of the state of the oscillator. In the latter case (Case 2), division can only occur for oscillators in state j. We choose $j = 1$ without loss of generality. This state dependence of division could be relevant in a number of biological settings, such as synchronization in cell division itself, where the oscillators in certain states–for example, those in certain stages of the cell cycle–divide

10

preferentially. State-dependence of division could also occur in oscillations of protein dynamics, as transcriptional and translational activity are often linked to the cell cycle [54, 55, 56, 57, 58].

Second, we allow the phase of the daughter oscillator to depend probabilistically on the state of the mother. Specifically, with each division, the new daughter oscillator has probability χ to be in the same state as the mother and a probability $(1 - \chi)/2$ to be in each of the two remaining states. This assumption could again be relevant in many biological applications, where cell division can lead to a repartitioning of intracellular contents, such as proteins, that may be fundamental to the oscillation [59, 60]. We stress that our goal here is not to incorporate biological details into a system-specific model, but rather to introduce state-dependent division and birth in a minimal model. While other rules for coupling single oscillator dynamics to division are possible, we will show below that the simple rules above lead to a rich collection of dynamical behaviors.

2.2.2 Mean Field Theory

To develop a mean field approximation for this model, we begin by writing evolution equations for N_i, the number of oscillators in state i, as

$$\dot{N_i} = -N_i\Gamma_{i+1} + N_{i-1}\Gamma_i +$$
$$\epsilon_i k N_i \chi + \frac{k}{2}(\epsilon_{i+1}N_{i+1} + \epsilon_{i-1}N_{i-1})(1 - \chi) \tag{2.3}$$

with $i = 1, 2, 3 \pmod 3$. The first two terms capture the nonlinear coupling between oscillators that drives synchronization, analogous to the two terms in Equation 2.1, while the latter two terms account oscillator division, as described in Section 2.2.1. Since the total number of oscillators $\sum_i N_i = N(t)$, we rewrite Equation 2.3 in terms

of P_i, the fraction of oscillators in state i, using $\dot{P}_i = \dot{N}_i/N - N_i\dot{N}/N^2$, to arrive at

$$
\dot{P}_i = -P_i\Gamma_{i+1} + P_{i-1}\Gamma_i + \epsilon_i k P_i \chi +
$$
$$
\frac{k}{2}(\epsilon_{i+1}P_{i+1} + \epsilon_{i-1}P_{i-1})(1-\chi) - P_i\frac{\dot{N}}{N}, \tag{2.4}
$$

where $\dot{N}/N = k\sum_j \epsilon_j P_j$ follows directly from Equation 2.3. The model is now fully specified by two differential equations (e.g. for $\dot{P}_1$ and $\dot{P}_2$) and the normalization condition $P_1 + P_2 + P_3 = 1$. Without loss of generality, we can set $g = 1$, which is equivalent to measuring time in units of g and replacing k with k/g; in what follows, we use k for economy of notation. Equation 2.4 provides a general mean field description valid in the limit of all-to-all coupling and can be solved numerically for any choice of parameters. To make further analytical progress, we now restrict our attention to the limiting cases of phase independent growth, $\epsilon_i = 1$, and strongly phase-dependent growth, $\epsilon_i = 3\delta_{ij}$.

2.2.3   Case 1: Division is independent of state

When division takes place independently of the state of each oscillator ($\epsilon_i = 1$), Equation 2.4 reduces to

$$
\dot{P}_i = -P_i\Gamma_{i+1} + P_{i-1}\Gamma_i - kP_i(1-\chi) +
$$
$$
\frac{k}{2}(P_{i+1} + P_{i-1})(1-\chi) \tag{2.5}
$$

Several things become apparent from inspection. First, for $\chi = 1$ (daughter oscillators are always in the same state as the mother), Equation 2.5 reduces to Equation 2.1. In this case, oscillator division leads to an exponentially increasing number of oscillators over time, but all synchronization properties–which depend on the fraction of oscillators in each state, not the total number–will remain unchanged. Second, it is clear that the asynchronous fixed point $P_i = 1/3$ is a solution to Equation 2.5 for all parameter values.

Figure 2.1: Top panels: values of successive maxima / minima of the time series $P_1(t)$ (black, dark) and $P_2(t)$ (red, light) for each value of the dimensionless growth k for model in Equation 2.5. Top left, $\chi = 0$; bottom left, $\chi = 1/3$; top right, $\chi = 2/3$; bottom right, $\chi = 1$. Bottom panel: order parameter q for $\chi = 0$ (light blue, lightest), $\chi = 1/3$ (black, darkest), $\chi = 2/3$ (dark blue, dark), and $\chi = 1$ (red, light). Different shapes represent different intrinsic oscillator frequencies ($g = 0.75$, circles; $g = 1$, crosses; $g = 1.5$, triangles). In all panels, $a = 20 > a_{c,0}$, $N_0 = 500$, initial conditions are given by $P_1 = 2/3$, $P_2 = 1/3$, and the coupling function $\Gamma_i = 1 + aP_i^2$.

To analytically explore the effects of division on oscillator synchrony, we linearize around the asynchronous fixed point; the corresponding Jacobian matrix, J, evaluated at the fixed point, is

$$J = \begin{pmatrix} -\frac{3}{2}(1-\chi)k - 2\Gamma + \frac{1}{3}\Gamma' & -\Gamma - \frac{1}{3}\Gamma' \\ \Gamma + \frac{1}{3}\Gamma' & -\frac{3}{2}(1-\chi)k - \Gamma + \frac{2}{3}\Gamma' \end{pmatrix}. \tag{2.6}$$

where Γ and Γ' are the coupling function and its derivative, respectively, evaluated at $P_i = 1/3$. The matrix J has complex conjugate eigenvalues $\lambda = \alpha \pm i\omega$, with

$$\begin{aligned} \alpha &= \frac{1}{2}\left(-3(1-\chi)k - 3\Gamma + \Gamma'\right) \\ \omega &= \frac{1}{2}\left(\sqrt{3}\Gamma + \frac{1}{\sqrt{3}}\Gamma'\right) \end{aligned} \tag{2.7}$$

which cross the imaginary axis at

$$k \equiv k_c = \frac{1}{3(1-\chi)}\left(-3\Gamma(a_c) + \Gamma'(a_c)\right), \tag{2.8}$$

where we have explicitly noted the dependence of Γ and Γ' on the critical value of the coupling, a_c. Equation 2.8 provides a relationship between the critical values of growth k_c and coupling a_c, which separate synchronous and asynchronous behavior. For $k = 0$, Equation 2.8 reduces to Equation 2.2. More generally, for $k > k_c$, the fixed point is stable and no oscillations occur; sufficiently fast population growth therefore disrupts otherwise synchronized populations. In addition, at the bifurcation point, the frequency of the oscillations is given by $\omega \equiv \omega_0 = \frac{1}{2}\left(\sqrt{3}\Gamma(a_c) + \frac{1}{\sqrt{3}}\Gamma'(a_c)\right)$ and is therefore expected to be modified by the addition of growth, which changes a_c.

To determine the nature of the bifurcation (subcritical or supercritical), we calculate the first Lyapunov coefficient, l_1. The sign of l_1, which is analogous to the coefficient of the third order term in the normal form for a Hopf bifurcation, is negative for supercritical and positive for subcritical Hopf bifurcations. For an n-dimensional dynamical system $\dot{x} = f(x, \epsilon)$ with an equilibrium point $x = x^H$ undergoing a Hopf

14

Figure 2.2: Top panels: values of successive maxima / minima of the time series $P_1(t)$ (black, dark) and $P_2(t)$ (red, light) for each value of the dimensionless growth rate k for model in Equation 2.5. Top left, $\chi = 0$; bottom left, $\chi = 1/3$; top right, $\chi = 2/3$; bottom right, $\chi = 1$. Bottom panel: order parameter q for $\chi = 0$ (light blue, lightest), $\chi = 1/3$ (black, darkest), $\chi = 2/3$ (dark blue, dark), and $\chi = 1$ (red, light). In all panels, $a = 4 > a_{c,0}$, $N_0 = 500$, $g = 1$, initial conditions are given by $P_1 = 2/3$, $P_2 = 1/3$, and the coupling function $\Gamma_i = e^{aP_i}$.
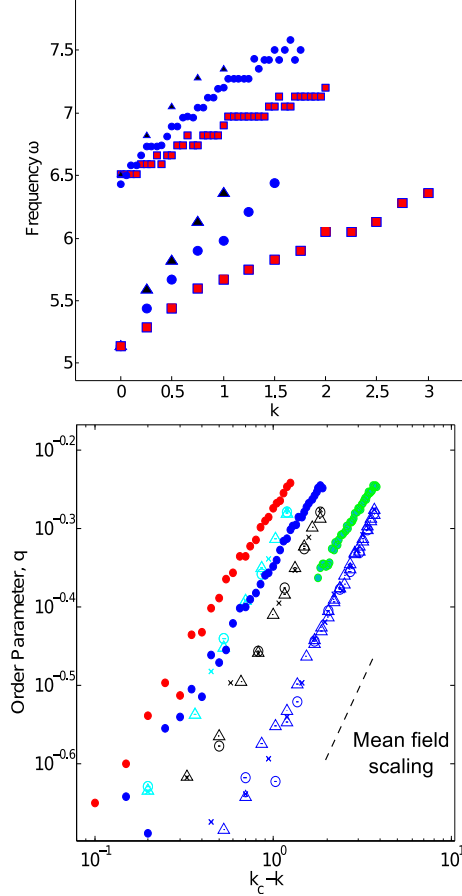
Figure 2.3: Upper panel: frequency ω of macroscopic oscillations for model in Equation 2.5, corresponding to the maximum peak of the power spectrum of $P_1(t)$ for $\chi = 0, 1/3, 2/3, 1$ (upper triangles, circles, and squares, respectively). Curves originating at $\omega \approx 6.5$ correspond to $\Gamma_i = e^{aP_i}$; curves originating at $\omega \approx 5.2$ correspond to $\Gamma_i = 1 + aP_i^2$. Lower panel: order parameter, q, as a function of $k_c - k$ near the critical point. Open shapes correspond to $\Gamma_i = 1 + aP_i^2$; small closed circles correspond to $\Gamma_i = e^{aP_i}$. Open shapes: $\chi = 0$ (light blue, leftmost), $\chi = 1/3$ (black, middle), $\chi = 2/3$ (dark blue, rightmost) at different intrinsic oscillator frequencies ($g = 0.75$, circles; $g = 1$, crosses; $g = 1.5$, triangles). Closed circles: $g = 1$ and $\chi = 0$ (blue, middle), $\chi = 1/3$ (red, leftmost), $\chi = 2/3$ (green, rightmost). In all panels, $N_0 = 500$ and initial conditions are given by $P_1 = 2/3$, $P_2 = 1/3$. $a = 20 > a_{c,0}$ for $\Gamma_i = 1 + aP_i^2$; $a = 4 > a_{c,0}$ for $\Gamma_i = e^{aP_i}$. Dashed line: mean field scaling $q \sim (k_c - k)^{1/2}$. Curves are shifted slightly to allow for visualization of all curves simultaneously.

bifurcation at parameter value $\epsilon = \epsilon^H$, l_1 can be calculated following the projection procedure in [61] as

$$
\begin{aligned}
l_1 = &\frac{1}{2\omega_0} Re[\langle p, C(q, q, \bar{q})\rangle - 2\langle p, B(q, A^{-1}B(q, \bar{q}))\rangle \\
&+ \langle p, B(\bar{q}, (2i\omega_0 I - A)^{-1}B(q, q))\rangle],
\end{aligned}
\tag{2.9}
$$

where $\langle ., . \rangle$ is the complex scalar product, I is the identity matrix, and p and q are the right and left eigenvectors, respectively, of the Jacobian $A = \frac{\partial f}{\partial x}|_{x=x^H}$ given by

$$
\begin{aligned}
Aq &= i\omega_0 q, \\
A^T p &= -i\omega_0 p.
\end{aligned}
\tag{2.10}
$$

The vectors are normalized so that $\langle p, q \rangle = 1$, and the functions $B(u, v)$ and $C(u, v, w)$ are multilinear, n-dimensional vector functions given by

$$
\begin{aligned}
B(u, v) &= \sum_{j,k=1}^{n} \frac{\partial^2 f(\psi, \epsilon^H)}{\partial \psi_j \partial \psi_k}\bigg|_{\psi=x^H} u_j v_k \\
C(u, v, w) &= \sum_{j,k,l=1}^{n} \frac{\partial^3 f(\psi, \epsilon^H)}{\partial \psi_j \partial \psi_k \partial \psi_l}\bigg|_{\psi=x^H} u_j v_k w_l.
\end{aligned}
\tag{2.11}
$$

Specifically, for the model in Equation 2.5, we find

$$
\begin{aligned}
q &= \left(\frac{-1 - i\sqrt{3}}{2\sqrt{2}}, \frac{1}{\sqrt{2}} \right), \\
p &= \left(-i\sqrt{\frac{2}{3}}, -\frac{3\sqrt{2} + i\sqrt{6}}{6} \right),
\end{aligned}
\tag{2.12}
$$

independent of the coupling function Γ. Following straightforward algebraic manipulations, we arrive at

$$
l_1 = \frac{\sqrt{3}}{4} \left(\frac{\Gamma''' - 6\Gamma''}{3\Gamma + \Gamma'} \right).
\tag{2.13}
$$

where primes indicate derivatives of the coupling function

$$
\begin{aligned}
\Gamma &\equiv \Gamma(x, a_c)\big|_{x=1/3}, \\
\Gamma' &\equiv \frac{\partial \Gamma(x, a_c)}{\partial x}\big|_{x=1/3}, \\
\Gamma'' &\equiv \frac{\partial^2 \Gamma(x, a_c)}{\partial x^2}\big|_{x=1/3}, \\
\Gamma''' &\equiv \frac{\partial^3 \Gamma(x, a_c)}{\partial x^3}\big|_{x=1/3}.
\end{aligned}
\tag{2.14}
$$

Interestingly, Equation 2.13 suggests that the nature of the Hopf bifurcation is determined by the magnitude of the derivatives of the coupling function at the critical point. Because increasing growth rate, k, will change the critical value a_c, it is possible for growth to not only change the coupling required for synchronization, but also the nature of the transition itself. For example, if we make the physically realistic assumptions that $\Gamma_i \geq 0$ and $\Gamma_i' \geq 0$, the condition $\Gamma''' = 6\Gamma''$ separates supercritical and subcritical transitions. To illustrate this point, in the next section we consider two specific examples of the coupling function and show that both supercritical and subcritical bifurcations are possible, depending on its derivatives.

2.2.3.1 Examples of supercritical and subcritical growth-induced bifurcations

In this section, we study two specific coupling functions to demonstrate the rich dynamics possible in this class of models. First, we consider a coupling of the form

$$
\Gamma(P_i, a) = 1 + a P_i^2,
\tag{2.15}
$$

which satisfies Equation 2.2 for $a > a_c \equiv 9$ in the absence of population growth. For nonzero growth rate k, we can rearrange Equation 2.8 to show the critical value a_c is increased to

$$
a_c = a_{c,0} + 9k(1 - \chi),
\tag{2.16}
$$

where $a_{c,0}$ is the critical coupling in the absence of growth. In a synchronized population ($a > a_{c,0}$), introducing population growth therefore quashes the macroscopic
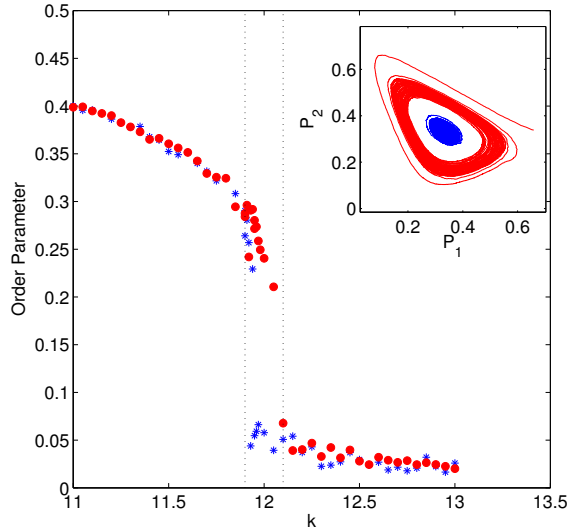
Figure 2.4: Order parameter q as a function of k for Equation 2.5 with $\Gamma_i = e^{aP_i}$ and $a = 6.75$. Simulations were run from two sets of initial conditions: $P_1 = 2/3, P_2 = 1/3$ (red, light) and $P_1 = 1/3, P_2 = 1/3$ (blue, dark), leading to different steady state behavior. Insets: phase portraits for $k = 12$ for each set of initial conditions. $\chi = 0$ and $N_0 = 5000$ for all points. Dashed lines indicate region of bistability.

oscillations when

$$k > k_c \equiv \frac{a - 9}{9(1 - \chi)}. \tag{2.17}$$

At the transition point, the frequency of oscillations is given by

$$\omega_0 = \frac{\sqrt{3}}{6}(a_c + 3) = \sqrt{3}\left(2 + \frac{3}{2}k_c(1 - \chi)\right). \tag{2.18}$$

Hence, for a fixed value of $k = k_c$, the frequency at the transition point decreases linearly with χ, eventually reaching the transition frequency $\omega_0 = 2\sqrt{3}$ of the non-dividing model. On the other hand, for a fixed value of $a > a_{c,0}$, the frequency at the transition point approaches the value $\omega = \frac{\sqrt{3}}{6}(a + 3)$, independent of χ, as k approaches k_c.

Finally, we can calculate the first Lyapunov coefficient, l_1, which depends on k,

as

$$l_1 = -\frac{9\sqrt{3}(1 + k(1 - \chi))}{4 + 3k(1 - \chi)}. \tag{2.19}$$

Hence, $l_1 < 0$ for all k and $0 \leq \chi \leq 1$, indicating that the bifurcation remains supercritical in the presence of population growth.

As a second example, we consider the coupling

$$\Gamma(P_i, a) = e^{aP_i}. \tag{2.20}$$

In the absence of growth, the model undergoes a Hopf bifurcation at $a = a_{c,0} = 3$. In the presence of growth, the critical value a_c increases and is given by the solution to

$$3k(1 - \chi) = (a - 3)e^{a/3}. \tag{2.21}$$

Equivalently, if we start with a synchronized population at a given value of $a > a_{c,0}$, the oscillations will be destroyed when $k > k_c \equiv (a-3)e^{a/3}/(3(1-\chi))$. The frequency at the transition point is given by

$$\omega_0 = \frac{(a_c + 3)e^{a/3}}{2\sqrt{3}}, \tag{2.22}$$

which increases when growth is introduced and $a_c > a_{c,0}$. Most interestingly, the first Lyapunov coefficient, l_1, is

$$l_1 = -\frac{\sqrt{3}(a_c - 6)a_c^2}{4(3 + a_c)}, \tag{2.23}$$

which changes sign at $a_c = 6$ (or equivalently, when $\Gamma''' = 6\Gamma'$). For small growth rates such that $a_{c,0} < a_c < 6$, the bifurcation between synchronous and asynchronous state is supercritical. However, for larger growth rates, $a_c > 6$ and the bifurcation becomes a subcritical, discontinuous transition. In this case, population growth–and the corresponding redistribution of oscillator phases–leads to a fundamentally different transition for sufficiently high growth rates.

To confirm these results numerically, we simulated growing populations of os-cillators using the Gillespie algorithm [62] for a wide range of k (growth rate), g (oscillator natural frequency), and χ (probability of daughter being in same state as mother). Unless otherwise noted, simulations were run starting with $N_0 = 500$ oscillators that are strongly coupled ($a > a_{c,0}$). For nonzero k, the total number of oscillators grows approximately exponentially, so computer memory limits simu-lations to relatively short time periods. To circumvent this limitation, we allowed simulations to run until the total number of oscillators reached $N_{max} = 10N_0$; when the number of oscillators exceeded N_{max}, we automatically reset the total number of oscillators to N_0 while preserving the fractional distribution of oscillator states. While this numerical procedure effectively underestimates the fluctuations observed in the oscillations, our goal is to approximate a thermodynamic limit $N \to \infty$, and even the modest starting number $N = 500$ yields relatively small fluctuations in macroscopic behavior.

After simulations have reached steady state, we visualize the dynamics by plot-ting the values of successive maxima / minima of the time series $P_1(t)$ (black, dark) and $P_2(t)$ (red, light) for each value of the dimensionless growth rate k (Fig-ures 2.1 and 2.2). We also calculated the synchronization order parameter $q = (\langle |Z - \langle Z \rangle_t|^2 \rangle_t)^{1/2}$, which was originally proposed in [45]. In this definition, $Z(t) = \frac{1}{N} \sum_j e^{i\theta_j(t)}$ is the (not yet averaged) Kuramoto order parameter [21, 24], $\theta_j = 2\pi k/3$, $k = (0, 1, 2)$ is the discretized phase of oscillator j, and angle brackets represent an average over time. The standard Kuramoto order parameter is not appropriate for models where rotational symmetry is absent and, consequently, non-oscillating steady states can lead to nonzero values of the order parameter, despite the absence of collective synchrony. As shown in [45], the order parameter q is akin to a gener-

alized standard deviation of $Z(t)$ and removes the bias due to a lack of rotational symmetry. Nonzero values of q correspond to synchronized, oscillatory states.

For $\Gamma_i = 1 + aP_i^2$ at $a = 20 > a_{c,0}$ (Figure 2.1) and $\Gamma_i = e^{aP_i}$ at $a = 4 > a_{c,0}$ (Figure 2.2), oscillations smoothly decrease in amplitude with increasing k, leading eventually to a completely asynchronous state. The value of the critical growth k is consistent with the linear stability analysis, Equation 2.17 and Equation 2.21; it increases with χ until, at $\chi = 1$, the oscillations are undisturbed by even large growth rates.

Our numerical simulations indicate that population growth affects not only global synchronization, but also the frequency of the macroscopic oscillations in the synchronized state. To explore this frequency dependence systematically, we calculated the power spectrum of the time series $P_1(t)$ for each simulation in steady state. Figure 2.3 (top panel) shows the frequency of the dominant peak in the power spectrum, which characterizes the frequency of the macroscopic oscillations. In both examples, increasing k leads to a monotonically increasing oscillation frequency until, at sufficiently high values of k, the macroscopic oscillations are no longer present.

Because these models are globally coupled and exhibit supercritical bifurcations, one expects that the order parameter should scale as $q \sim (k_c - k)^\beta$ near the critical point, with $\beta = 1/2$ the standard mean field scaling exponent. Indeed, we find that in our numerical simulations, the order parameter approximately follows mean field scaling near the critical point, independent of the value of χ or the specific coupling function chosen (Figure 2.3, bottom panel; note that we have slightly shifted the curves relative to one another so that each is visible). One would expect similar behavior for any choice of Γ_i where a supercritical transition occurs as k eclipses a critical value k_c.

By contrast, the transition becomes discontinuous when $\Gamma_i = e^{aP_i}$ and a is increased beyond $a = 6$. For example, at $a = 6.75$, growth induces a subcritical Hopf bifurcation (Figure 2.4), as indicated by the discontinuous drop in the order parameter and the corresponding bistability. Interestingly, in the bistable region, which we find to exist for $11.9 \leq k \leq 12.1$, synchronous oscillations co-exist with an asynchronous fixed point. For populations initiated with approximately uniform phase distributions, the system settles into a stable asynchronous state; for highly non-uniform distributions, the population undergoes stable oscillations indicative of synchrony (upper right inset). Similar behavior would be expected in the class of models where l_1 can switch signs as growth increases (see Equation 2.13), indicating that in this class of models, coupling between population growth and phase can modify the nature of the Hopf bifurcation.

2.2.4 Case 2: Division occurs only in one state

When division occurs only in one state ($\epsilon_i = 3\delta_{i1}$), equation 2.4 reduces to

$$
\dot{P}_i = -P_i\Gamma_{i+1} + P_{i-1}\Gamma_i + 3kP_i(\delta_{i,1}\chi - P_1) + \\
\frac{3k}{2}(\delta_{i,3}P_{i+1} + \delta_{i,2}P_{i-1})(1 - \chi) \tag{2.24}
$$

where δ_{ij} is the Kronecker delta. Because the choice of ϵ_i has broken the rotational symmetry of the model, the solution $P_i = 1/3$ is not, in general, a steady state solution to Equation 2.24. In what follows, we first consider the case $\chi = 1/3$, which is amenable to analytical treatment, and then go on to numerically explore the general case $0 \leq \chi \leq 1$.

When $\chi = 1/3$, Equation 2.24 reduces to

$$
\dot{P}_i = -P_i\Gamma_{i+1} + P_{i-1}\Gamma_i + 3kP_i\left(\frac{\delta_{i,1}}{3} - P_1\right) + \\
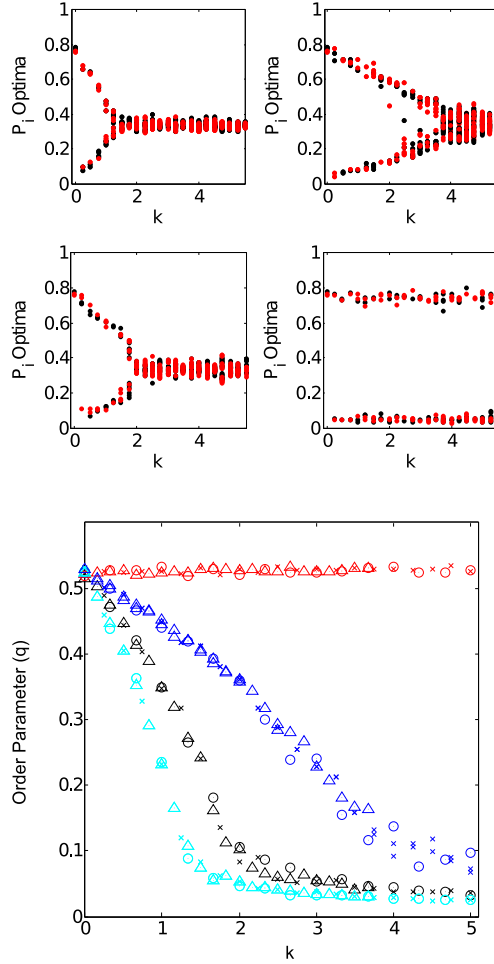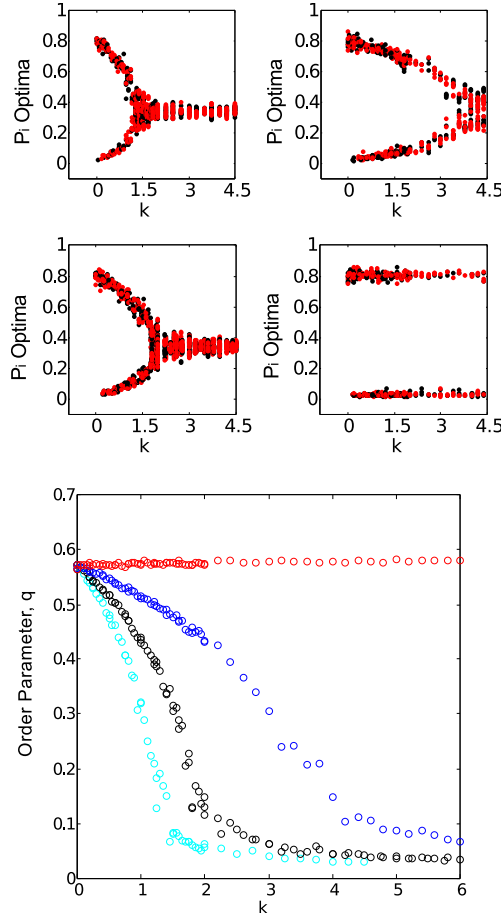k(\delta_{i,3}P_{i+1} + \delta_{i,2}P_{i-1}), \tag{2.25}
$$
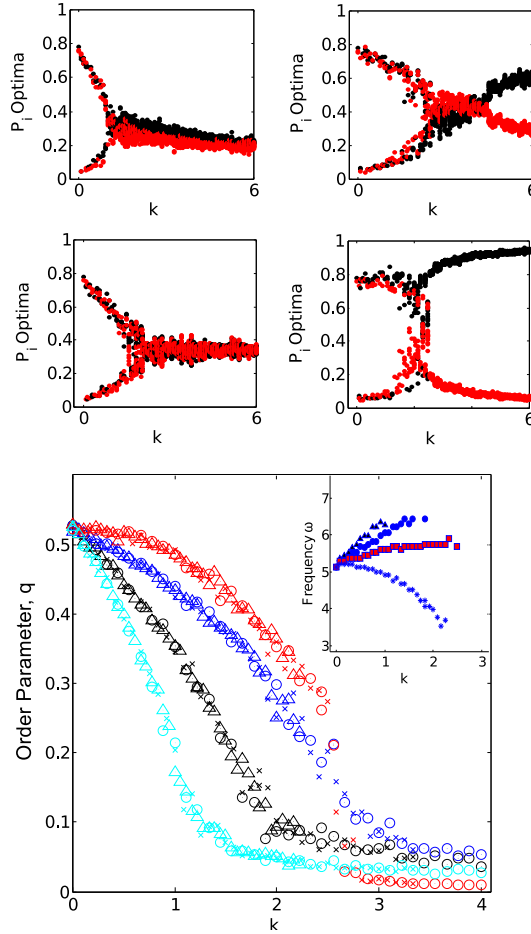
Figure 2.5: Top panels: values of successive maxima / minima of the time series $P_1(t)$ (black, dark) and $P_2(t)$ (red, light) for each value of the dimensionless ratio k for the model Equation 2.24. Top left, $\chi = 0$; bottom left, $\chi = 1/3$; top right, $\chi = 2/3$; bottom right, $\chi = 1$. Bottom panel: order parameter q for $\chi = 0$ (light blue, lightest gray), $\chi = 1/3$ (black), $\chi = 2/3$ (dark blue, darkest gray), and $\chi = 1$ (red, gray). Different shapes represent different intrinsic oscillator frequencies ($g = 0.75$, circles; $g = 1$, crosses; $g = 1.5$, triangles). Inset: frequency ω of macroscopic oscillations, corresponding to the maximum peak of the power spectrum of $P_1(t)$ for $\chi = 0, 1/3, 2/3, 1$ (upper triangles, circles, squares and stars, respectively). In all panels, $a = 20 > a_{c,0}$, $N_0 = 500$, initial conditions are given by $P_1 = 2/3$, $P_2 = 1/3$, and the coupling function $\Gamma_i = 1 + aP_i^2$.

for which $P_i = 1/3$ is always a solution. The corresponding matrix J is identical to Equation 2.6 when $\chi = 1/3$, and the linear stability analysis yields identical results to those in Equations 2.6-2.13. For example, if $\Gamma_i = 1 + aP_i^2$, we have a critical coupling of $a_c = a_{c,0} + 6k$, and when the coupling is fixed at $a = 20$, synchronization is destroyed when $k > k_c = 11/6$, which is consistent with numerical simulations (Figure 2.5). In addition, at the transition point $\omega = \frac{\sqrt{3}}{6}(a_c + 3) = \sqrt{3}\,(2 + k_c)$ and the transition is always supercritical $\left(l_1 = -\frac{3\sqrt{3}(3+2k)}{4+2k} < 0\right)$. Hence, while Equation 2.5 and Equation 2.24 correspond to microscopically distinct mechanisms and differ in higher order terms, when $\chi = 1/3$ the linear stability properties of the fixed point $P_i = 1/3$, which determine synchronization properties near the phase transition, are identical. Intuitively, this correspondence arises because, in both cases, the division process redistributes the oscillators uniformly between the 3 possible states.

For other values of χ, however, state-dependent division can give rise to entirely new dynamics. To explore this behavior, we performed numerical simulations for a wide range of parameters, as in Section 2.2.3. As a prototype model, we choose $\Gamma_i = 1 + aP_i^2$, but we later show that the similar behavior is observed for other coupling functions and even in continuous phase models. While the amplitude of the oscillations decreases with increasing growth rate k (Figure 2.5), the oscillations of P_1 and P_2 do not always occur around the symmetric values $(P_1, P_2) = (1/3, 1/3)$. Furthermore, for sufficiently large values of k, the system appears to settle into a non-oscillating fixed point where the fraction of oscillators in states 1 and 2 can be significantly different. As an example, for $\chi = 2/3$ (Figure 2.5, upper right) the oscillations cease at $k \approx 3$, leading initially to a non-oscillating state where $P_1 < P_2$. This is somewhat counterintuitive, as only oscillators in state 1 divide, and the majority of daughter cells ($\chi = 2/3$) are also in state 1. As k is further increased,
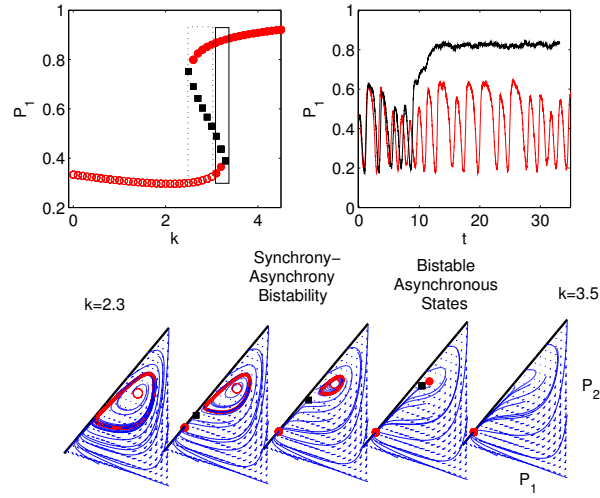
Figure 2.6: Upper left panel: Steady state solution P_1^* of the mean field model, Equation 2.24. Stability is indicated by marker (open circles, unstable points; closed circles, stable points; squares, saddle points). Dashed box is region where synchronous oscillations stably coexist with a non-oscillating state. Solid box is region where two asynchronous states stably coexist. Upper right panel: Two example time series of P_1 from numerical simulations with $N_0 = 2000$ starting from identical initial conditions, $P_1 = 0.45, P_2 = 0.45$. In one case, the system settles into stable oscillations (red, light). In the other case, a fluctuation drives the system to the asynchronous fixed point following initial oscillations (black). Bottom panel: phase portraits for $k = 2.3, 2.6, 2.9, 3.2, 3.5$ (left to right). Thin (blue, dark gray) lines are example trajectories, thick (red, light gray) lines are stable limit cycles; stability of fixed points is indicated by markers (open (red) circles, unstable; closed (red) circles, stable; squares (black), saddle). In all panels, $\chi = 1$.
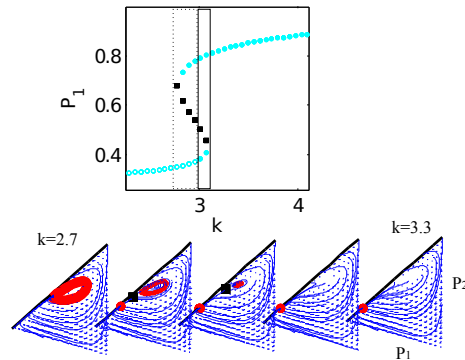
Figure 2.7: Upper panel: Steady state solution P_1^* of the mean field model, Equation 2.24. Stability is indicated by marker (open circles, unstable points; closed circles, stable points; squares, saddle points). Dashed box is region where synchronous oscillations stably coexist with a non-oscillating state. Solid box is region where two asynchronous states stably coexist. Bottom panel: phase portraits for $k = 2.7, 2.85, 3.0, 3.15, 3.3$ (left to right). Thin (blue, dark gray) lines are example trajectories, thick (red, light gray) lines are stable limit cycles; stability of fixed points is indicated by markers (open (red) circles, unstable; closed (red) circles, stable; squares (black), saddle). In all panels, $\chi = 1$.
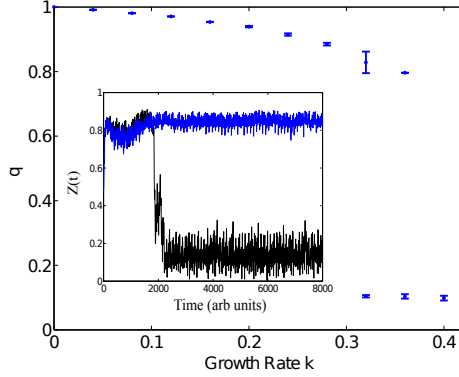
Figure 2.8: Order parameter q in growing population of identical Kuramoto oscillators, each with intrinsic frequency $\omega = 10$. Coupling strength $K = 1$; Number of initial oscillators $N_0 = 500$. When population size reaches $N = 10^6$, the population is reset to a size of $N = 1000$ while preserving the distribution of oscillator phases. Points represent averages from simulations of 10 independent trials. Insets: Time series of order parameter $Z(t)$ for two typical simulations ($k = 0.32$ in both cases) in the bistable region; the population stochastically switches between two stable states, one synchronized (top curve) and one asynchronous (bottom curve).

the population is eventually dominated by oscillators in state 1, as one might expect. Each individual oscillator continues to cycle through all three states, but on average, the distribution of states is not uniform.

In addition, growth can dramatically affect the frequency of oscillations in the synchronous state, but the effect is no longer monotonic for all values of χ. As k is increased, we find oscillations of increasing frequency for $\chi = 0$ and $\chi = 1/3$, approximately constant frequency for $\chi = 2/3$, and rapidly decreasing frequency for $\chi = 1$ (Figure 2.5, lower panel inset). It is somewhat surprising that the choice of χ, alone, can lead to either an increase or decrease in the overall oscillation frequency. Interestingly, the case $\chi = 1$ also appears to undergo an abrupt transition for $k \approx 2.9$, indicating that the transition is qualitatively different from the supercritical Hopf bifurcation in the non-growing model.

To examine this transition in detail, we performed linear stability analysis numerically for $\chi = 1$. In particular, for $\chi = 1$, we find that the fixed point P_1^* remains close to $P_1 = 1/3$ for $k < 3$ and loses stability via a supercritical Hopf bifurcation

at $k \approx 3$, in apparent contradiction with numerical results, which indicate a discontinuous transition at a smaller value of k (see Figure 2.5). Interestingly, a more thorough numerical analysis reveals that a second branch of stable solutions arises at $k \approx 2.5$ (Figure 2.6, upper left). The emergence of this solution branch leads to two types of novel bistable behavior and underlies the abrupt transition observed in numerical simulations. As k is increased above $k \approx 2.5$, one finds bistability between a synchronized oscillating state and a non-oscillating state with $P_1 > P_2 > P_3$. Surprisingly, the synchronized oscillations occur only when oscillator states are initially distributed within a relatively small section of phase space. Initial conditions with $P_i = 1$ for $i =$1, 2, or 3, for example, will (counterintuitively) lead to an asynchronous, non-oscillating steady state dominated by oscillators in state 1. For finite populations, fluctuations may also lead the population to stochastically jump from one stable state (oscillations) to the other (fixed point) (Figure 2.6, upper right). As k is further increased, the unstable fixed point at $P_1 \approx 1/3$ becomes stable (supercritical Hopf), leading to a small region of bistability between two non-oscillating states. Finally, at $k \approx 3.4$, the lower branch of the solution disappears and the population settles into a fixed point on the upper branch of the solution curve. Similar behavior occurs for other χ values in the approximate range $0.8 \leq \chi \leq 1$; for smaller χ, the Hopf bifurcation occurs prior to the emergence of the upper solution branch, leading to a larger region of bistability between asynchronous fixed points.

2.2.4.1 Bistability in Other Classes of Oscillators

When oscillators in any state can divide (i.e. Case 1), our linear stability analysis shows that similar behavior exists for a class of coupling functions, as long as the derivatives follow certain restrictions (see Section 2.2.3). Unfortunately, because the rotational symmetry of the model is broken when only one state can divide (i.e. Case

2), we are not able to provide similar analytical evidence that the bistable behavior discussed in Section 2.2.4 (e.g. Figure 2.6) occurs for other choices of coupling function. However, it is straightforward to perform numerical linear stability analysis for any particular model.

To confirm that these findings are not specific to the chosen form of the coupling function, we performed linear stability analysis for $\Gamma_i = e^{aP_i}$ at $a = 3.65 > a_{c,0}$. As shown in Figure 2.7, we see similar dynamics for this choice of coupling. Specifically, for small k, we see stable oscillations. As k increases, we see a region of bistability between synchronous oscillations and an asynchronous fixed point, followed by a region of bistability between two asynchronous fixed points. Finally, at $k \approx 3$, the lower branch of the solution disappears and the population settles into a fixed point on the other branch of the solution curve. Numerically, we find that similar bistabilities also occur for other coupling functions, including multiple examples of the form $\Gamma_i = 1 + aP_i^n$ with $1 < n \leq 4$ (results not shown). As before, these coupling functions lead to a supercritical Hopf bifurcation in the absence of growth.

Our analysis of discrete phase oscillators suggests that population growth can induce bistability between stable, asynchronous fixed points and stable, synchronous oscillations when the growth is strongly phase-dependent. While the exact mathematical correspondence between these discrete phase models and classic continuous phase models, such as the Kuramoto model, has yet to be rigorously established, one might expect similar bistability to occur in continuous phase models as well. To explore this question, we performed numerical simulations of populations of Kuramoto oscillators [21], whose (continous) phases ϕ evolve according to

$$\dot{\phi}_i = \omega_i + \frac{K}{N} \sum_j \sin(\phi_j - \phi_i), \tag{2.26}$$

ω_i is the intrinsic frequency of oscillator i, K is a coupling parameter, and the sum

runs over all oscillators in the population. We take $\omega_i = \omega$ for all oscillators; for identical oscillators, a synchronous state exists for all $K > 0$. To incorporate phase dependent population growth, at each time step we allow oscillators whose phase falls in a given range, $\phi_0 \le \phi \le \phi_1$, to reproduce with probability per unit time k. Following division, the daughter oscillator has a phase that is chosen to fall in the range $\phi_0 \le \phi \le \phi_1$ with uniform probability. To circumvent numerical limitations due to exponentially growing populations, we start with $N_0 = 500$ oscillators and allow them to grow to a total size of $N = 10^6$; when N reaches this maximum value, we reset the population size to $N = 1000$ while preserving the phase distribution of oscillators. In practice, we preserve the approximate phase distribution by binning oscillator phases into a total of M bins over the range $0 \le \phi \le 2\pi$. Prior to resetting the population size, we calculate the fraction of oscillators in each bin and choose the phases in the smaller population so that the distribution is conserved. We find that similar behavior is observed as long as M is sufficiently large. In what follows, we choose $M = 10$, $\phi_0 = \pi/3$, $\phi_1 = 2\pi/3$, and we set $K = 1$.

As with the discrete oscillators, numerical simulations suggest that population growth decreases the synchrony of the population, eventually leading to a discontinuous transition to asynchronous behavior and a region of bistability between synchronous and asynchronous oscillations (Figure 2.8). Because the simulations involve finite populations, it is common to see trajectories that stochastically switch between stable oscillations and asynchronous behavior (Figure 2.8, inset). While a full analysis of continuous models is an exciting avenue for future work, we stress that our goal here is simply to provide evidence that growth-induced bistability can occur in continuous phase models. Further analysis along these lines is necessary and would be welcome, but it is beyond the scope of the current work.

2.3 Excitable Elements

2.3.1 Model for Growing Populations of Excitable Elements

The results of Section 2.2 raise the question of whether population growth might have similar effects on populations of coupled excitable elements. To explore this question in a simple context, we will model an excitable system as a discrete m-state system comprised of a quiescence state (0), an excited state (1), and a finite set of refractory states $(2, 3, ..., m - 1)$ using the model introduced in [47]. For each state i, the discretized phase is $\theta = 2\pi i/m$. Here we study a simple four state system, which contains the minimum number of refractory states (2) required for stable synchronization [63].

This discrete time model involves deterministic transitions between states $1 \to 2$ and $2 \to 3$ and probabilistic transitions from the quiescent state 0 to the activated state 1. Coupling between elements is achieved by allowing the transition from state 0 to state 1 to depend on the states of the neighboring systems and a parameter σ that measures the strength of the inter-element coupling. The last transition, from state 3 back to the quiescent state 0, is also probabilistic and occurs with probability p_γ, which is the same for all excitable elements [47]. A thorough analysis of this model [47] reveals that, in the thermodynamic limit, the population transitions from an absorbing state to an active state at a critical value of σ. More interestingly, for certain choices of p_γ, it can undergo synchronous oscillations within a range of coupling strengths $\sigma_1 < \sigma < \sigma_3$, and there exists a region of bistability between synchronous oscillations and an asynchronous fixed point for $\sigma_2 < \sigma < \sigma_3$, with $\sigma_1 < \sigma_2 < \sigma_3$.

In what follows, we study this model in the case where individual elements are allowed to reproduce, producing daughter elements in potentially different states. As

with the oscillators, we focus on two cases: all oscillators are equally likely to divide (case 1), and division occurs only for oscillators in one particular state (case 2). As before, the daughter element will be in the same state as the mother with probability χ, and will be randomly assigned to each of the other states with probability $(1 - \chi)/3$. The discrete nature of the model makes it amenable to rapid numerical simulations [47], which we explore in the next section.

2.3.2 Numerical Simulations

We performed discrete time simulations starting from $N_0 = 10^4$ globally coupled excitable elements for $t = 500$ total time steps. To avoid limits due to computational memory, we reduce the total population size by a factor of 5 (while preserving the state distribution) when the number of units reaches 5×10^4. As in [47], we take the probability of exciting a quiescent state to be

$$p_\mu(t) = 1 - \left(1 - \frac{\sigma}{N(t)}\right)^{N_t(1)}, \tag{2.27}$$

where $N(t)$ is the total number of units at time step t, $N_t(1)$ is the number of elements in state 1 at time step t, each excited element can activate a neighbor in the quiescent state with probability $\sigma/N(t)$, and p_μ reflects the probability that the quiescent state is excited by at least one of its $N_t(1)$ active neighbors. We choose initial conditions so that $P_0(0) = 0.8$ and $P_0(1) = 0.2$, where $P_i(j)$ is the fraction of oscillators in state j at time step i. For each choice of k and χ, we continuously increased coupling strength σ from 2 to 50 for each successive simulation, using the steady state from the previous value of σ as initial conditions for the next value. We then repeated the simulations starting from $\sigma = 50$ and decreasing σ to 0; when simulations reached a steady state, we calculated the order parameter q, which is the same as that used for oscillators (see Section 2.2).

In the case where all states can divide, the most salient effect of population growth is to decrease the range of σ over which oscillations are stable (Figure 2.9). For example, when $p_\gamma = 0.94$, [47] showed that the model undergoes a synchronizing transition as σ is increased from zero. Further increase of σ leads to discontinuous re-entrant transition that includes a region of bistability between synchronous and asynchronous states (black curves, main panel). When including population growth, we find that as k is increased from zero, the size of both the synchronized and bistable regions shrink (Figure 2.9, blue curves); as k is further increased, the bistable region eventually disappears (Figure 2.9, red curves) and, eventually, the entire synchronization region is lost (not shown). We observe a similar decrease in the size of the oscillatory regime for $\chi = 0$ (top panels) and $\chi = 1$ (bottom panels) and for smaller values of p_γ where bistability does not exist, even in the absence of growth. In all cases, increasing χ slightly counteracts the effect of population growth; that is, larger χ leads to a slightly larger region of synchrony and/or bistability.

We find qualitatively similar behavior when division is restricted to only one state, such as state 1 (Figure 2.10). Interestingly, however, we find that the effect of increasing χ will depend on which state is chosen for division. Specifically, when division is restricted to states 0, 2 or 3, increasing χ will lead to an increase in the size of the active region (Figure 2.10, upper insets), as in the case where all states can divide (Figure 2.9). By contrast, when division is restricted to state 1, increasing χ will lead to a decrease in the size of the active region (Figure 2.10, main panels and lower insets).

For all simulations, we also calculated 1) the frequency of macroscopic oscillations in the active regions and 2) the maximum growth rate–which we refer to as the critical growth rate–that still allows for synchronous oscillations. Figure 2.11(a) shows that
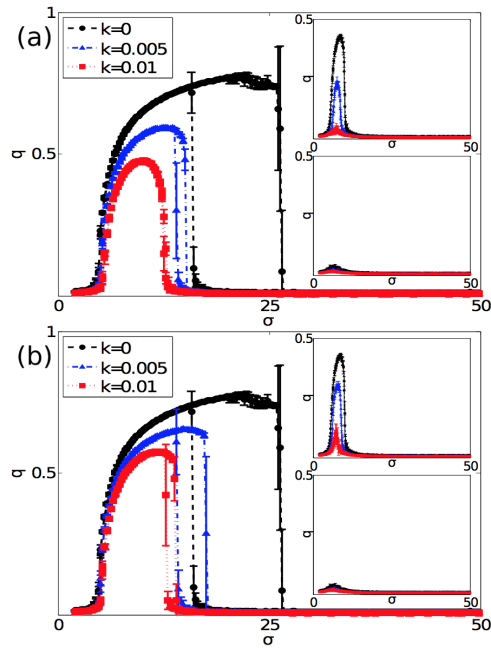
Figure 2.9: Order parameter q vs coupling strength σ when all states divide for (a) $\chi = 0$ and (b) $\chi = 1$. Error bars are from standard deviations over 10 runs. Black dashed (upper curve), blue dash dot (middle curve) and red dotted line (lower curve) represent growth rate $k = 0$, 0.005 and 0.01, respectively, at $p_\gamma = 0.94$. For smaller values of p_γ, the size of the active region shrinks and the bistable area disappears, even in the absence of growth (upper insets in (a) and (b): $p_\gamma = 0.84$). If p_γ is further reduced, stable oscillations will eventually disappear (lower insets in (a) and (b): $p_\gamma = 0.74$).
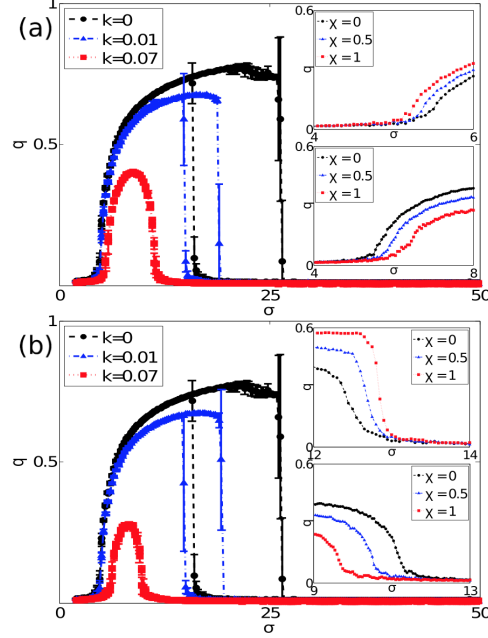
Figure 2.10: Order parameter q vs coupling strength σ when division is restricted to one state. Main panels: Division is restricted to units in state 1: (a) $\chi = 0$ and (b) $\chi = 1$. Black dashed (upper curve), blue dash dot (middle curve) and red dotted lines (lower curve) represent growth rate $k = 0$, 0.01 and 0.07, respectively at $p_\gamma = 0.94$. When increasing χ from 0 to 1, the size of the active region shrinks (lower insets of both panels, $k = 0.07$). For comparison, upper insets show effect of increasing χ when division is independent of state (upper insets in (a) and (b), $k = 0.01$).

population growth increases the frequency of oscillations, regardless of which state is chosen for division. Figure 2.11(b) illustrates that as χ increases, the critical growth rate increases when division is independent of state or is restricted to states 0, 2, or 3; the opposite trend exists when division is restricted to state 1 (upper red triangles).

2.3.3 Mean Field and Linear Stability Analysis

To gain a systematic picture of these results, we follow the approach in [47] to develop a mean field approximation and derive full phase diagrams for these excitable systems. Specifically, by assuming that probability of exciting a quiescent state via one of its $N(t) - 1$ neighbors is $\sigma P_t(1)/(N(t) - 1)$, the probability of excitation via at least one excited neighbor is

$$p_\mu(t) = 1 - \left(1 - \frac{\sigma P_t(1)}{N(t) - 1}\right)^{(N(t)-1)}. \tag{2.28}$$
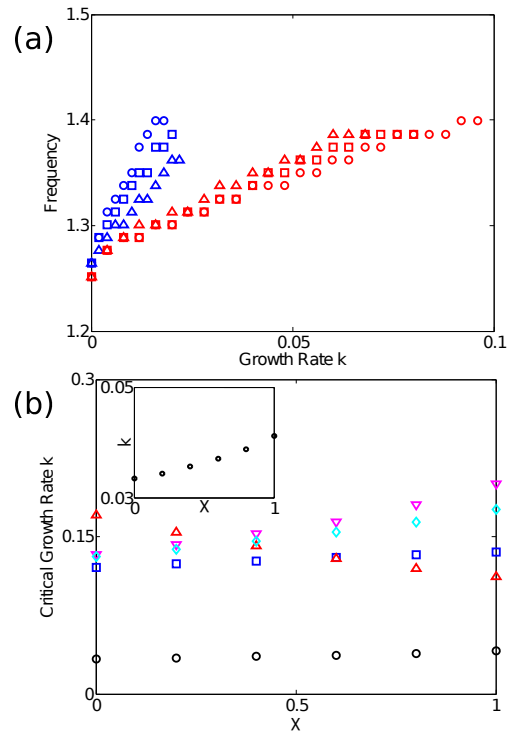
Figure 2.11: Frequency and critical growth rate vs χ. Upper figure: circle, square and up triangle represent $\chi = 0$, 0.5 and 1, respectively. Blue (darker) shows the case in which all states divide and red (lighter) means only state 1 divides. $p_\gamma = 0.9$ and $\sigma = 8$. Lower figure: black circle, blue square, red up triangle, magenta down triangle and cyan diamond represent five cases (all states divide, only state 0 divides...), respectively. Inset: zoom in black circle (all states divide case)

In the thermodynamic limit, p_μ becomes $1 - e^{-\sigma P_t(1)}$. In the case where all states divide, the system is governed by the difference equations

$$N_{t+1}(0) = p_\gamma N_t(3) + e^{-\sigma P_t(1)} N_t(0)$$

$$+ k(\chi N_t(0) + \frac{1-\chi}{3}(N_t(1) + N_t(2) + N_t(3)))$$

$$N_{t+1}(1) = (1 - e^{-\sigma P_t(1)}) N_t(0)$$

$$+ k(\chi N_t(1) + \frac{1-\chi}{3}(N_t(0) + N_t(2) + N_t(3)))$$

$$N_{t+1}(2) = N_t(1)$$

$$+ k(\chi N_t(2) + \frac{1-\chi}{3}(N_t(0) + N_t(1) + N_t(3)))$$

$$N_{t+1}(3) = N_t(2) + (1 - p_\gamma) N_t(3)$$

$$+ k(\chi P_t(3) + \frac{1-\chi}{3}(N_t(0) + N_t(1) + N_t(2))),$$

$$(2.29)$$

and the total number of oscillators follows $N(t+1) = (1+k)N(t)$. If all equations are divided by the total number of oscillators, we arrive at equations for the probability $P_t(i)$ to be in state i at time t,

$$P_{t+1}(0) = \frac{p_\gamma}{1+k} P_t(3) + \frac{e^{-\sigma P_t(1)}}{1+k} P_t(0)$$

$$+ \frac{k}{1+k}(\chi P_t(0) + \frac{1-\chi}{3}(1 - P_t(0)))$$

$$(2.30)$$

$$P_{t+1}(1) = \frac{1 - e^{-\sigma P_t(1)}}{1+k} P_t(0)$$

$$+ \frac{k}{1+k}(\chi P_t(1) + \frac{1-\chi}{3}(1 - P_t(1)))$$

$$(2.31)$$

$$P_{t+1}(2) = \frac{1}{1+k} P_t(1)$$

$$+ \frac{k}{1+k}(\chi P_t(2) + \frac{1-\chi}{3}(1 - P_t(2)))$$

$$(2.32)$$

$$P_{t+1}(3) = \frac{1}{1+k} P_t(2) + \frac{1 - p_\gamma}{1+k} P_t(3)$$

$$+ \frac{k}{1+k}(\chi P_t(3) + \frac{1-\chi}{3}(1 - P_t(3))).$$

$$(2.33)$$

Similarly, if division is restricted to only one state, such as state 1, we have

$$P_{t+1}(0) = \frac{p_\gamma}{1 + kP_t(1)}P_t(3) + \frac{e^{-\sigma P_t(1)}}{1 + kP_t(1)}P_t(0)$$
$$+ \frac{k(1 - \chi)}{3(1 + kP_t(1))}P_t(1)$$

(2.34)

$$P_{t+1}(1) = \frac{1 - e^{-\sigma P_t(1)}}{1 + kP_t(1)}P_t(0) + \frac{k\chi}{1 + kP_t(1)}P_t(1)$$

(2.35)

$$P_{t+1}(2) = \frac{1}{1 + kP_t(1)}P_t(1) + \frac{k(1 - \chi)}{3(1 + kP_t(1))}P_t(1)$$

(2.36)

$$P_{t+1}(3) = \frac{1}{1 + kP_t(1)}P_t(2) + \frac{1 - p_\gamma}{1 + kP_t(1)}P_t(3)$$
$$+ \frac{k(1 - \chi)}{3(1 + kP_t(1))}P_t(1).$$

(2.37)

It is easy to derive similar equations when division is restricted to one of the other states. In all cases, nontrivial steady states $P^*(i)$ occur when $P_{t+1}(i) = P_t(i)$ ($i = 0, 1, 2, 3$). Since the probabilities are normalized to 1, we can omit equations (2.30) and (2.34) and reduce each set of equations by one.

To study the stability of nontrivial solutions, we linearize the equations near each solution; the corresponding Jacobian matrix J when all states can divide is given by

$$J = \frac{J_N}{1 + k} + \left(\frac{k}{1 + k} \left(\chi - \frac{1 - \chi}{3} \right) \right) I,$$

(2.38)

where J_N is the Jacobian for non-dividing populations [47]

$$J_N = \begin{pmatrix} a_{11} & e^{-\sigma P_1} - 1 & e^{-\sigma P_1} - 1 \\ 1 & 0 & 0 \\ 0 & 1 & 1 - p_\gamma \end{pmatrix}\Bigg|_{\vec{P}*},$$

(2.39)

I is identity matrix, and $a_{11} = \sigma e^{-\sigma P_1}(1 - P_1 - P_2 - P_3) + e^{-\sigma P_1} - 1$. At steady state, $P_1^* = P_2^* = p_\gamma P_3^*$. We note that even when $\chi = 1$ and the excitable elements reproduce to form identical daughter cells, the model does not reduce to the corresponding non-growing model. Hence, unlike the oscillator model, growth will modify

38
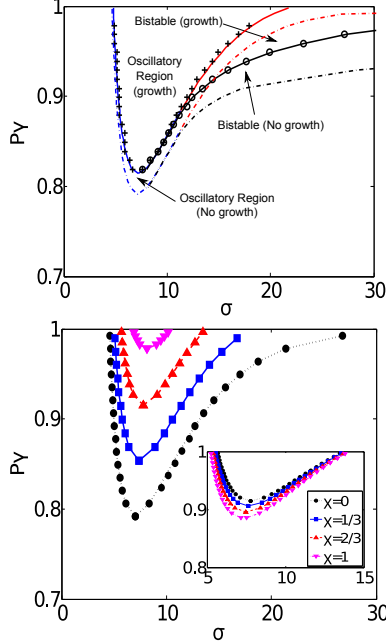
Figure 2.12: Phase diagrams when all oscillator states can divide. Upper panel: Phase diagram p_γ vs σ when all states divide and $k = 0.005$, $\chi = 1$. Curves indicate nature of bifurcation (blue (gray), supercritical Hopf; red (light gray), subcritical Hopf; black, global saddle node of limit cycles). Regions of bistability between synchronous and asynchronous states are indicated. Crosses and circles indicate results from numerical simulations ($N_0 = 10^4$). Black line shows numerical σ_{c3} from mean field analysis. Cross and circle represent simulation results. Dash dot curves show non-growing case for comparison. Lower panels: phase boundaries (excluding bistable regions) when all states divide, $\chi = 0$; $k = 0$ (black circle), $k = 0.01$ (blue square), $k = 0.02$ (red up triangle), $k = 0.03$ (magenta down triangle). Lower right inset, $k = 0.02$ for different values of χ: Black circle, blue square, red up triangle, magenta down triangle represent $\chi = 0$, $\frac{1}{3}$, $\frac{2}{3}$ and 1, respectively.

the dynamics of these excitable systems even in the case when all states can divide and $\chi = 1$. For cases where division is restricted to one state, the Jacobian can be readily calculated numerically, but it cannot be simply written in terms of J_N.

As in the case of continuous time systems, the eigenvalues provide information about the stability of each fixed point. Specifically, bifurcations between stable and unstable fixed points occur when $|\lambda| = 1$, allowing us to dilineate phase boundaries separating oscillatory and non-oscillatory regimes. Specifically, we are interested in the location of Neimark-Sacker (NS) bifurcations, which are the discrete time analog of a Hopf bifurcation. As with Hopf bifurcations, the nature of the transition is given by the sign of the first Lyapunov coefficient: the NS bifurcation is supercritical
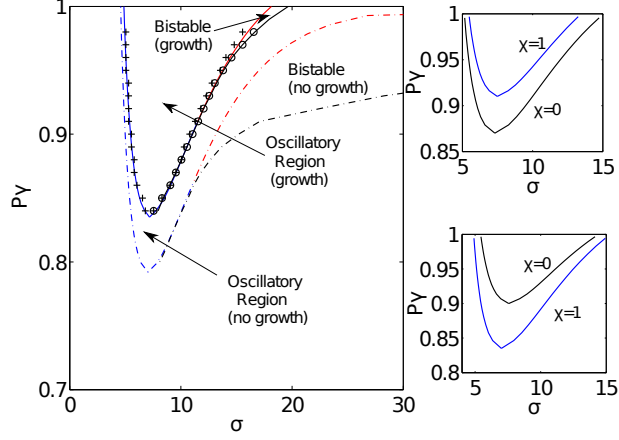
Figure 2.13: Phase diagrams when division is restricted to one state. Main panel: phase diagram for excitable elements with growth (solid lines; $\chi = 0$, $k = 0.04$, only state 1 can divide) and without growth (dashed lines). Curves indicate nature of bifurcation (blue (gray), supercritical Hopf; red (light gray), subcritical Hopf; black, global saddle node of limit cycles). Regions of bistability between synchronous and asynchronous states are indicated. Crosses and circles indicate results from numerical simulations ($N_0 = 10^4$). Right panel, phase boundaries (excluding bistable regions) for $\chi = 0$ and $\chi = 1$ when only state 1 (top) or only state 2 (bottom) divides; $k = 0.07$ in both cases.

if $l_1 < 0$ and subcritical if $l_1 > 0$. Following standard bifurcation theory (see, for example, [47]), we calculate l_1 as

$$
\begin{aligned}
l_1 = \frac{1}{2} Re \Big\{ \bar{\lambda} \Big[& \Big\langle \vec{s}, \vec{C}(\vec{r}, \vec{r}, \bar{\vec{r}}) \Big\rangle \\
& + 2 \Big\langle \vec{s}, \vec{B}(\vec{r}, (I - J)^{-1} \vec{B}(\vec{r}, \bar{\vec{r}})) \Big\rangle \\
& + \Big\langle \vec{s}, \vec{B}(\bar{\vec{r}}, (\lambda^2 I - J)^{-1} \vec{B}(\vec{r}, \vec{r})) \Big\rangle \Big] \Big\},
\end{aligned}
\tag{2.40}
$$

where brackets represent the standard complex inner product, $\vec{r}$ is the eigenvector of the Jacobian matrix with corresponding eigenvalue λ, $\vec{s}$ is the eigenvector of J^T with eigenvalue λ^*, and normalization is chosen so that $\langle \vec{r}, \vec{r} \rangle = 1$ and $\langle \vec{s}, \vec{r} \rangle = \sum_{i=1}^{3} \bar{s}_i r_i = 1$. Furthermore, $\vec{B}(\vec{x}, \vec{y})$ and $\vec{C}(\vec{x}, \vec{y}, \vec{z})$ are vector-valued multi-linear functions

$$
\begin{aligned}
B_i(\vec{x}, \vec{y}) &= \sum_{j,k=1}^{3} \frac{\partial^2 F_i(\vec{P}_t)}{\partial P_t(j) \partial P_t(k)} \Bigg|_{\vec{P}^*, \sigma_c} x_j y_k, \\
C_i(\vec{x}, \vec{y}, \vec{z}) &= \sum_{j,k,l=1}^{3} \frac{\partial^3 F_i(\vec{P}_t)}{\partial P_t(j) \partial P_t(k) \partial P_t(l)} \Bigg|_{\vec{P}^*, \sigma_c} x_j y_k z_l,
\end{aligned}
\tag{2.41}
$$

where $\vec{x} = (x_1, x_2, x_3)^T$, $\vec{y} = (y_1, y_2, y_3)^T$ and $\vec{z} = (z_1, z_2, z_3)^T$ are arbitrary vectors.

40

As in [47], when $l_1 > 0$ (indicating a subcritical bifurcation and the corresponding bistability), we supplement the above calculations with simulations of the mean field equations to determine the location of the bistable regimes, which are not fully determined by linear stability properties.

Figure 2.12 shows the resulting phase diagrams for the case where all states divide, and Figure 2.13 shows the phase diagram when division is restricted to state 1. Population growth has several obvious effects on the excitable systems. First, growth can shift the location of the fixed points, but unlike the oscillator case, we do not find evidence of new fixed points. Consistent with our simulations, growth shifts the phase boundaries to higher values of p_γ, leading to a smaller region of synchronized oscillations and a significantly reduced region of bistability; as k is further increased, the oscillatory region is eventually eliminated (see Figure 2.12, bottom panel). The phase diagrams indicate that adding growth can have significant effects on the dynamics, depending on the values of σ and p_γ. Consider, for example, the main panel of Figure 2.13. Systems originally undergoing oscillations can enter a bistable state (e.g. $(\sigma, p_\gamma) = 18, 0.98)$) or a non-oscillating active state (e.g. $(\sigma, p_\gamma) = 8, 0.82)$) when growth is increased to $k = 0.04$. Qualitatively similar behavior is observed when division is restricted to one of the other states, or when all states can divide (Figure 2.12).

Interestingly, we also find that the effect of χ on the phase diagram will depend on which state is chosen for division (Figure 2.12, bottom inset; Figure 2.13, right panels). For example, increasing χ at a fixed value of k will raise the phase boundary to higher p_γ when state 1 divides, but will lower the boundary when states 0, 2, or 3 divide (Figure 2.13, right panels) or when all states can divide (Figure 2.12, bottom inset). When only the excited state (1) divides, self-similarity between mother and

daughter oscillators decreases the area of phase space over which synchrony can occur, while such self-similarity increases the size of the synchronized region when any of the non-excited states divide.

2.4 Discussion

We have shown that population growth, and the corresponding redistribution of oscillator phases, can induce a wide range of new dynamic behaviors in systems of coupled oscillators and excitable elements. In particular, when growth is independent of oscillator phase, increasing growth rate leads to an increase in oscillation frequency and a decrease in phase synchrony, eventually culminating in a transition to a non-oscillating steady state. Interestingly, the growth-induced transition can be subcritical, even when the non-growing model exhibits a supercritical bifurcation; in that case, one sees a bistable region with coexisting synchronous and asynchronous states, depending on the derivatives of the coupling function. When division is strongly state dependent, growth can again lead to extinction of oscillations, but in certain parameter regimes, one finds new asynchronous states with unequal phase distributions, bistability between two asynchronous states or between asynchronous and oscillatory states, or modulation of the bulk oscillation frequency. In excitable systems, which may include bistable behavior even in the absence of growth, the most salient effects of growth are to shift the phase boundaries separating active, oscillatory, and bistable regimes while also increasing the frequency of super-threshold oscillations. In practice, the shifting phase boundaries can lead to a range of different dynamical effects, many of which mirror the behaviors seen in oscillators. For example, systems originally undergoing oscillations can enter a bistable state or a non-oscillating active state when growth is increased.

Our work complements several recent studies on specific biological systems. Notably, a number of interesting studies have examined cell-density dependent synchronization (see, for example, [38, 37]). In these systems, synchronization of intracellular dynamics can be modified at high cell densities as a result of biochemical communication known as quorum sensing. These studies do not directly explore the effects of population growth rate, but instead treat cell density as the relevant control parameter that governs not only intracellular coupling, but also the dynamics of individual cells. It may be interesting to further explore the role of population growth rate itself on synchronization in these systems. In addition, the authors of [30] develop a detailed biochemical model of circadian clocks in growing cyanobacteria populations. They show that otherwise stable oscillations–specifically, those driven by phosphorylation cycles–are destabilized at high growth rates via a supercritical Hopf bifurcation for the chosen range of parameters. Therefore, in fast growing populations, additional stabilizing mechanisms (transcription-translation cycles) are required to preserve integrity of the oscillations. The current work raises the question of whether subcritical bifurcations, including the bistability observed in our models, might occur in different parameter regimes.

We have shown that population growth can dramatically influence synchronization phenomena and, in some cases, lead to entirely new dynamical states in populations of coupled oscillators and excitable elements. While we focused on discrete phase models because of their relative simplicity, we hope these results will motivate future explorations on the interplay between synchronization and population growth in additional models of oscillators, excitable elements, and perhaps more general dynamical systems. Given the theoretical importance of self-synchronization in statistical physics and its ubiquity in biological systems, we believe that the potential

effects of population growth on collective oscillations will prove to be an important and rich topic for future exploration.

CHAPTER III

Interplay Between Antibiotic Efficacy and Drug-induced Lysis Underlie Enhanced Biofilm Formation at Subinhibitory Drug Concentrations

3.1   Introduction

Biofilms are dense, surface-associated microbial communities that play an important role in infectious diseases and a range of device-related clinical infections [20, 64]. Biofilms exhibit a fascinating range of community behavior [65], including long-range metabolic codependence [7] and electrical signaling [8, 9, 10], phenotypic phase variation [11] and spatial heterogeneity [12], strong ecological competition [13], and multiple types of cooperative behavior, including collective resistance to antimicrobial therapy [14, 15, 16]. The biofilm response to antibiotics has been a topic of particular interest, with biofilms across species showing dramatically increased resistance to antibiotics relative to planktonic cells. Surprisingly, however, a number of recent studies have shown that exposure to sub-lethal doses of antibiotics may *enhance* biofilm formation in a range of species [66, 67, 18]. While antibiotic-mediated biofilm induction has been associated with modulated expression of biofilm-related genes, particularly those affiliated with bacterial and cell surface adhesion, cell motility, or metabolic stress, the mechanisms vary across species and drug classes and remain a focus of ongoing research efforts [67, 18].

In this work, we investigate the effects of sublethal antibiotic concentrations on biofilm formation in *E. faecalis*, a gram-positive bacteria commonly underlying nosocomial infections, including bacteremia, native and prosthetic valve endocarditis, and multiple device infections [19, 20]. While our understanding of the molecular basis of both biofilm development and drug resistance in *E. faecalis* continues to rapidly mature [19, 68], surprisingly little attention has been paid to the impact of subinhibitory antibiotic treatments on *E. faecalis* communities. However, a recent series of studies has shown that *E. faecalis* biofilm formation (without antibiotic) hinges on an intriguing interplay between fratricide-associated cell lysis and the release of extracellular DNA (eDNA) [69, 70, 71, 72, 73]. More generally, eDNA is widely recognized as a critical component of biofilm structure in many species [74, 75, 76]. Additionally, a recent study in *S. aureus* showed that β-lactams administered at subinhibitory concentrations promoted biofilm formation and induced eDNA release in an autolysin-dependent manner [77]. Taken together, these results suggest that– for some drugs–biofilm induction hinges on a balance between the inhibitory effects of antibiotics–which reduce biofilm formation at sufficiently high concentrations–and the potential of antibiotic-induced cell lysis to promote biofilm formation, presumably through release of eDNA. Here we investigate this trade-off in *E. faecalis* biofilms exposed to multiple classes of antibiotics. We find that subinhibitory doses of cell wall synthesis inhibitors, but not other classes of drug, promote biofilm formation associated with increased cell lysis and increased eDNA and eRNA. Using a simple mathematical model, we quantify the trade-offs between drug efficacy and "beneficial" cell lysis and use the model to predict the effect of environmental perturbations, including the addition of DNase or chemical inhibitors of lysis, on the location and height of optimal biofilm production. Our results suggest that inhibitors of cell wall
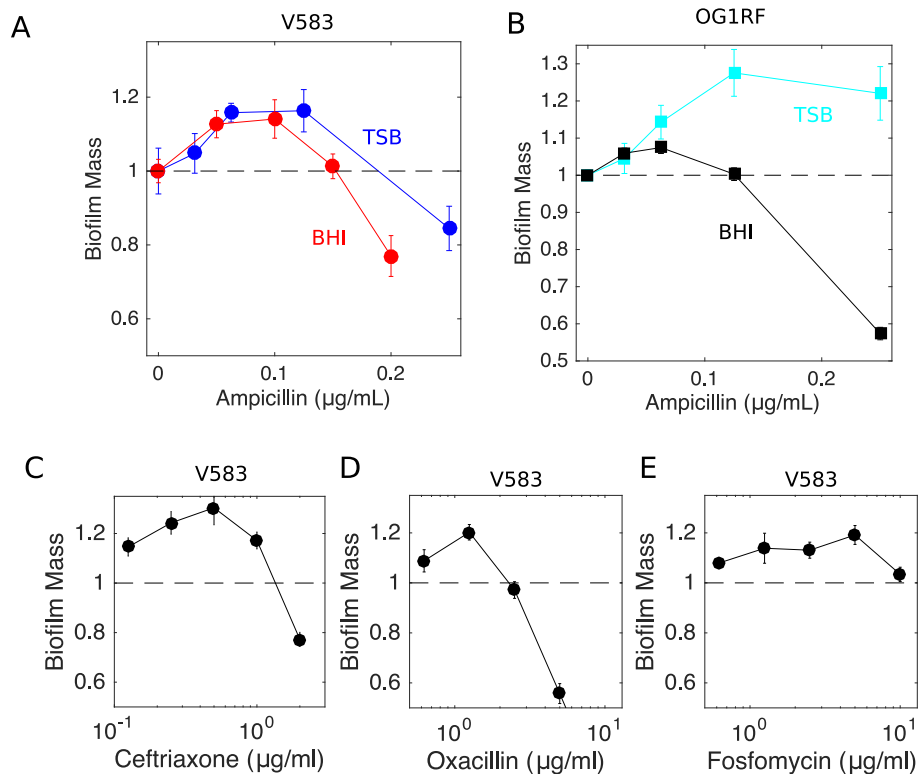
Figure 3.1: Inhibitors of cell wall synthesis enhance biofilm formation at low concentrations. A. Biofilm mass (normalized to 1 in the absence of drug) as a function of ampicillin concentration for E. faecalis strain V583 in TSB (blue) and BHI (red). B. Similar to panel A, with E. faecalis strain OG1RF in TSB (light blue) and BHI (black). Similar curves are also shown for V583 in BHI exposed to three additional cell wall synthesis inhibitors: ceftriaxone (C), oxacillin (D), and fosftomycin (E). In all panels, biofilm mass is measured by crystal violet assay (see Methods). Error bars are ± standard error of the mean from ten replicates.

synthesis promote biofilm formation via increased cell lysis and offer a quantitative, predictive framework for understanding the trade-offs between drug toxicity and lysis-induced biofilm induction.

3.2   Results

3.2.1   Cell wall synthesis inhibitors, but not other classes of antibiotics, promote biofilm formation at low concentrations

To investigate antibiotic induced biofilm formation, we exposed cultures of E. faecalis V583, a fully sequenced clinical isolate, to ampicillin during the first 24 hours of biofilm development. Using a bulk crystal violet staining assay (Methods),
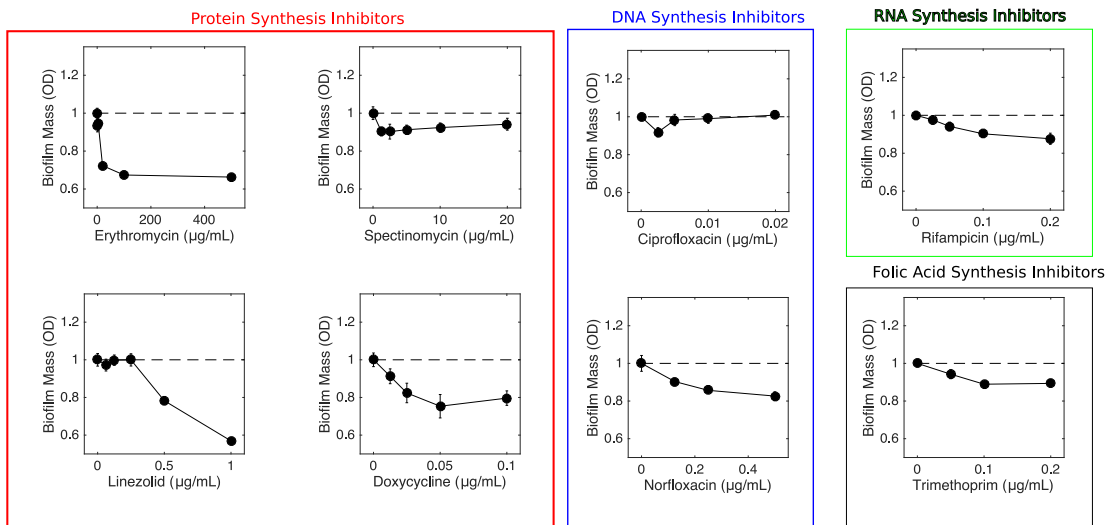
Figure 3.2: Antibiotics that do not target the cell wall do not enhance biofilm formation. Biofilm mass (normalized to 1 in the absence of drug) as a function of antibiotic for E. faecalis strain V583 in BHI exposed to protein synthesis inhibitors (red box: erythromycin, spectinomycin, linezolid, doxycycline), DNA synthesis inhibitors (blue box: ciprofloxacin, norfloxacin), RNA synthesis inhibitor (green box: rifampicin), and folic acid synthesis inhibitors (black box, trimethoprim). In all panels, biofilm mass is measured by crystal violet assay (see Methods). Error bars are $\pm$ standard error of the mean from ten replicates.

we observed a statistically significant enhancement of biofilm formation after 24 hours in the presence of low doses of ampicillin (Figure 3.1 A). Similar effects were observed for cells grown in different types of media (BHI, TSB) as well as for strain OG1RF, a common laboratory strain (Figure 3.1 B), with the magnitude of the enhancement ranging from $\approx 10 - 30\%$.

To determine whether the biofilm enhancement was specific to ampicillin, we performed similar experiments for antibiotics from multiple drug classes. Interestingly, we observed a similar increase of biofilm mass for other drugs inhibiting cell wall synthesis, including ceftriaxone, oxacillin, and fosfomycin (Figure 3.1 C-E), whose mechanism of action is tightly linked to cell lysis. By contrast, drugs targeting protein synthesis, DNA synthesis, RNA synthesis, and folic acid synthesis did not promote biofilm formation (Figure 3.2).

3.2.2 Biofilm enhancement occurs at subinhibitory concentrations but is associated with increased cell lysis and extracellular nucleic acid

In ampicillin, peak biofilm formation occurs for concentrations of approximately 0.1 μg/mL, which is significantly below the reported minimum inhibitory concentration (MIC) for V583. To determine whether this concentration has a measurable effect on the viability of V583 in planktonic phase, we measured optical density time series of V583 cultures exposed to differing drug concentrations (Figure 3.3 A). Ampicillin has little effect ($< 10\%$) on the steady state density of cells up to concentrations of approximately 0.2 μg/mL, and the dose response curve is well-approximated by a Hill-like function, which is commonly used in pharmacology, that exhibits a half-maximal inhibitory concentration of $K_{50} = 0.38 \pm 0.01$ μg/mL. Therefore, increased biofilm formation occurs at concentrations that have little impact on planktonic cell growth.

While these drug concentrations do not appreciably impact planktonic cell growth, it's possible that they still produce a measurable increase in cell lysis. To investigate this issue, we measured cell lysis in 24 hour biofilms (Figure 3.3 B) and planktonic cultures (Figure 3.6) using an established ATP-based luminescence assay. Indeed, we observed increase cell lysis even for low doses of ampicillin (≤ 0.2 μg/mL), with lysis increasing by nearly 5 fold in biofilms and several thousand fold in planktonic cultures for the highest doses.

Because eDNA has been implicated in *E. faecalis* biofilm formation, we next asked whether subinhibitory doses of ampicillin lead to increased quantities of extracellular nucleic acids in biofilms. To answer this question, we grew 24-hour biofilms in 5 mL cultures at various concentrations of ampicillin, harvested the biofilms and removed cells by centrifugation, and then extracted nucleic acid from remaining supernatant.

We then quantified DNA (RNA) following treatment with RNase (DNase) using quantitative imaging of agarose gel electrophoresis. Both eDNA and eRNA increase with ampicillin treatment, with eDNA (but not eRNA) increasing even at the lowest dose (ampicillin at 0.1 μg/mL).

3.2.3 Non-antibiotic induction of cell lysis promotes biofilm formation

Because cell lysis is observed at subinhibitory doses of ampicillin, and because lysis has been previously implicated in biofilm formation, we next asked whether non-antibiotic inducers of cell lysis might also increase biofilm mass at small concentrations. To test this hypothesis, we grew biofilms in the presence of Triton X-100, a surfactant and known inducer of cell lysis. Interestingly, we observed enhancement of biofilm formation similar in magnitude ($\approx$ 20%) to that observed for cell wall inhibitors over Triton X-100 concentrations that yield similar (approximately 1.5-2 fold) increase of cell lysis (Figure 3.3 D).

3.2.4 Antibiotic-induced biofilm formation corresponds to an increase in number of living cells

While our results indicate that biofilm mass is increased at low doses of ampicillin, it is not clear whether this enhancement is due to an increase in the number of living cells or merely an increase in bulk biofilm mass, which may include both viable and non-living components. To answer this question, we grew 16 replicate biofilms at 3 different antibiotic concentrations, treated them with live-dead cell stains, and quantified the number of live and dead cells in two-dimensional sections at single-cell resolution using laser-scanning confocal microscopy (Methods). We observed an average increase in the number of living cells of approximately 25%, similar in magnitude to the effects observed in bulk experiments. These results indicate that biofilms formed under subinhibitory concentrations contain more living cells–not
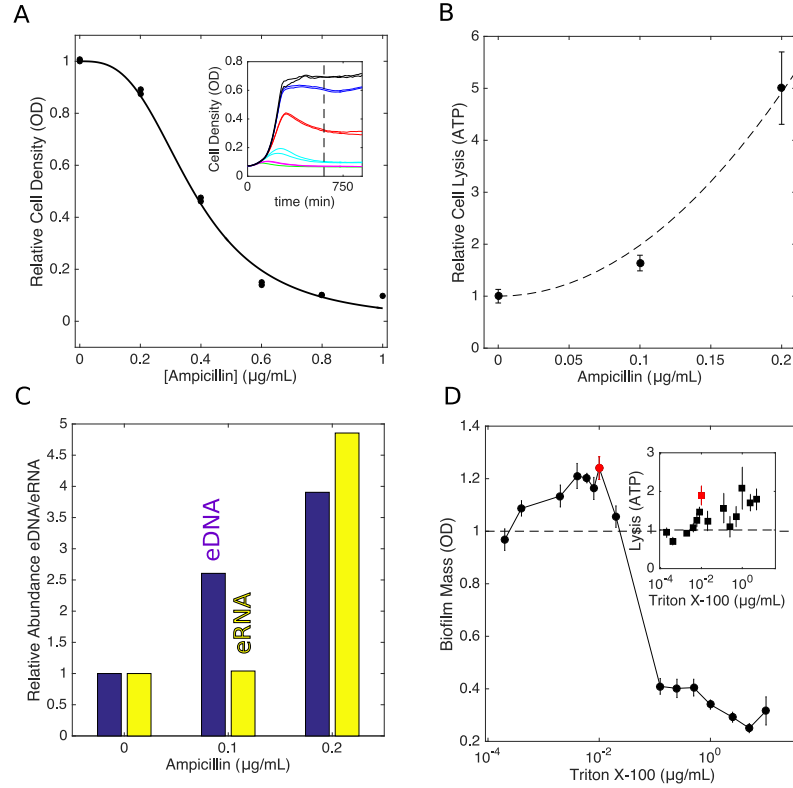
Figure 3.3: Enhanced biofilm formation occurs at sub-inhibitory concentrations and is associated with increased cell lysis and increased extracellular nucleic acid. A. Relative cell density (OD) approximately 10 hours after addition of ampicillin. Solid curve, fit to $(1 - (A/K_{50})^h)^{-1}$, with A the ampicillin concentration, $K_{50} = 0.38 \pm 0.01$ μg/mL the half maximal inhibitory concentration of the drug, and $h = 3$ a Hill coefficient. Inset: time series of optical density following drug exposure at time $t = 0$ for ampicillin concentrations of 0 (black), 0.2 μg/mL (blue), 0.4 μg/mL (red), 0.6 μg/mL (green), 0.8 μg/mL (magenta), and 1.0 μg/mL (cyan). B. Cell lysis (relative to untreated cells) as a function of ampicillin as measured by ATP assay (see Methods). Error bars are $\pm$ standard error of the mean from eight replicates. Dashed line, fit to $1 + a^2/r_{00}$, with a the ampicillin concentration (measured in units of the drug's half maximal inhibitory concentration (K_{50})) and $r_{00} = 0.010 \pm 0.001$. C. Abundance of extracellular DNA (eDNA, blue) or RNA (eRNA, yellow) as a function of ampicillin concentration. D. Triton X-100, a known inducer of cell lysis, enhances biofilm formation at low concentrations. Biofilm mass is measured by crystal violet assay (see Methods), and error bars are $\pm$ standard error of the mean from eight replicates. Inset: cell lysis (relative to untreated cells) as a function of Triton X-100 concentration. Red points correspond to peak in biofilm formation.
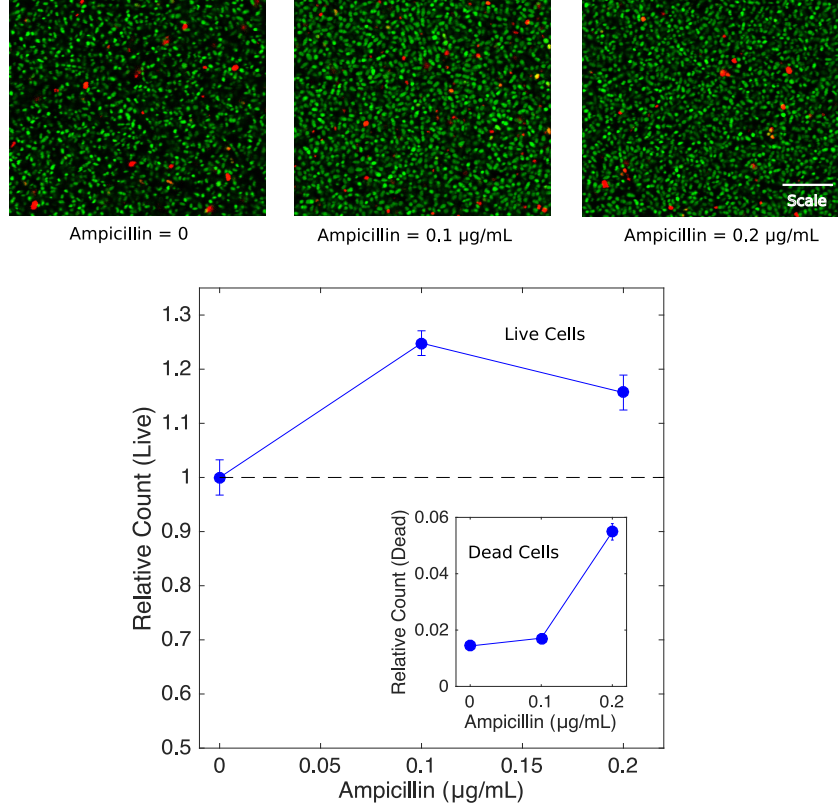
Figure 3.4: Enhanced biofilm formation corresponds to an increase in the number of living cells. Top panels: example laser scanning confocal images from biofilms exposed to ampicillin at different concentrations (0, left panel; 0.1 μg/mL, middle panel; 0.2 μg/mL, right panel) and post-treated with live (green) and dead (red) stains. Main panel: Relative count of live cells and dead cells (inset) as a function of ampicillin concentration. Counts are normalized relative to the total number of live cells in the absence of drug, which is set to 1. Error bars are $\pm$ standard error of the mean taken over a total of 48 two dimensional slices per condition (three z-slices of each biofilm and 16 total biofilms per condition).

merely an increase in non-living mass–than those formed in the absence of drug.

3.2.5 A simple mathematical model describes biofilm induction as a balance between beneficial cell lysis and costly drug efficacy

To quantify the trade-offs between antibiotic efficacy and "beneficial" cell lysis, we developed a simple mathematical model describing the number of living cells N and the number of lysed (dead) cells D in a biofilm. Specifically, we have

$$
\begin{aligned}
\frac{\partial N}{\partial t} &= g\left(1 - \frac{N}{K}\right)N - rN + cLD \\
\frac{\partial D}{\partial t} &= rN - \gamma D
\end{aligned}
\tag{3.1}
$$

In the first equation, the first term describes logistic growth (with per capita growth g and carrying capacity $K > 0$), the second describes cell death (lysis) with rate $r \geq 0$, and the last term describes the increase in biofilm mass due to surface attachment of living cells in the planktonic phase, a process which is coupled to the number of lysed cells D and controlled by a parameter $c > 0$. It is straightforward to show that models without this coupling do not exhibit a drug-induced maximum in biofilm mass (see SI). While the mechanism of coupling is not specified in the model, this term could describe eDNA-induced attachment of planktonic cells, assumed to occur at a rate proportional to both the living cells in solution (L) and the lysed cells in the biofilm (D). In the second equation, the first term accounts for cell lysis and the second term describes a decay of dead (lysed) cell material due to, for example, detachment from the biofilm. The model implicitly assumes that the effect of antibiotic on cells in the planktonic phase occurs on a fast timescale, allowing L to reach a steady state on the timescale of biofilm formation. This assumption is consistent with experimental measurements, where planktonic populations reach a steady state size after approximately 10 hours (Figure 3.3), while the biofilms we study are formed over a 24 hour period. The model includes two parameters, r and L, that depend on drug concentration, which we call a.

In the steady state, the living biofilm mass N is given by

$$\frac{N}{K} = 1 + r_0(a)\left(L_0(a) - 1\right), \tag{3.2}$$

where $r_0(a) = r(a)/g$ and $L_0(a) = cL(a)/\gamma$ are (rescaled) functions describing the rate of cell lysis and the number of living cells in planktonic solution as a function of drug, a. Equation 3.2 illustrates a simple balance between the biofilm-inducing properties of lysis (proportional to $L_0(a)$) and the biofilm reducing effects of lysis. A more detailed analysis shows that when $L_0(a) > 1$, the maximum biofilm mass
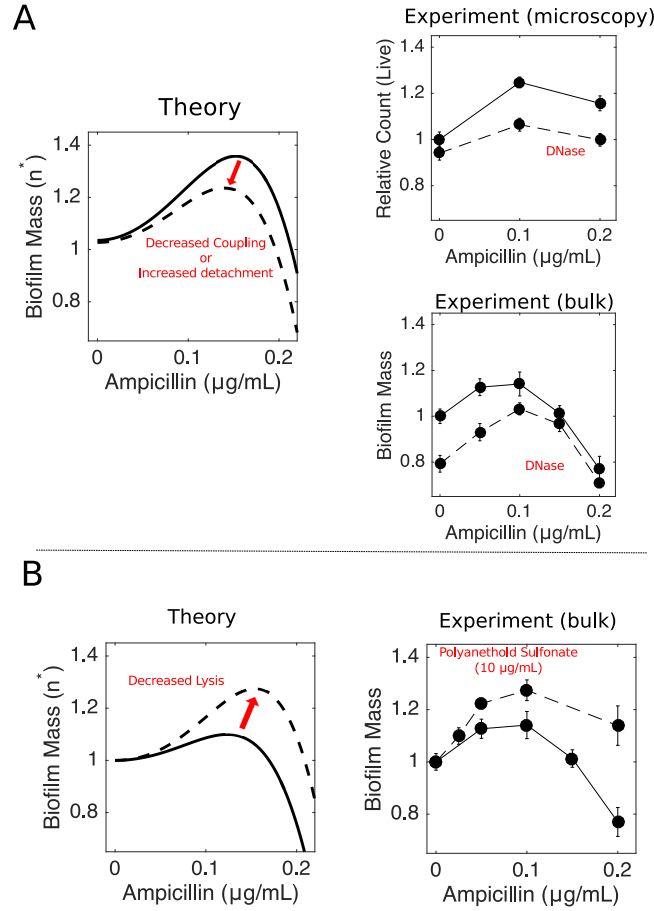
Figure 3.5: Minimal mathematical model predicts qualitative changes in peak location and height following external perturbations. A simple mathematical model that couples cell lysis to biofilm formation describes qualitative features of biofilm enhancement. The model contains two free parameters (ϵ and r_{01}) which can be estimated from the peak height and peak location in biofilm enhancement curves (e.g. Figure 3.1 or Figure 3.4). A. Left panel (Theory): Living biofilm mass (n^*, solid line) as a function of ampicillin for parameter values $\epsilon = 1.18 \pm 0.01$ and $r_{01} = 19 \pm 4$ estimated from living biofilm cell counts (i.e. solid curve in upper right panel). Dashed curve shows the predicted change in peak location and height due to perturbations that reduce the coupling ϵ by several percent. Right panels (Experiment): relative biofilm mass (solid curves) as a function of ampicillin from confocal microscopy (see also Figure 3.4) and bulk experiments (see also Figure 3.1). Dashed curves: identical experiments but with DNase added at a concentration of 400-500 μg/mL. B. Left panel (Theory): Living biofilm mass (n^*, solid line) as a function of ampicillin for parameter values $\epsilon = 1.09 \pm 0.02$ and $r_{01} = 18 \pm 6$ estimated from bulk experiments (i.e. solid curve in right panel). Dashed curve shows the predicted change in peak location and height due to perturbations that decrease cell lysis. Right panel (Experiment): relative biofilm mass (solid curve) as a function of ampicillin from bulk experiments (see also Figure 3.1). Dashed curves: identical experiments but with polyamethoid sulfonate, a known inhibitor of cell lysis, at a concentration of 10 μg/mL. Error bars represent $\pm$ standard error of the mean.

can occur for $a > 0$, i.e., the model exhibits a peak in biofilm mass at a non-zero concentration of drug (SI).

Fortunately, the functions $r_0(a)$ and $L_0(a)$ can each be estimated–up to a scaling constant–by independent experiments. Specifically, using the data in Figure 3.3 A, we take $L_0(a) = \epsilon/(1 + a^h)$, where $h = 3$ a Hill coefficient and a is measured in units of the drug's half-maximal inhibitory concentration, estimated to be $K_{50} = 0.38 \pm 0.01$ μg/mL. Similarly, based on the measurements in Figure 3.3 B, we take $r_0(a) = r_{01}(1 + a^2/r_{00})$, with $r_{00} = 0.010 \pm 0.001$. It should be noted that we assume a simple quadratic dependence of lysis on a to match the experimental measurements; this should be viewed as a simple parameterization of the experimental lysis measurements and does not imply any particular mechanism. The quadratic dependence of lysis on a could depend on complex pharmacological and pharmacodynamics of the antibiotics, and we do not attempt to model those here.

The remaining two parameters, ϵ and r_{01}, are scaling parameters that can be estimated from biofilm data. Because the measured value of $r_{00} << 1$, we can derive approximate solutions for the location (a_{max}) and height (p_h) of the biofilm peak (SI). Specifically, the peak location is given by

$$a_{max} \approx \left(\frac{2(\epsilon - 1)}{4 + \epsilon}\right)^{1/3} \tag{3.3}$$

and the peak height is given by

$$p_h \approx 1 + \frac{3}{5}\left(\frac{2}{5}\right)^{2/3} r_{01}(\epsilon - 1)^{5/3}. \tag{3.4}$$

It is clear from these expressions that an optimum in biofilm production occurs at a nonzero concentration a when $\epsilon > 1$, and the effect of further increasing ϵ is to shift the peak to higher a and increase its height.

3.2.6 Mathematical model predicts changes to peak height and location due to external perturbations

While it is straightforward to estimate ϵ and r_{01} from biofilm experiments–for example, $\epsilon = 1.09 \pm 0.02$ and $r_{01} = 18 \pm 6$ based on the bulk experiments in Figure 3.1 A–it is more instructive to consider the qualitative predictions of the model as parameters are varied. To express these scaling parameters in terms of the original (physical) parameters, let's write $L(a)$ as the product of a normalized drug-dependent component $(1/(1 + a^h))$ and a scaling constant α, which represents the number of living cells in planktonic phase at drug concentration $a = 0$. It is then clear that $\epsilon = \frac{c\alpha}{\gamma}$. Increasing ϵ therefore corresponds to 1) increasing the coupling between biomass material and lysis (c), 2) decreasing the decay rate of lysed cell material in the biofilm (γ), and/or 3) increasing the number of living cells in solution (α) at constant $a = 0$.

Our model predicts that perturbations that decrease ϵ will lower the peak height (Figure 3.5 A, left panel; Figure 3.7, bottom left). To test this prediction experimentally, we repeated both bulk and microscopy experiments in the presence of DNase. Because eDNA has been implicated as the molecular conduit linking cell lysis to biofilm formation, we expect DNase treatment to decrease ϵ by effectively lowering the coupling parameter c (that is, to reduce the beneficial effects of cell lysis). Indeed, biofilms treated with DNase exhibit lower peaks (Figure 3.5 A, right panels). It is worth noting that the model also predicts a slight shift in the location of the peak, but the resolution of the experimental data is insufficient to evaluate that prediction quantitatively. A second way of decreasing ϵ would be to decrease the number of living cells in planktonic phase (α). One possibility is to treat the cells with a second (non-lysis-inducing) antibiotic; indeed, treatments with tetracycline and rifampicin

decrease the height of the peak to almost zero (Figure 3.8), though we cannot rule out additional mechanisms, including interactions between the antibiotics.

Because the peak in biofilm production appears liked with cell lysis, one would expect chemical inhibitors of cell lysis to significantly impact the peak height and/or location, though the exact effects are not clear a priori. In terms of the model, the primary effect of decreasing cell lysis would be to shift $r_0(a) \to r_0(a) - \beta$, with β a positive constant (or equivalently, a shift in $r_{00} \to r_{00} - \beta/r_{01}$). While these effects would not be evident at the level of the approximate equations (Equations 3.3, 3.4), we can easily evaluate the predicted effects numerically (Figure 3.5B, left panel, and Figure 3.7, bottom right panel). Decreasing lysis is predicted to shift the peak location to higher drug concentrations and, somewhat counterintuitively, leads to an increase in the relative height of the peak. In words, a higher concentration of antibiotic is needed to achieve sufficient cell lysis to induce increased biofilm production.

To test this prediction experimentally, we repeated the experiment in the presence of polyamethoid sulfonate, a known inhibitor of cell lysis. Polyamethoid sulfonate inhibits cell lysis by approximately 40% in the absence of drug at the concentrations used (Figure 3.8). Indeed, treatment with the lysis inhibitor leads to a shift in optimal biofilm mass to higher drug concentrations and increases the relative size of the peak.

3.3 Discussion

Our work demonstrates that biofilm formation in E. faecalis is enhanced by subinhibitory concentrations of cell-wall synthesis inhibitors, but not by other classes of antibiotics. Enhanced biofilm is associated with increased cell lysis and an increase in eDNA and eRNA. We observed similar enhancement effects when cultures were

treated with non-antibiotic chemicals that induce similar amounts of cell lysis. To quantify the trade-off between drug toxicity and the beneficial effects of cell lysis, we developed a simple mathematical model that predicts changes to the magnitude and concentration-dependence of optimum biofilm formation induced by external perturbations that reduce eDNA, reduce living cells in the planktonic phase, or inhibit cell lysis.

Subinhibitory concentrations of antibiotics have been reported to promote biofilm formation in multiple species [67, 18], but studies in *E. faecalis* are relatively rare. Subinhibitory antibiotic concentrations have previously been shown to impact the physioelectrical [78] and adhesion behavior [79] of *E. faecalis*. In addition, low concentrations of tigecycline have been shown to reduce biofilm formation, even when growth of planktonic cells is not significantly affected [80]. To our knowledge, this is the first work to describe enhancement of biofilm formation due to cell wall synthesis inhibitors in *E. faecalis*.

While our findings are consistent with recent findings supporting the role of eDNA in biofilm formation, other mechanisms may also contribute to the observed increase in biofilm formation. For example, recent work has shown that eDNA is prevalent in biofilms even at the early developmental stages when cell lysis is minimal [81]. We cannot rule out contributions from similar non-lysis-based mechanisms for increasing eDNA to the observed biofilm enhancement. In addition, it is well-known that sub-MIC levels of antibiotic can dramatically alter gene expression profiles in bacteria [82, 83, 84], indicating that biofilm enhancement may arise from a complex combination of multiple factors.

We also stress that our mathematical model is a dramatic oversimplification of the complex biofilm-formation process. Computational models of biofilm forma-

tion may contain dozens or even hundreds of microscopic parameters, yet even the most elaborate mathematical models neglect biological details at some scale. Our approach was not to develop a detailed microscopic model, but rather to develop a simple, minimal model to help intuitively explain and predict the trade-offs between antibiotic efficacy and beneficial cell lysis at the population level. Linking our model with more detailed agent-based simulations may help us further understand the potential role of spatial structure and heterogeneity in drug-induced biofilm formation. For example, recent work has shown that in the absence of drug, *E. faecalis* biofilm formation depends on a phenotypic bistability in gene expression, giving rise to lysis-susceptible and lysis-inducing sub-populations [69, 70, 71, 72, 73]. It would be interesting to further explore the interplay between this multi-modal population structure and drug-induced lysis observed in this work.

Our work also raises intriguing questions about how genetic resistance determinants might spread in biofilm populations, even in the absence of the strong selection pressure of high drug concentrations. A quantitative understanding of biofilm formation may also inspire new optimized dosing protocols, similar to those in, for example, [85, 86, 87] developed for planktonic populations. In the long run, these results may lay the groundwork for improved, systematic design of biofilm-specific therapies [88, 89].

3.4 Supplemental Information

3.4.1 Mathematical Model

To model lysis-induced biofilm formation, we consider a simple model given by

$$
\begin{aligned}
\frac{\partial N}{\partial t} &= g\left(1 - \frac{N}{K}\right)N - rN + cLf(D) \\
\frac{\partial D}{\partial t} &= rN - \gamma D
\end{aligned}
\tag{3.5}
$$

where N is the number of living cells in the biofilm, D is the number of dead (lysed) cells, and L is the number of living cells in the planktonic media. In the first equation, the first term describes logistic growth (with per capita growth g and carrying capacity $K > 0$), the second describes cell death (lysis) with rate $r \geq 0$, and the last term describes the increase in biofilm mass due to surface attachment of living cells in the planktonic phase. When $f(D)$ is a constant, cells attach to the biofilm at a rate proportional to the number of cells in the planktonic phase ($L > 0$) times a rate parameter $c > 0$; more general choices for $f(D)$ couple biofilm induction to cell lysis, which we show below is required to achieve a peak in N as a function of lysis. In the second equation, the first term accounts for cell lysis and the second term describes a decay of dead (lysed) cell material due to, for example, detachment from the biofilm. The model includes two parameters, r and L, that depend on drug concentration, which we call a. In what follows, we begin our analysis under mild assumptions on $r(a)$ and $L(a)$. Then, for a more detailed analysis, we resort to specific functional forms which can be estimated, up to a scaling constant, directly from experimental data.

3.4.2 Biofilm formation uncoupled from lysis

We first consider a simple case where biofilm formation is uncoupled from cell lysis, i.e. $f(D) = \text{constant}$ (which we subsume into the constant c without loss of generality). In this case, Equation 3.5 can be written in terms of dimensionless variables $n = N/K$, $d = Dg/(Kr)$, and rescaled time $\tau = tg$ as

$$
\begin{aligned}
\frac{\partial n}{\partial \tau} &= (1 - n)\, n - r_0 n + L_0 \\
\frac{\partial d}{\partial \tau} &= n - \gamma_0 d
\end{aligned}
\tag{3.6}
$$

where $r_0 = r/g$, $L_0 = cL/(gK)$, and $\gamma_0 = \gamma/g$. In the steady state, we have

$$n^* = \frac{1}{2}\left(1 - r_0 + \sqrt{(1-r_0)^2 + 4L_0}\right)$$

$$d^* = \frac{1}{2\gamma_0}\left(1 - r_0 + \sqrt{(1-r_0)^2 + 4L_0}\right)$$

(3.7)

where we have kept only the physically meaningful (positive) root. It is straight-forward to show that this steady state is always a stable fixed point ($\operatorname{tr} J < 0$ and $\det J > 0$, where J is the Jacobian of the system in Equation 3.6 evaluated at (n^*, d^*)).

It is intuitively clear that this model does not exhibit a non-zero peak in n^* as a function of antibiotic a. Recall that the dependence on a arises from $r_0(a)$ and $L_0(a)$, which are functions of drug concentration. If we make the physically reasonable assumptions that, for $a > 0$, $r_0'(a) > 0$ (lysis increases with drug) and $L_0'(a) < 0$ (planktonic cells decrease with drug)–both of which are consistent with experimental measurements–the derivative of $n^*(a)$ is always negative. Specifically, we have

$$\frac{\partial n^*(a)}{\partial a} = \frac{1}{2}\left(r_0'(a)(\lambda - 1) + \frac{2L_0'(a)}{\sqrt{4L_0(a) + (r_0(a) - 1)^2}}\right)$$

(3.8)

where primes indicate differentiation with respect to a and $\lambda = \frac{r_0(a) - 1}{\sqrt{4L_0(a) + (r_0(a) - 1)^2}}$. Because $|\lambda| \leq 1$, both terms are negative, indicating that $n^*(a)$ is always decreasing and cannot exhibit a maximum for $a > 0$.

3.4.3 Biofilm formation coupled to lysis

To capture experimental observations in a minimal model, we consider Equation 3.5 with $f(D) = D$, so that the number of dead (lysed) cells is coupled to living biofilm mass. We can write Equation 3.5 in terms of rescaled variables $n = N/K$, $d = Dg/(Kr)$, and $\tau = tg$ as

$$\frac{\partial n}{\partial \tau} = (1 - n)\,n - r_0 n + L_0 r_0 d$$

$$\frac{\partial d}{\partial \tau} = n - \gamma_0 d$$

(3.9)

where $r_0 = r/g$, $L_0 = cL/\gamma$, and $\gamma_0 = \gamma/g$. In the steady state, we have

$$n^* = 1 + r_0 (L_0 - 1)$$

$$d^* = \frac{1}{\gamma_0} (1 + r_0 (L_0 - 1))$$

(3.10)

We restrict our analysis to the physically-meaningful regime $r_0(1 - L_0) \leq 1$, where the steady state values n^* and d^* are positive semi-definite. In this regime, the steady state solution Equation 3.10 is always a stable fixed point ($\text{tr} J < 0$ and $\det J > 0$, where J is the Jacobian of the system in Equation 3.9 evaluated at (n^*, d^*)).

To look for a peak in biofilm (living) mass as a function of a, we again consider $r_0 \to r_0(a)$ and $L_0 \to L_0(a)$ with $r_0'(a) > 0$ (lysis increases with drug) and $L_0'(a) < 0$ (planktonic cells decrease with drug). Differentiating Equation 3.10 with respect to a, we have

$$\frac{\partial n^*(a)}{\partial a} = r_0(a)L_0'(a) + (L_0(a) - 1) r_0'(a).$$

(3.11)

It is clear that $\frac{\partial n^*(a)}{\partial a} \leq 0$ when $L_0(a) \leq 1$. However, an optimum ($\frac{\partial n^*(a)}{\partial a} = 0$) can occur when L_0 is sufficiently large, i.e. when

$$L_0(a) = \left| \frac{r_0(a)L_0'(a)}{r_0'(a)} \right| + 1$$

(3.12)

In words, the existence and location of an optimum is determined by properly scaled functions–and the corresponding first derivatives–describing lysis ($r_0(a)$) and the decay of living cells in the planktonic phase ($L_0(a)$) as a function of drug. Both of these functions can be independently measured–up to a scaling constant–in our experiments. In turn, these two scaling constants become free parameters which can be estimated, for example, from the peak height and peak location in our biofilm experiments.

To make further analytical progress, we assume that $r(a)$ and $L(a)$ take the fol-
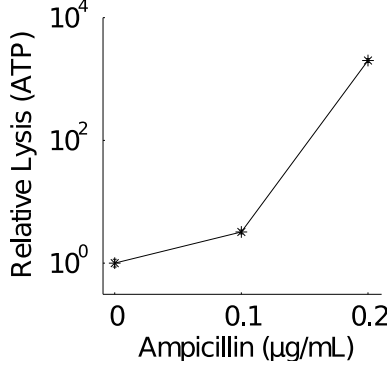
Figure 3.6: Subinhibitory concentrations of ampicillin increase cell lysis in planktonic populations.

lowing functional forms

$$r_0(a) = r_{01}(r_{00} + a^2)$$
$$L_0(a) = \frac{\epsilon}{(1 + a^h)}$$
(3.13)

where r_{00} and r_{01} describe the increase in lysis as a function of a, ϵ is a positive definite parameter that captures the effective coupling between biofilm formation and cell lysis, h is a hill coefficient, and a is measured in units of the drug's half-maximal inhibitory concentration (IC50). Based on experimental measurements (Figure 3.3), we estimate $r_{00} = 0.010 \pm 0.001 << 1$, $h = 3.2 \pm 0.2$, and the drug's IC50 is given by 0.38 ± 0.01 μg/mL. For mathematical simplicity, we take $h = 3$ in what follows. As we will see, the remaining two parameters (ϵ and r_{01}) determine the location and the height of the peak in biofilm production as a function of a.

Plugging Equations 3.13 into Equation 3.12 yields a nonlinear equation that can be solved numerically to yield the peak location a_{max},

$$2a_{max}^6 + (4 + \epsilon)a_{max}^3 + 3\epsilon r_{00}a_{max} + 2(1 - \epsilon) = 0.$$
(3.14)

It is clear that Equation 3.14 has $a_{max} > 0$ solutions only when $\epsilon > 1$. Because we expect this peak to occur in the subinhibitory regime of antibiotic concentration, we assume $a << 1$ and ignore the sixth order term to give

$$a_{max}^3 + \delta a_{max} + \omega = 0$$
(3.15)

63
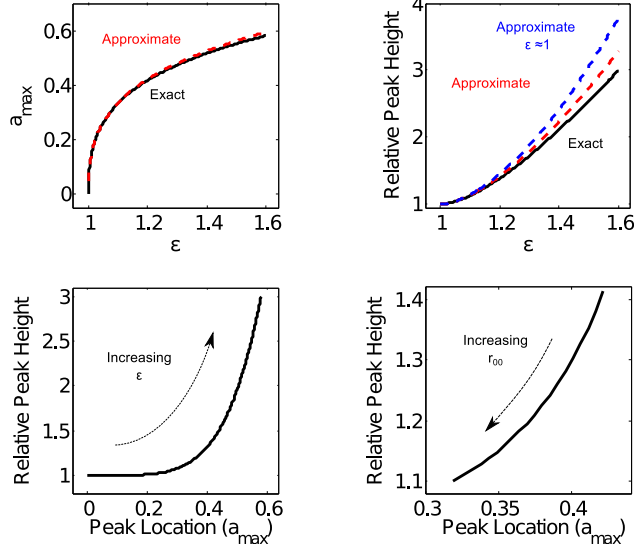
Figure 3.7: Changes in ϵ and r_{00} shift peak location and peak height. Top left: Approximate equation for peak location (Equation 3.19, red dashed) and exact value (black). Top right: Approximate equation for peak height (Equation 3.20, red dashed), $\epsilon \approx 1$ expansion (Equation 3.21, blue dashed) and exact value (black). Bottom left: Peak height vs. peak location (exact) for $1 \leq \epsilon \leq 1.6$. Bottom right: Peak height vs. peak location (exact) for $0 \leq r_{00} \leq 0.2$. Parameters r_{00}, r_{01} and ϵ were chosen to match the range observed in experiments. $r_{01} = 20$ for all panels. $r_{00} = 0.01$ for top panels and bottom left panel. $\epsilon = 1.2$ for bottom right panel.

with $\delta \equiv \frac{3\epsilon r_{00}}{4+\epsilon}$ and $\omega \equiv \frac{2(1-\epsilon)}{(4+\epsilon)}$. Since r_{00} is estimated to be on the order of 10^{-2}, we assume $\delta << 1$ and expand a_{max} in a power series as

$$a_{max} = a_0 + a_1\delta + ... \tag{3.16}$$

Subbing this expression into Equation 3.15 and equating like powers of δ, we have

$$a_0 = (-\omega)^{1/3} = \left(\frac{2(\epsilon - 1)}{4 + \epsilon}\right)^{1/3} \tag{3.17}$$

and

$$a_1 = -\frac{1}{3a_0} = -\frac{1}{3\left(\frac{2(\epsilon-1)}{4+\epsilon}\right)^{1/3}}. \tag{3.18}$$

To first order in δ, then, the peak location is given by

$$a_{max} = \left(\frac{2(\epsilon - 1)}{4 + \epsilon}\right)^{1/3} - \frac{\epsilon r_{00}}{(4 + \epsilon)^{2/3}\left(2(\epsilon - 1)\right)^{1/3}} \tag{3.19}$$

We can also plug Equation 3.19 into the expression for n^* (Equation 3.10) to get an expression for the peak height, p_h. The full expression is cumbersome, even to first
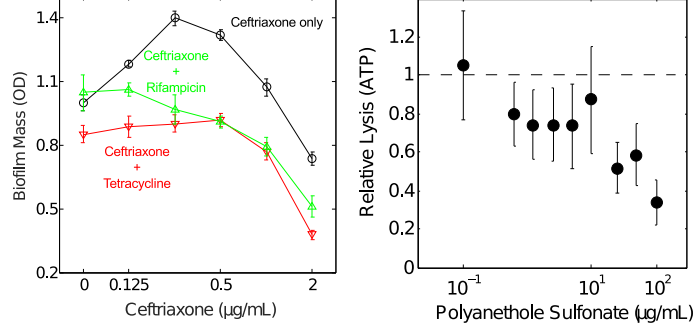
Figure 3.8: Left panel: Addition of a second (non-lysis-inducing) drug reduces the height of the biofilm peak. Black circles: ceftriaxone only. Green triangles: ceftriaxone combined with rifampicin (0.3 μg/mL). Red triangles: ceftriaxone combined with tetracycline (0.2 μg/mL). Right panel: polyamethoid sulfonate reduces cell lysis.

order in δ, but the 0th order approximation ($\delta = 0$) is given by

$$p_h = 1 + \frac{2^{2/3}(\epsilon^2 + \epsilon - 2)r_{01}}{2 + 3\epsilon}\left(\frac{\epsilon - 1}{4 + \epsilon}\right)^{2/3} \tag{3.20}$$

For ϵ just above 1, the expression can be expanded to yield

$$p_h \approx 1 + \frac{3}{5}\left(\frac{2}{5}\right)^{2/3} r_{01}(\epsilon - 1)^{5/3} \tag{3.21}$$

which makes it clear that increasing ϵ increases the peak height.

Figure 3.7 shows that the approximate solutions derived above capture the ϵ dependence of peak height and peak location well (top panels). The model predicts that increasing ϵ leads to an increase in both peak height and peak location (bottom left panel). On the other hand, increasing r_{00} leads to a decrease in both peak height and peak location (bottom right panel). It's instructive to consider these trends in terms of the original model parameters. Rewriting Equation 3.13 in terms of the original model parameters, we have

$$\frac{cL(a)}{\gamma} = \frac{\epsilon}{(1 + a^h)}. \tag{3.22}$$

Let's write $L(a)$ as the product of a normalized drug-dependent component ($1/(1 + a^h)$) and a scaling constant α that describes a-independent changes in the number of

living cells in solution. It is then clear that $\epsilon = \frac{c\alpha}{\gamma}$. Increasing ϵ therefore corresponds to 1) increasing the coupling between biomass material and lysis (c), 2) decreasing the decay rate of lysed cells (γ), and/or 3) increasing the number of living cells in solution (α) at constant a. In terms of experimental perturbations, ϵ could be decreased by treating biofilms with DNase, which underlies the hypothesized biological coupling between lysis and biofilm formation. This treatment would therefore be expected to decrease c. A second way of decreasing ϵ would be to decrease the number of living cells in planktonic phase (α). One possibility is to treat the cells with a second (non-lysis-inducing) antibiotic; indeed, treatments with tetracycline and rifampicin decrease the height of the peak to almost zero (Figure 3.8), though we cannot rule out additional mechanisms, including interactions between the antibiotics.

CHAPTER IV

Spatial Pattern Formation in Antibiotic Resistant Bacterial Populations

4.1 Introduction

There are numerous observations of spatial patterns formed by different species of bacteria grown in non-liquid media [90]. An example of interesting pattern formation is a series of concentric rings formed by *Escherichia coli* on semi-solid agar plates and was reported in early 1991 [91]. Bacterial growth patterns can vary dramatically as growth conditions, such as medium type, the amount of nutrients, and hardness of agar surface, are varied; transitions between morphotypes can be seen by altering these factors. For example, bacteria can move faster and form compact patterns on plates with more nutrients or less agar. However, on poor media plates, some bacteria can have branching shaped patterns via group motility or chemical signals [92]. When exposed to antibiotic stress, a larger variety of growth patterns can be observed due, in part, to unfavorable environmental stress [93].

These works have revealed large-scale bacterial coordination within colonies which have, in turn, contributed to a deeper understanding of microbial evolution and genetics. The results have also led to the development of new theoretical models, including reaction-diffusion aggregation [94] and the walker model [95], which have been used to successfully predict spatial patterns in some cases [96]. The meth-

ods are particularly useful for populations containing a single species, but they are not easily extended to mixtures of two or more species. On the other hand, in the absence of cooperation/competition interactions, so called "stepping stone" models (see Section 4.1.1) have been especially powerful for explaining genetic demixing phenomenon, with large scale experimental observables linked–in some cases–to analytical expressions containing microscopic parameters. Unfortunately, despite the great success of these models for non-interacting populations, they often fail to describe complex interaction phenomena observed in real experiments containing multiple species.

In this chapter, we investigate pattern formation in mixed bacterial populations containing antibiotic sensitive and antibiotic resistant strains of the same species (either *E. coli* or *E. faecalis*). In both species, antibiotic resistance is conferred by over-expression of the enzyme β-lactamase, which degrades drugs from the β-lactam class (in our case, ampicillin). Similar types of enzyme-mediated resistance have recently shown to be a cooperative phenomenon in both liquid cultures [97] and in microscopic colonies [98], allowing sensitive cells to survive in the presence of resistant cells, even at high drug concentrations. However, little is known about how this cooperation might impact spatial pattern formation in mixed populations exposed to drug, though a deeper understanding of the phenomenon could provide insight into theoretical population dynamics while also enriching our understanding of how drug resistance determinants spread in microbial communities.

While the *E. coli* and *E. faecalis* resistant strains both exhibit resistance via enzyme production and the associated drug degradation, they differ in important ways that may impact pattern formation. First, *E. coli* are mobile bacteria which exhibit self-propelled motility on soft agar; by contrast, *E. faecalis* are typically not

motile. In addition, *E. faecalis* are round (coccus), while *E. coli* are rod-shaped; such microscopic shape differences have been recently predicted to influence large-scale colony growth [99].

In what follows, we first review the stepping stone model (Section 4.1.1) and show how it can be used to estimate microscopic parameters (diffusion constants) in simple microbial populations. Then, we discuss our experiments used to measure the velocity of colony expansion and segmentation using time-resolved scanning and fluorescence microscopy, first in single-species populations and later in more complex situations. We demonstrate experimentally that populations of *E. coli* and *E. faecalis* both exhibit features of cooperative drug resistance but shown dramatically different spatial patterns. Finally, we briefly discuss how adaptations of a stochastic lattice model will allow us to quantitatively investigate the different patterns and density effects observed experimentally.

4.1.1 Stepping Stone Model

Stepping stone model was proposed by Motoo Kimura in 1964 [100] and is very useful to study spatial segmentation of bacterial populations. Similar to the Wright-Fisher and Moran models [101], this model includes genetic drift, selection, migration and mutation. It can be extended to study high dimensions and a large number of alleles; for simplicity, however, here we use the one-dimensional model and consider only two alleles which can approximate the population expansion front with low cell density.

Assume there is an infinite array of colonies which are separated by distance L and each colony can have N_0 individual cells with two alleles. During every generation, a random individual selected from each colony can grow and another individual would die at the same time. But due to selection, individual with different alleles can have

different growth rates. The individual with allele one would be chosen to grow with probability $w_1 f/(w_1 f + w_2(1 - f))$, where f is fraction of allele one in each colony, w_1 and w_2 are growth rates of allele one and two respectively. Their offspring can mutate from allele one to two with a probability μ_{12} or from allele two to one with a probability μ_{21}. Individuals can also migrate to left or right neighbor colonies with a probability of $m/2$. In the continuous space limit, we can derive the equation for f,

$$\frac{\partial f}{\partial t} = D_s \frac{\partial^2 f}{\partial x^2} + sf(1 - f) + \mu_{21} - (\mu_{12} + \mu_{21})f + \sqrt{D_g f(1 - f)}\,\Gamma, \qquad (4.1)$$

where Γ is a white noise and arises from random genetic drift within each colony, $D_s = mL^2/2$ and $s = 2(w_1 - w_2)/(w_1 + w_2)$. We calculate spatial heterozygosity H as a measurement of degree of spatial assortment, and it is close to 0 when local extinction occurs. The equation for H is given by

$$H(t, x_1 - x_2) = \langle f(t, x_1)(1 - f(t, x_2)) + f(t, x_2)(1 - f(t, x_1)) \rangle, \qquad (4.2)$$

where the bracket means average over all possible locations.

If there is no selection process, which means an individual with allele one has the same fitness as the individual with allele two, and if we also ignore mutation process, then equation of H in polar coordinates is [102],

$$\frac{\partial H(t, \phi)}{\partial t} = \frac{2D_s}{(R_0 + vt)^2}\frac{\partial^2 H(t, \phi)}{\partial \phi^2} - \frac{D_g}{R_0 + vt}H(t, 0)\delta(\phi), \qquad (4.3)$$

where ϕ is the angle, R_0 is initial radius of sample droplet, v is expansion velocity, D_g is genetic diffusion constant and D_s spatial migration constant. H is given as

$$H(t, \phi_1 - \phi_2) = \langle f(t, \phi_1)(1 - f(t, \phi_2)) + f(t, \phi_2)(1 - f(t, \phi_1)) \rangle. \qquad (4.4)$$

It is possible to solve equation 4.3 exactly and calculate the number of isolated

sectors N when t is very large [102],

$$N(t \to \infty) = \frac{2\pi H(0, \phi)v}{D_g} + H(0, \phi)\sqrt{\frac{2\pi R_0 v}{D_s}}. \qquad (4.5)$$

Since N is linear with $\sqrt{R_0}$, by varying radius of initial sample and counting sector numbers in experiment, we will be able to calculate diffusion constants from this equation by least-squares fitting [103].

Unfortunately, if selection, mutation or cooperation plays an important role in the dynamics, the analytical calculation is significantly more complicated [104] [102] and the differential equations can not be solved analytically because the hierarchy of moment equations does not close. In what follows, we will see that the stepping stone model above provides accurate estimates of simple population dynamics for our system in the absence of antibiotic, but more complex models are required to describe the cooperative and density-dependent pattern formation observed in the presence of antibiotic.

4.2 Results

4.2.1 Quantitative Measurements of Colony Growth and Segmentation

As described in Chapter V, I used a commercial document scanner, customization of previously developed Matlab code [105], and fluorescence microscopy to measure pattern formation and dynamics during colony growth. To visualize the bacteria, we labeled wild-type (blue) and resistant (red) strains of both *E. coli* and *E. faecalis* using previously available reporter plasmids that constitutively express fluorescent proteins of the appropriate color. By scanning the plates over time, I collected time series of colony growth and used it to estimate expansion velocity and then used fluorescence microscopy to image colonies at the final time step and observe segmented regions. This experimental setup is convenient because on each agar plate, multiple
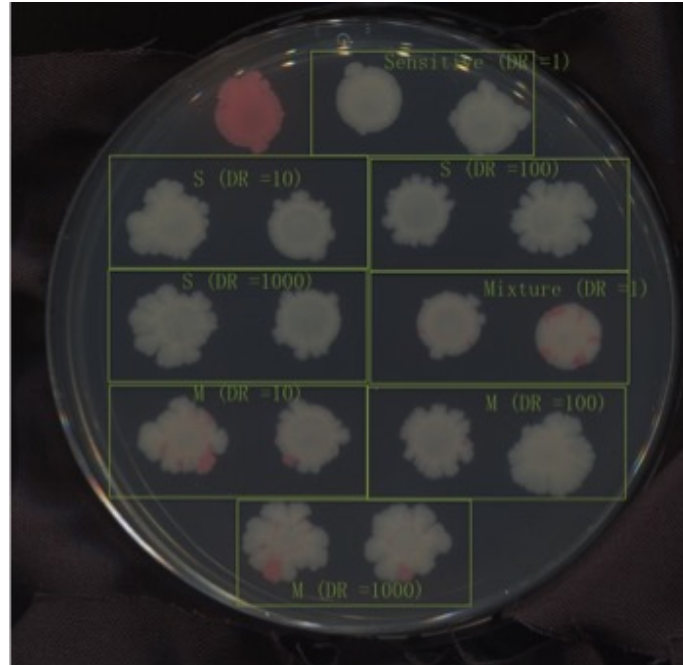
Figure 4.1: Scanner image of one plate without ampicillin. Fraction of resistant cells is 0.1. Dilution rates are 1, 10, 100 and 1000.

colonies can be grown and measured at the same time. When studying cooperation between resistant and sensitive cells, different concentrations of antibiotic ampicillin (AMP) will be added into the agar plates. As mentioned previously, resistant strains can express β-lactamase enzyme which can break down the β-lactam ring structure of antibiotic and thus deactivate its antibacterial activity. Sensitive cells will also benefit from this process and have a chance to survive in the hostile environment.

The sample volume, population composition (fraction of resistant cells), and the dilution level (overall population density) of the initial sample can be easily varied to explore their effects on pattern formation. Figure 4.1 shows the scanner image of a plate without AMP. Different colonies represent different resistant fractions and different initial dilutions (initial population densities). As one might expect, stochastic fluctuations lead to a roughening of the colony frontier when dilution rate is high or initial cell density is low.
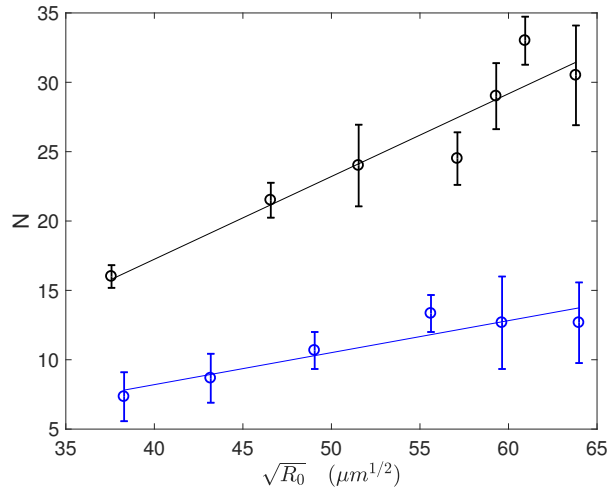
Figure 4.2: Number of sectors as a function of square root of radius. Black curve is least-squares fitting and initial fraction of resistant cells in mixture is 0.5. Blue curve is least-squares fitting and initial fraction of resistant cells in mixture is 0.1.

4.2.2 Pattern formation in Drug-Resistant *Escherichia coli* Communities

In Section 4.1.1, it is shown that number of isolated sectors is linear with square root of initial radius of the sample when there is no selection pressure and mutation. To confirm this prediction, we varied the initial radius of the colony by using different volumes of samples, and then 1) measured time series of colony radii and 2) counted the number of sectors at the final time point, after 3 days incubation. In figure 4.2, we use theoretical predictions from the stepping stone model to estimate diffusion constants in mixtures of drug sensitive and drug resistant *E. coli* in the absence of drug.

The average velocity of expansion is about $1.72 \pm 0.05 \times 10^{-2}$ μm/s. The initial radius is about 2.8 mm for 3 μL sample and can vary a lot among different droplets even with the same volume. It looks like the droplet with mixture inside would expand as a whole for a little bit (0.2 mm) and then start segmentation.
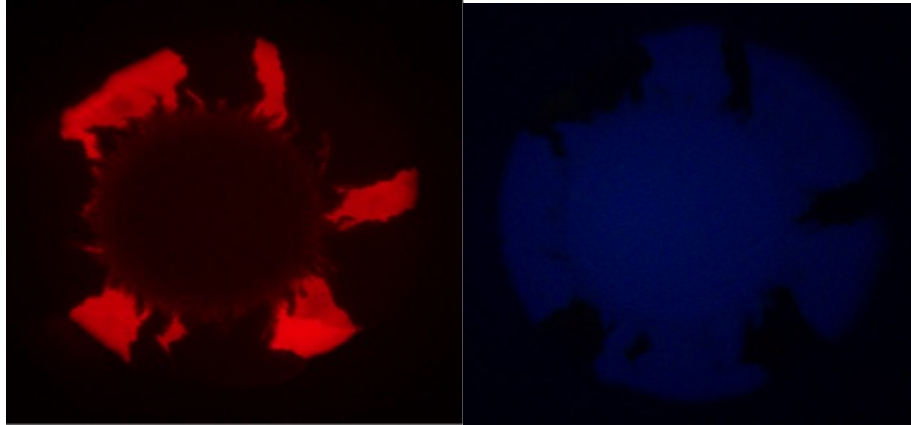
(a) Microscope image of one resistant colony without dilution.

(b) Microscope image of one sensitive colony without dilution.
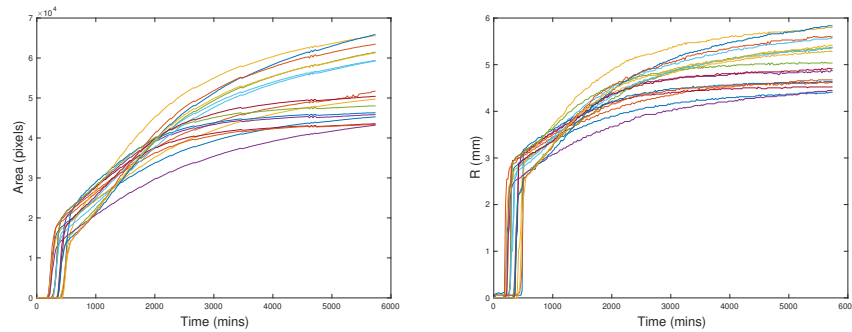
(c) Area of each colony on one plate as a function of time.

(d) Radius of each colony on one plate as a function of time.

Figure 4.3: ScanLag and Microscope images of one plate without ampicillin. Note that the early-time measurements in c and d are not accurate because we will detect many small separated cells within initial droplet area until they merge to one large colony.
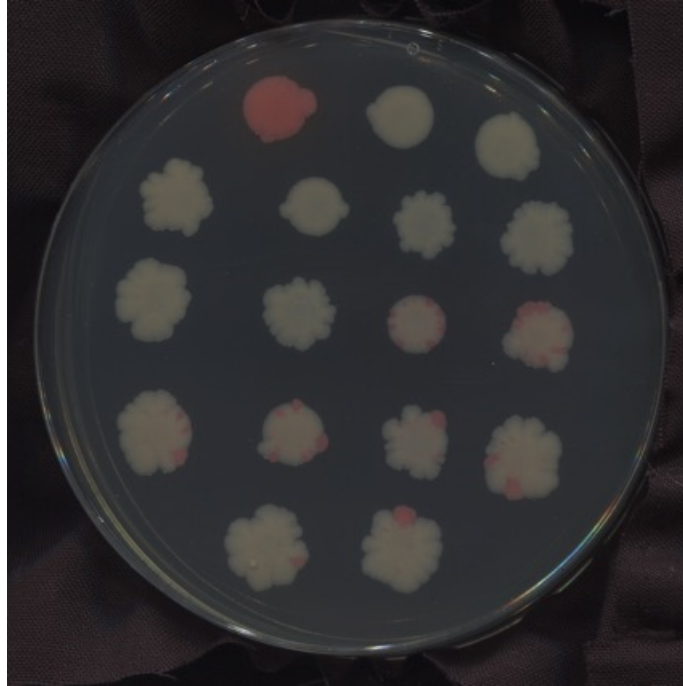
Figure 4.4: Scanner image of one plate with 1 μg/mL ampicillin. Dilution rates are 1, 10, 100 and 1000.

4.2.2.1 Founder cell density has enhanced impact on segmentation in the presence of ampicillin

In the presence of antibiotic, we expect that spatial pattern formation will exhibit evidence of cooperation. To investigate this question, we repeated the mixed-species experiments in the presence of ampicillin. First, in the absence of drug, we found that decreasing the number of founder cells (with a fixed starting volume) leads to a higher degree of assortment (less segmentation), an effect that is predicted by Equation 4.5. However, the effects of founder cell density are considerably enhanced in the presence of antibiotic (Figures 4.4 and 4.5). A similar phenomenon was recently observed in two cooperative strains of *Bacillus subtilis* on agar plates, though the mechanism of cooperation was significantly different [106]. Our observations could be partially explained by cooperation, and a full quantitative analysis is currently in progress (see below).
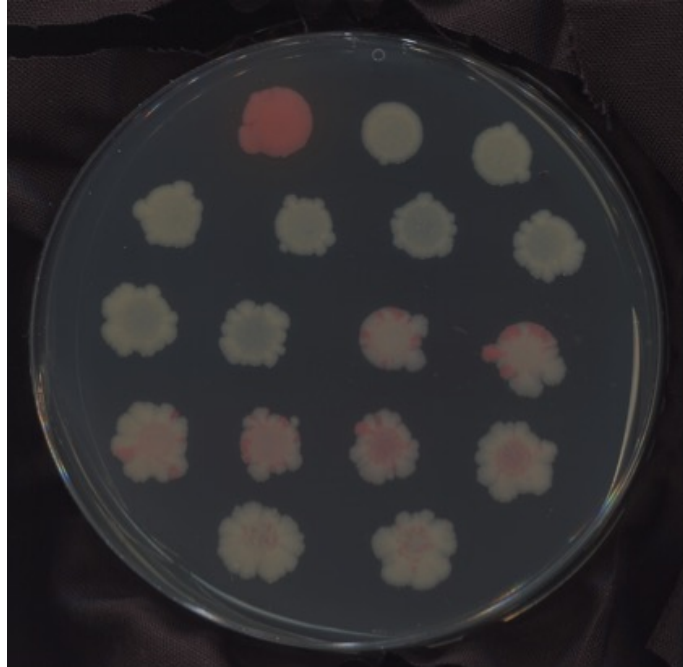
Figure 4.5: Scanner image of one plate with 2 μg/mL ampicillin. Dilution rates are 1, 10, 100 and 1000.

4.2.2.2 High drug concentrations affect appearance time for initial colony but not final colony size

We also observe several other trends in the presence of ampicillin. At low concentrations ($<$ MICs), the final colony area and radius are very similar to the drug free (no AMP) case (Figure 4.4). However, as ampicillin concentration is increased (Figures 4.5 and 4.6) the final colony sizes can be comparable with the no AMP case, even though the appearance time for sensitive colonies alone can be much longer. It's possible that these delays indicate the presence of so-called "persister cells", which are drug-tolerant and start to grow after a long incubation time [107]. In addition, we observe local segmentation in the middle of the colony when dilution rate is high in figure 4.6 (b).
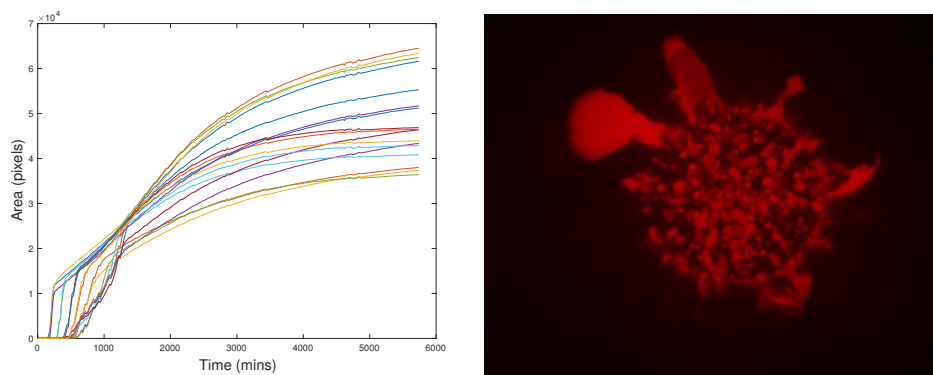
(a) Area of each colony on one plate as a function of time.

(b) Microscope image of one resistant colony with dilution rate 100.

Figure 4.6: ScanLag and Microscope images of one plate with 2 μg/mL ampicillin.

4.2.2.3 Fraction of resistant cells depends on antibiotic concentration and initial cell density

As ampicillin concentration is increased, we found that resistant cells will become dominant at higher dilution rates (see Figure 4.7; compare two colonies in right side of third row which has no dilution, and last two colonies at the bottom which has 1000 dilution rate). These results are consistent with recent results in liquid culture, where the fraction of resistance cells at stationary phase is proportional to antibiotic concentration and inversely proportional to initial cell density [97]. In addition, we found that the shape of the resistant cell colonies, as shown in figure 4.8, will change dramatically when dilution rates are increased.

4.2.2.4 Sensitive cells do not survive high antibiotic concentrations unless initial population density is sufficiently high

In figure 4.9, we see that sensitive cells will not grow at low initial densities due to high concentration of antibiotic, but they can survive in a mixed population as long as the initial population density is sufficiently high. The microscope images for mixture colonies with high dilution rates are purely red with no special structures inside.
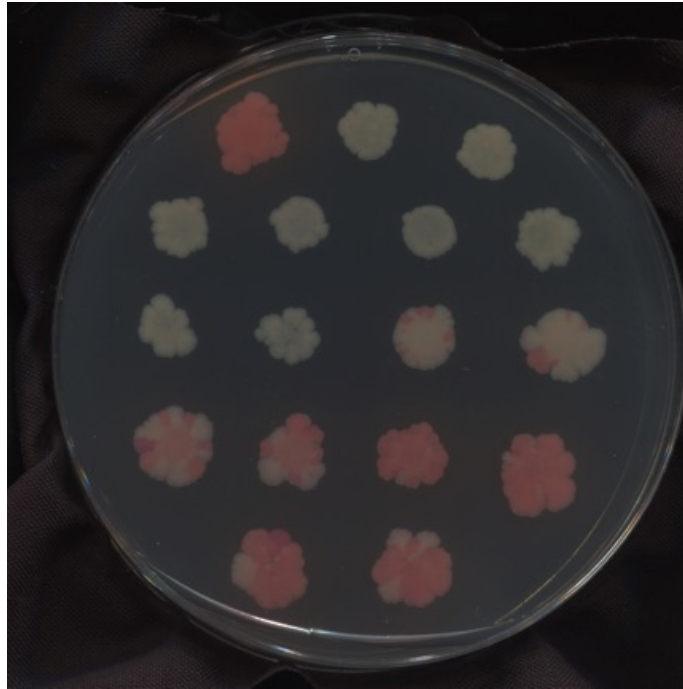
Figure 4.7: Scanner image of one plate with 3 μg/mL ampicillin. Dilution rates are 1, 10, 100 and 1000.
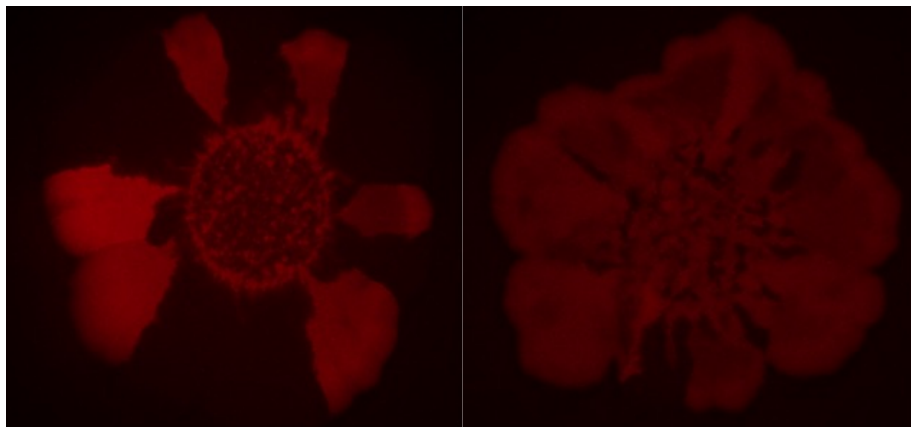
(a) Microscope image of one resistant colony with dilution rate 10.

(b) Microscope image of one resistant colony with dilution rate 100.

Figure 4.8: Microscope images of one plate with 3 μg/mL ampicillin.
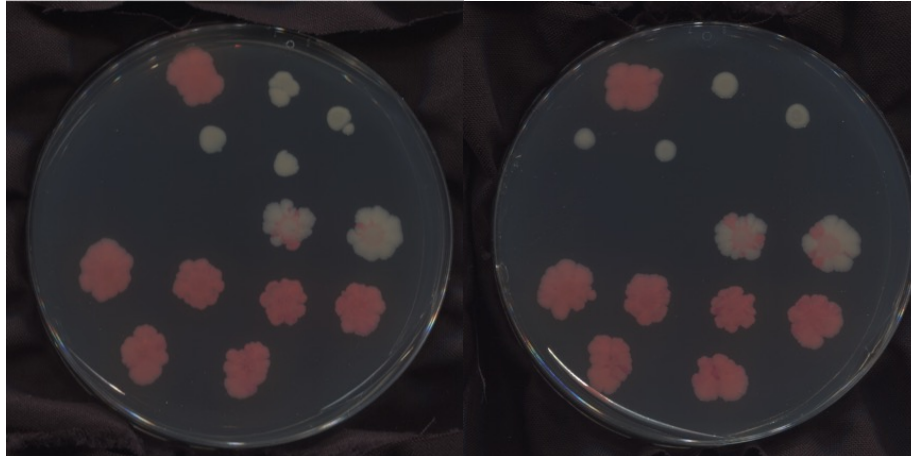
(a) Scanner image of one plate with 4 μg/mL ampicillin. (b) Scanner image of one plate with 5 μg/mL ampicillin.

Figure 4.9: Scanner images of one plate. Dilution rates are 1, 10, 100 and 1000.

4.2.3 *Enterococcus faecalis* **exhibit dramatically different spatial patterns and dynamics than** *E. coli*

E. faecalis exhibit significantly different colony morphologies and spatial patterns than those observed in *E. coli*. As shown in figure 4.10, colonies are compact with a significantly smoother front. In addition, microscope figures 4.11 also showed very different shapes. When rod-like cells (*E. coli*) mixed together, they tend to have fractal shape, whereas coccal cells (*E. faecalis*) show clear vertical boundaries through the colony, a finding that is consistent with recent work indicating that cell morphology can greatly affect bacterial spatial pattern [99].

As shown in figure 4.12, size of each colony is smaller than *E. coli* and expansion velocity is about $6.65 \pm 0.08 \times 10^{-3}$ μm/s, which is almost half of that for *E. coli*. This velocity is comparable with some other motile species [103], but we have to know that colony expansion is also related to nutrient concentration, agar concentration, medium type and so on.

As concentrations of ampicillin increased, sensitive cells die but can still grow in mixture, and resistant cells start to dominate at higher dilution rates. We will see
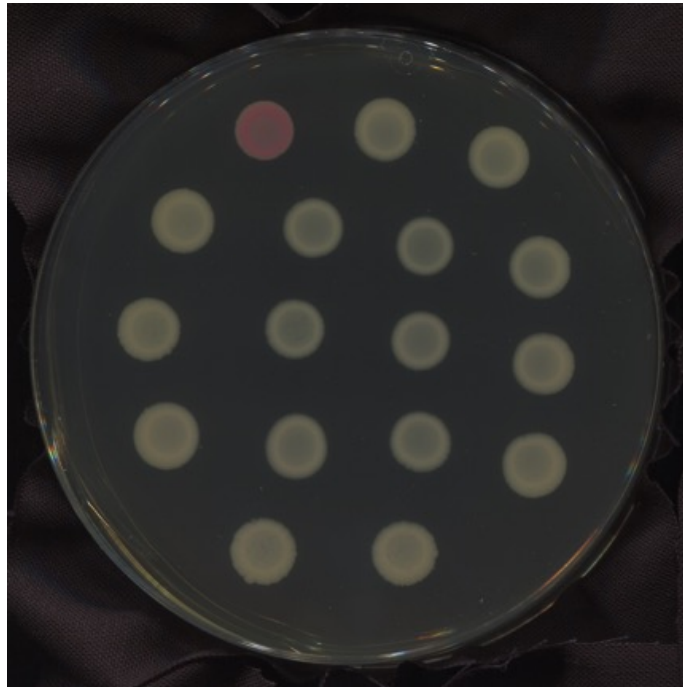
Figure 4.10: Scanner image of one plate without ampicillin. Fraction of resistant cells is 0.1. Dilution rates are 1, 10, 100 and 1000.
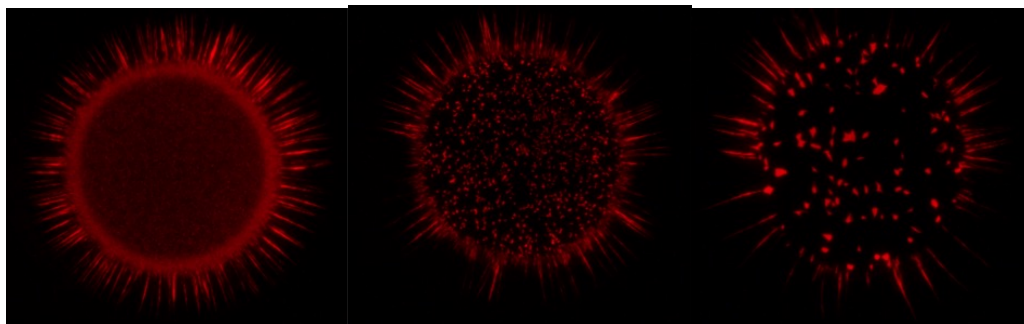
(a) Microscope image of one resistant colony without dilution.

(b) Microscope image of one resistant colony with dilution rate 100.

(c) Microscope image of one resistant colony with dilution rate 1000.

Figure 4.11: Microscope images of one plate without ampicillin.
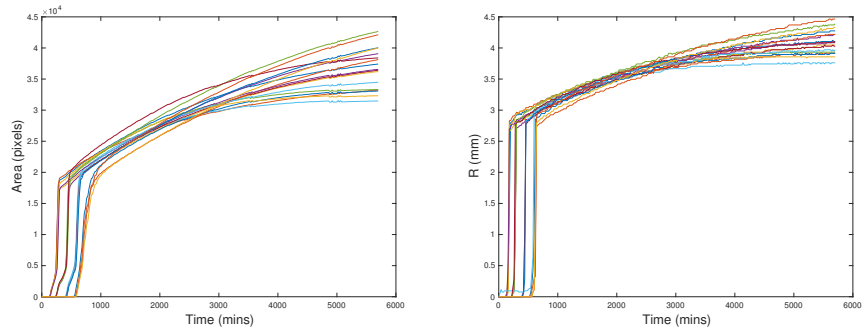
(a) Area of each colony on one plate as a func- (b) Radius of each colony on one plate as a
tion of time.   function of time.

Figure 4.12: ScanLag images of one plate without ampicillin.

interesting patterns in figures 4.13, 4.14, 4.15 and 4.16 at higher dilutions, and it is
difficult for resistant cells to survive at high concentration of antibiotic as well.

4.2.4 Stochastic Lattice Model

While the stepping stone model is a powerful tool for simple populations, it is not
easy to extend the analytical results to two-dimensions or to incorporate complex
cooperative interactions. To investigate the source of the spatial patterns observed
in our experiments, we adapted a simple, lattice-based stochastic model that can be
used to simulate our experiment results [103]. As proof of principle, we simulated
colony growth on a lattice size of 1000*1000 and with a local carrying capacity of
30 at each spatial location. The simulation was started with a mixture population
$N = 10000$ in the center of the lattice. The initial radius can vary according to
different conditions, typically $R_0 = 40$, which is consistent with measured pixels in
our experiment.

During each time step, each island will have the chance to grow and migrate.
First, one randomly choses an individual from a point; the migration rate is then
proportional to the fraction of the cells on the point and the fraction of vacancies on
a randomly selected nearest-neighbor point. The growth probability is proportional
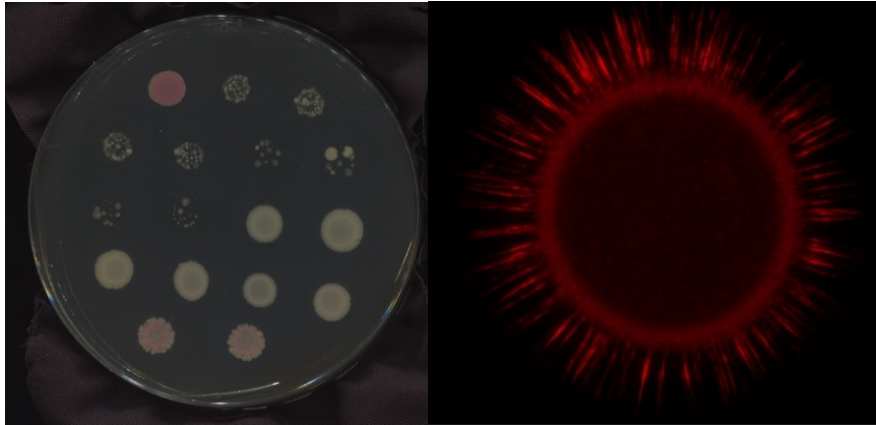
81

(a) Scanner image of one plate.

(b) Microscope image of one resistant colony without dilution.
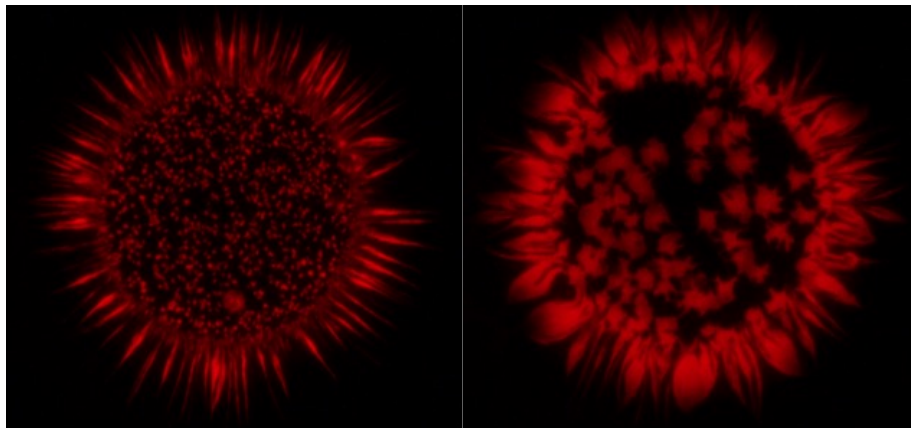
(c) Microscope image of one resistant colony with dilution rate 100.

(d) Microscope image of one resistant colony with dilution rate 1000.

Figure 4.13: Microscope images of one plate with 1 μg/mL ampicillin.
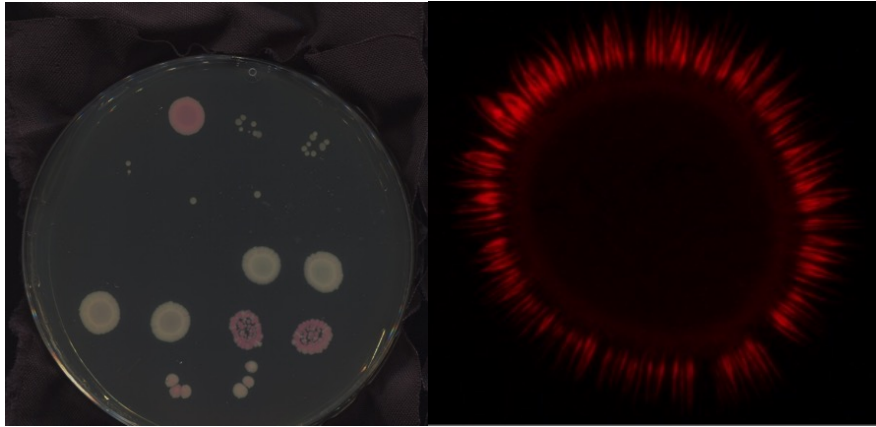
(a) Scanner image of one plate.

(b) Microscope image of one resistant colony without dilution.
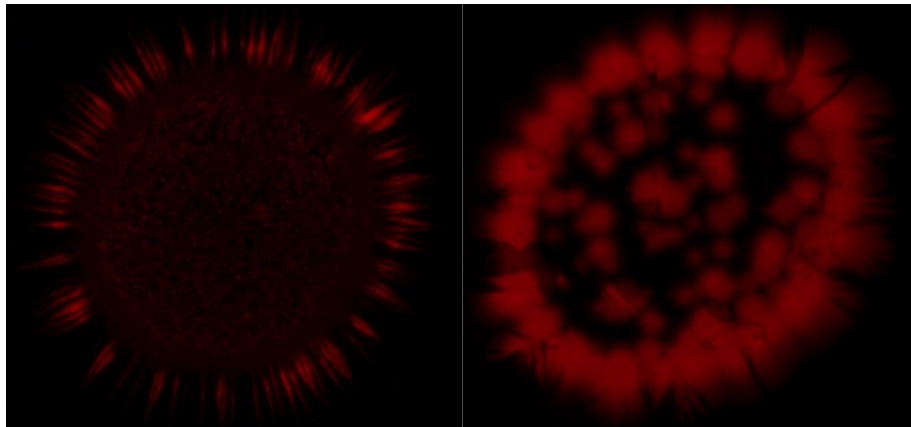
(c) Microscope image of one resistant colony with dilution rate 10.

(d) Microscope image of one resistant colony with dilution rate 100.

Figure 4.14: Microscope images of one plate with 2 μg/mL ampicillin.
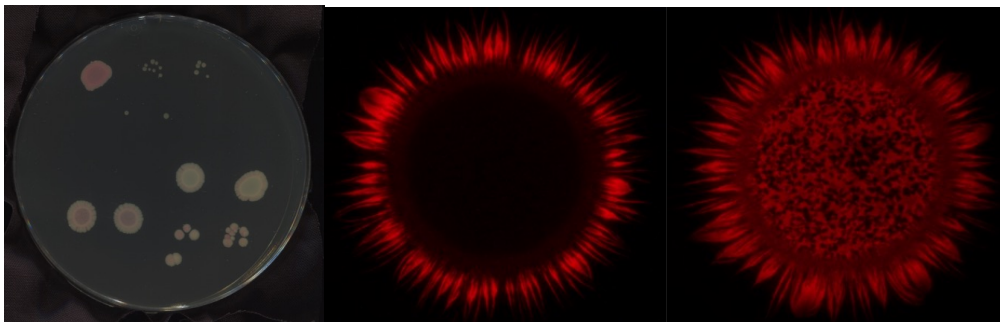
(a) Scanner image of one plate. (b) Microscope image of one resistant colony without dilution. (c) Microscope image of one resistant colony with dilution rate 10.

Figure 4.15: Microscope images of one plate with 3 μg/mL ampicillin.
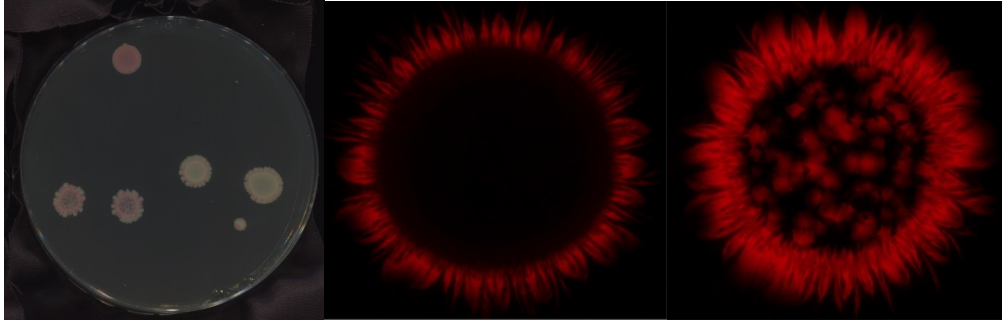
(a) Scanner image of one plate. (b) Microscope image of one resis-(c) Microscope image of one resis-
tant colony without dilution.   tant colony with dilution rate 10.

Figure 4.16: Microscope images of one plate with 4 μg/mL ampicillin.

to the fraction of the cells on the point and fraction of vacancies as well. As shown in figure 4.17, it is straightforward to measure the growth of a colony and observe dynamics for a wide range of conditions.

4.2.4.1 Model captures basic features of stepping stone model but allows for incorporation of complex interactions

To begin investigating our experimental observations, we increased the initial radius by increasing the total volume and keeping cell density constant. I assume population number is proportional to R_0^2. The model exhibits a linear relation between number of sectors and square root of radius (Figure 4.18), similar to what is predicted in the stepping stone model.

Our ongoing work is focused on adapting the lattice model above to incorporate cooperative effects of antibiotic resistance. To do so, we assume that cell death occurs stochastically at a rate r that decreases linearly with the number of resistant cells in the local lattice site. Indeed, this simple model exhibits cooperation and density effects similar to those seen in experiment; for example, in the presence of antibiotic at high concentrations, the sensitive cell population will not survive if the initial population density is sufficiently low (Figure 4.19). Our current work is focused on investigating the impact of cooperation on spatial patterns in both motile and non-
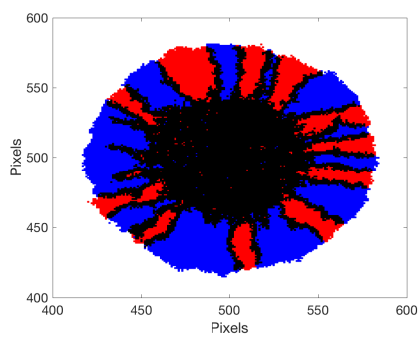
(a) Spatial pattern model of a colony expansion.
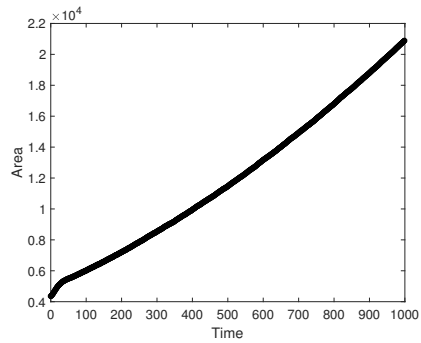
(b) Area as a function of time.
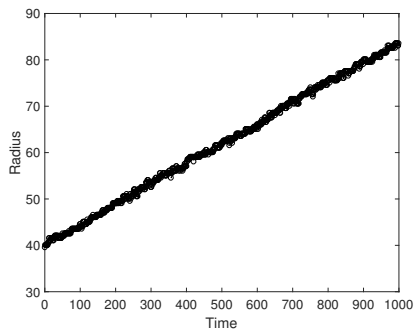
(c) Radius as a function of time.
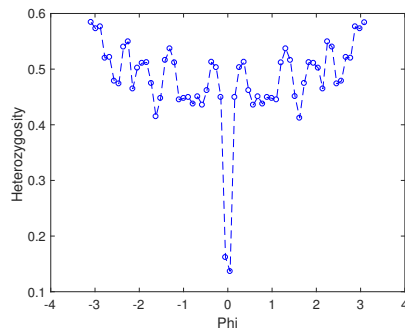
(d) Heterozygosity as a function of polar angle.

Figure 4.17: Images of stochastic modeling without antibiotic. Time=1000, initial fraction of resistant cells is 0.5. Blue and red color represents sensitive and resistant cells respectively, black color means mixture.
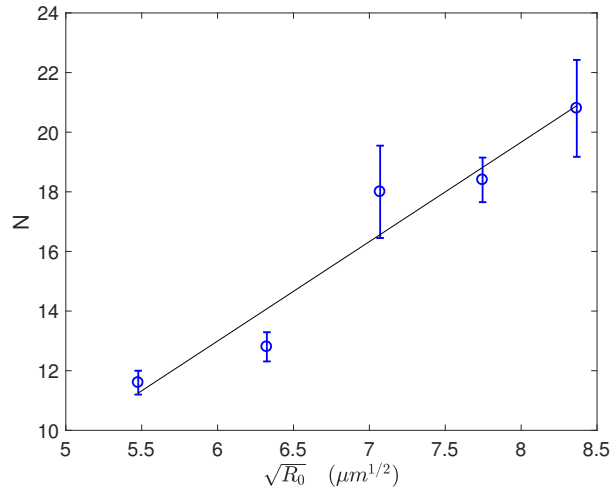
Figure 4.18: Number of sectors as a function of square root of radius. Blue curve is least-squares fitting and initial fraction of resistant cells in mixture is 0.1.

motile cells. While the current simulation mimics many of the features of *E. coli* pattern formation, we expect that a more sophisticated model will be needed for the patterns observed in non-motile cells.

4.3 Conclusion

We have developed a quantitative experimental platform for studying dynamics and steady-state spatial patterns of fluorescently labeled bacterial populations growing on agar plates. The setup involves a commercial document scanner controlled by customized Matlab software, adapted from a similar setup developed in [105], and can be used to track colony size over time. At the final time point, spatial patterns are visualized with high spatial resolution to investigate pattern formation in multicolored communities. We have found that both *E. coli* and *E. faecalis* communities comprised of sensitive and drug-resistant cells exhibit colony growth dynamics and spatial patterns consistent with a simple stepping stone model in the absence of antibiotic. However, the addition of antibiotic leads to considerably more complex behavior, including cooperation between sensitive and resistant cells leading to
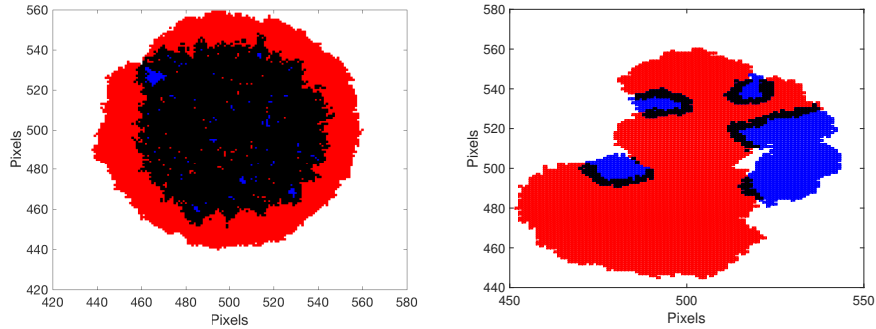
(a) Spatial pattern model of a colony expan-(b) Spatial pattern model of a colony expansion. Initial cell number is 10000. sion. Initial cell number is 100.

Figure 4.19: Images of stochastic modeling with antibiotic. Time=500, killing rate $d = d_0(1\text{-fraction}$ of resistant cells), $d_0 = 0.1$, initial fraction of resistant cells is 0.1. Blue and red color represents sensitive and resistant cells respectively, black color means mixture.
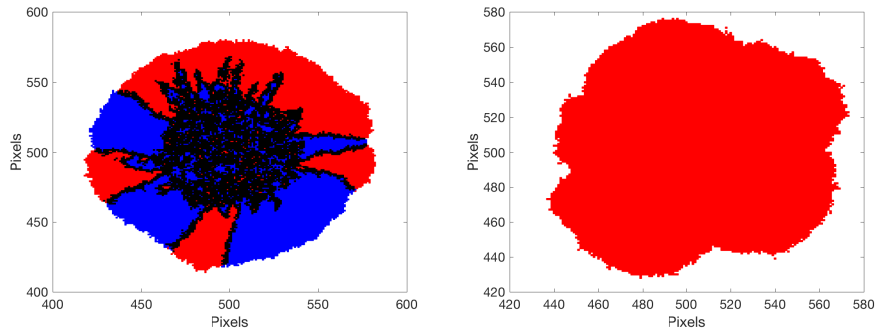
(a) Spatial pattern model of a colony expan-(b) Spatial pattern model of a colony expansion. Initial cell number is 10000 and killingsion. Initial cell number is 100 and killing rate rate $d = 0.02$. $d = 0.2$.

Figure 4.20: Images of stochastic modeling with antibiotic. Time=500, initial fraction of resistant cells is 0.1. Blue and red color represents sensitive and resistant cells respectively, black color means mixture.

density-dependent extinction of the sensitive subpopulation. We also observe striking differences in the patterns formed between the two bacterial species. To investigate these trends, we've developed a simple stochastic model of colony growth that can be easily extended to incorporate complex interactions and competition between cells. Our preliminary results indicate that a local spatial coupling between the death rate of sensitive cells and the local density of resistant cells captures some qualitative features of our experiments. As a whole, our set-up allows for the quantitative study of spatial patterns and provides a framework for ongoing studies on the impact of cooperative antibiotic resistance on spatial pattern formation in multiple bacterial species.

CHAPTER V

Materials and Methods

5.1 Bacterial strains and media

The bacteria used in my study are *Enterococcus faecalis* V583, OG1RF and *Escherichia coli* MG1655. The vancomycin resistance strain V583 was isolated from blood culture of patients in 1987 [108]. OG1RF was derived from human oral isolate OG1 [109]. MG1655 is a commonly used wild-type *E. coli* and was derived from original K-12 isolate [110].

In order to label strains with different fluorescent colors, ATUM ProteinPaintbox was purchased and FPB-54-441 was used for *E. coli* fresno red fluorescent protein (RFP), which has Isopropyl β-D-1-thiogalactopyranoside (IPTG) inducible promoter with kanamycin marker of 25 μg/mL resistance. Blue fluorescent protein (BFP) was originally from plasmid pBAD-mTagBFP2 [111] and was Gibson assembled onto the same backbone as fresno RFP. Plasmid used to construct resistant *E. coli* was pFPV-mCherry, which can express β-lactamase enzyme and mCherry fluorescent protein [112]. These plasmids were then transformed into *E. coli* MG1655 using standard transformation protocols.

The plasmid vector used for *E. faecalis* was pBSU101 [113], which has a 120 μg/mL spectinomycin resistance marker and constitutively expresses GFP. FPB-31-441 rudolph RFP or BFP color region was inserted into pBSU101 to replace GFP

Bacterial Strains and Plasmids	Characteristics	Chapter
E. faecalis V583	Wild-type	Chapter III
E. faecalis OG1RF	Wild-type	Chapter III
E. coli MG1655 + IPTG-Fresno RFP + pFPV-mCherry	IPTG inducible, 25 μg/mL kanamycin resistance, Fresno RFP and β-lactamase enzyme	Chapter IV
E. coli MG1655 + IPTG-BFP	IPTG inducible, 25 μg/mL kanamycin resistance and BFP	Chapter IV
E. faecalis OG1RF + pBSU101-Rudolph RFP-β-lactamase	120 μg/mL spectinomycin resistance, Rudolph RFP and β-lactamase enzyme	Chapter IV
E. faecalis OG1RF + pBSU101-BFP	120 μg/mL spectinomycin resistance and BFP	Chapter IV

Table 5.1: A list of bacterial strains and plasmids used in this project.

and provide multiple colors. To make resistant *E. faecalis*, the β-lactamase gene and the corresponding promoter was amplified by PCR from the chromosome of *E. faecalis* HH22 [114] and then Gibson assembled onto pBSU101. These plasmids were finally transformed into *E. faecalis* OG1RF.

E. faecalis bacteria was inoculated from single colony grown on brain heart infusion (BHI) medium with 1.5% (w/v) bacteriological agar added. *E. coli* bacteria was inoculated from lennox lysogeny broth (LB) agar. All media were prepared using millipore water and were sterilized by autoclaving at 121°C for 15 minutes. *E. faecalis* strains were grown overnight in BHI or tryptic soy broth (TSB) medium at 37°C without shaking. *E. coli* strains were grown overnight in LB medium at 30°C with continuous shaking at 200 rpm.

For long-term storage, bacterial stocks were made by mixing overnight culture with sterilized 30% glycerol solution. All antibiotics used in my study in table 5.1 were sterilized by passing 0.22 μm filter, aliquoted and kept at -20 or -80°C for no more than 3-6 months.

All chemicals and media were purchased from Sigma-Aldrich or Fisher Scientific unless stated otherwise.

Antibiotics	Description	Abbreviation
Ampicillin	Interfere with bacterial cell wall synthesis	AMP
Vancomycin	Cell wall synthesis inhibitor	VAN
Ceftriaxone	Cell wall synthesis inhibitor	CEF
Tazobactam	Cell wall synthesis inhibitor	TAZ
Fosfomycin	Cell wall synthesis inhibitor	FOS
Oxacillin	Cell wall synthesis inhibitor	OXA
Chlorhexidine	Disrupt cell membrane	CHL
Gentamicin	Inhibit 30s subunit	GEN
Tetracycline	Inhibit 30s subunit	TET
Tigecycline	Inhibit 30s subunit	TIG
Doxycycline	Inhibit 30s subunit	DOX
Spectinomycin	Inhibit 30s subunit	SPEC
Kanamycin	Inhibit 30s subunit	KAN
Erythromycin	Inhibit 50s subunit	ERY
Linezolid	Inhibit 50s subunit	LIN
Ciprofloxacin	DNA synthesis inhibitor	CIP
Norfloxacin	DNA synthesis inhibitor	NOR
Nitrofurantoin	Cell wall, protein, DNA and RNA synthesis inhibitor	NIT
Rifampin	RNA synthesis inhibitor	RIF
Trimethoprim	Folic Acid synthesis inhibitor	TRI

Table 5.2: A list of antibiotics used in this project.

5.2 Growth curves of *Enterococcus faecalis*

E. faecalis V583 overnight culture was diluted 100 times into fresh BHI medium, and then 200 μL diluted culture was added to each well of a 96-well plate. Different concentrations of antibiotics were added when measuring killing rates or minimum inhibitory concentrations (MICs). EnSpire Multimode Plate Reader was used to incubate and measure optical density at a wavelength of 600 nm every 15 minutes for 24 hours at 30°C. BHI medium was used as a blank. Each condition under test would have a few replicates.

5.3 Microtiter plate biofilm assay

Overnight cultures of *E. faecalis* V583 were diluted 1:100 into fresh BHI medium. 100 μL of dilution culture with different concentrations of antibiotics or chemicals was added to each well of a flat-bottomed polystyrene microtiter 96-well plate (Greiner

Bio-One Cellstar). For each treatment we had 6-12 replicates. The plate was incubated at 37°C without shaking for 24 hours.

After incubation, we dumped out liquid cultures by turning over the plate, shaking and patting on paper towels. Wells were then gently washed washed and shaken with fresh phosphate buffered saline (PBS). To fix biofilm on the plate, 125 μL 96% ethanol was added into each well for 20 minutes. Ethanol was then dumped and we let the plate dry at room temperature for half an hour. 125 μL 0.5% crystal violet [115] [116] was then added to stain the whole biofilm mass. After 30 minutes, we washed plate by pipetting PBS twice, and then rinsed it twice into a tub of PBS and dumped out liquid. The plate was turned upside down and dried for 1 hour. Finally, 125 μL 30% acetic acid was added to each well in order to dissolve biofilm. Solutions were transferred to a new 96-well plate and absorbance readings at 590 nm were taken using Enspire multimodal plate reader.

5.4 ATP detection assay

Biofilms were grown with different concentrations of antibiotics or chemicals in a 96-well plate for 24 hours. We then washed the plate twice with nuclease-free water and dumped out liquid. 10 μL nuclease-free water was added to each well and biofilms were scraped down by using inoculation loops or pipette tips. Solutions were transferred to a new 96-well white polystyrene plate (Thermo Scientific Nunc F96 MicroWell) and 90 μL ATP standard assay solution from ATP Determination kit (Molecular Probes) was added to each sample. Luminescence was measured by plate reader.

5.5 Confocal laser scanning microscopy

200 μL bacterial cultures wth ampicillin or DNase I were grown in a 16-well chambered coverglass vessels. Four replicates for each treatment were made. After incubating for 24 hours, liquid was removed and plate was washed twice with filtered millipore water and then stained using LIVE/DEAD BacLight Bacterial Viability kit (Molecular Probes) for 20 minutes. We then dumped out liquid again, removed upper structure of the vessel and attached a coverglass on top of it.

Zesis LSM700 confocal laser scanning microscope was used to examine biofilm samples. For each well, four image stacks were taken at similar locations on the cover slip. Thickness of a biofilm is typically about 20-30 μm and the spacing between slices is 1 μm. To analyze images, we split them into red and green channels, adjusted brightness/contrast and set threshold individually using automated thresholding algorithms in ImageJ. We then performed watershed algorithm to segment cells and finally measured number of live or dead cells for each slice within biofilms.

5.6 DNA techniques

5.6.1 Extracellular DNA/RNA extraction

Biofilms were grown with ampicillin 0, 0.1 and 0.2 μg/mL in 6-well polystyrene plates with a total volume of 5 mL for each well. Each treatment had three replicates. After 24 hours, we dumped out liquid and washed the plate twice with PBS. 1 mL 1X Tris-EDTA (TE, 10mM Tris-Cl, 1 mM EDTA, pH=8.0) buffer was added into each well and we then scraped down biofilms from bottom of plates.

After harvesting biofilms, cells were centrifuged down and supernatant was purified by using only binding and washing steps in QIAprep Spin Miniprep kit according to the manufacturer's instruction. 5 volumes of PB buffer was added to 1 volume

of supernatant and mixed. 800 μL of solution was transferred to a spin column and centrifuged at 13000 rpm for 1 minute. 0.5 mL PB buffer was added to wash the spin column and centrifuged for 1 minute. 0.75 mL PE buffer was added to spin column and centrifuged again for 1 minute. The flow-through was discarded and residual was removed by centrifuging spin column for an additional 1 minute. Transferred spin column in a new 1.5 mL microcentrifuge tube and 30 μL EB buffer was added to the center of the spin column. Let it stand for 1 minute and then centrifuged for 1 minute to elute DNA. DNase I or RNase was added to the same treatment samples as controls.

5.6.2 Agarose gel electrophoresis

We first rinsed gel tray and related tools with nuclease-free water and then made 1% agarose gel with 1X Tris-acetate-EDTA (TAE, pH=8.4) buffer according to size of DNA fragments. Appropriate volume of SYBR safe was added into agarose gel. We then filled chamber with 1X TAE buffer and samples were loaded according to the well size. The gel was run at 120V for 40 mins. DNA or RNA fragments were virtualized under UV light from UV transilluminator. To analyze images, ImageJ software was used to subtract background and perform intensity analysis for different lanes. The same size of regions were selected for different lanes and a profile plot of each lane was drawn. A straight line across the base of peak was drawn to enclose the peak, and the wand tool was used to select each peak and measure percentage of relative densities.

5.6.3 Transformation by electroporation

150 mL culture of *E. faecalis* was grown overnight in BHI medium. 30 mL of liquid culture was aliquoted into chilled 50 mL centrifuge tube. We harvested cells

by centrifuging at 5000g for 15 minutes, resuspended pellet in 30 mL chilled 10% glycerol, and centrifuged again. We then repeated wash step with 15 mL chilled glycerol and again with 6 mL glycerol. The pellet was resuspended in 600 μL chilled glycerol and transferred to a chilled 1.5 mL microcentrifuge tube. After centrifuging for 15 minutes, resuspended pellet in 200 μL glycerol.

1.5 mL overnight culture of *E. coli* was diluted in 150 mL fresh super optimal broth (SOB). The culture was grown with shaking until optical density reached 0.4-0.5. Cells were harvested by centrifuging 30 mL culture at 6500g for 7 minutes. We washed pellet with 30 mL chilled nuclease-free water and centrifuged, resuspended pellet in 1 mL nuclease-free water, and transferred suspension to a new microcentrifuge tube. After centrifuging at 17000g for 1 minute, we resuspended the pellet in 200 μL nuclease-free water.

Plasmids were extracted and purified by using QIAprep Spin Miniprep kit in 5.6.1. Appropriate DNA solutions were mixed with electrocompetent cells in a chilled eporator cuvette. The cuvette was then charged and fired at certain voltage. The mixture was added in 1 mL fresh media and grown for 3 hours. After outgrowth, 100 μL culture was dispensed on a selective plate and grown overnight.

5.7 RNA sequencing

We prepared biofilm samples following the same protocols in 5.6.1 with ampicillin 0, 0.125 and 0.25 μg/mL. RNA extraction was performed by using a Qiagen RNeasy mini kit in combination with RNAprotect Bacteria Reagent and RNase-Free DNase Set. TE buffer (30 mM Tris-Cl, 1 mM EDTA, pH=8.0) containing 50 mg/mL lysozyme was prepared.

2 volumes of bacteria reagent were added to 1 volume of biofilm culture and

mixed by vortexing for 5 seconds. After incubating for 5 minutes, the culture was centrifuged at 5000g for 10 minutes and then supernatant was discarded. 10 μL Qiagen proteinase K and 200 μL TE buffer was added to resuspend the pellet. After vortexing for 10 seconds, solution was incubated for 20 minutes and vortexed for 10 seconds every 2 minutes. 700 μL RLT buffer was added and the tube was centrifuged for 2 minutes at a maximum speed. 500 μL 96% ethanol was added and mixed by pipetting. 700 μL lysate was then transferred to a spin column and centrifuged at 13000 rpm for 15 seconds. The flow-through was discarded and 350 μL RW1 buffer was added to spin column. The spin column was centrifuged again for 15 seconds. 10 μL DNase I and 70 μL RDD buffer was then added and incubated for 15 minutes. 350 μL RW1 buffer was added to spin column and incubated for 5 minutes, and then centrifuged for 15 seconds. The spin column was transferred to a new 2 mL collection tube. 500 μL RPE buffer was added and centrifuged to wash the spin column membrane. Washed it again by adding 500 μL RPE buffer and centrifuging or an additional 2 minutes. Finally, the spin column was transferred in a new 1.5 mL collection tube. 30 μL RNase-free water was added and centrifuged for 1 minute to elute RNA.

According to manufacturer's instruction, total RNA was isolated with high quality. Ribosomal RNA removal, RNA-seq libraries preparation and measurements were performed by University of Michigan DNA sequencing core by using HiSeq 50 cycle single-read stranded RNA method.

After checking RNA quality, short-sequence reads were annotated onto NCBI reference by using Bowtie 2 [117] and alignments were sorted by using SAMtools [118]. Differential gene expression analysis was performed by using Cuffdiff [119] and CummeRbund [120], and then BioVenn [121] was used for comparisons between different

treatment cases. Differentially express genes were obtained based on criteria that false discovery rate (FDR) value $<= 0.05$ and $|\log(\text{fold change})|$ (FC) $>= 0.5$. Significant proteins were used to determine the Clusters of Orthologous Groups (COG) of proteins.

5.8 Scanner Tracking of Microbial Colonies

We used the previously described "ScanLag" technique to record growth dynamics of cells on agar plates at high temporal and spatial resolution [107]. This technique could be customized for use in my study in order to automatically monitor pattern formation and help to understand growth and cooperation process when working with two cell types.

A commercial document scanner (Epson Perfection V370 Flatbed scanner) was set up and controlled by a laptop using scanning manager application files can be downloaded from JoVE [105] and installed on laptop. Petri dishes with appropriate medium and different concentrations of antibiotics were prepared and 1.0% (w/v) bacteriological agar was added. Cultures of interested bacteria were grown overnight in appropriate medium with relative antibiotics and then diluted in fresh medium until optical density reached 0.1. Cells were centrifuged down and resuspended in nuclease-free water. Different ratios of cell compositions and densities were created based on based on experimental requirements. 1-15 μL droplets of culture were plated on agar plates. The plates were covered with black cloth to absorb moisture and placed on the scanner (at most 6 plates). The laptop was able to control the scanner to automatically take images every 15-20 minutes over 2-3 days.

Finally, we developed customized Matlab software to analyze these images and measure characteristics of colonies. By labeling and tracking sizes of colonies, the

appearance time of each colony could be measured to determine antibiotic stresses. Radius and area of each colony were also recorded in order to calculate growth rates of bacteria.

The plates were also imaged at the final time step by using Olympus fluorescence microscope with monochrome camera. These images were processed and analyzed to study dynamics and genetic demixing phenomenon between two types of cells.

BIBLIOGRAPHY

BIBLIOGRAPHY

[1] A. Pikovsky, M. Rosenblum, and J. Kurths. *Synchronization: A Universal Concept in Nonlinear Sciences*. Cambridge, 2001.

[2] John H. Miller and Scott E. Page. *Complex Adaptive Systems: An Introduction to Computational Models of Social Life*. Princeton Studies in Complexity. Princeton University Press, 2007.

[3] Claudio Castellano, Santo Fortunato, and Vittorio Loreto. Statistical physics of social dynamics. *Rev. Mod. Phys.*, 81, 2009.

[4] Frank Schweitzer. *Brownian Agents and Active Particles: Collective Dynamics in the Natural and Social Sciences*. Synergetics. Springer, 2009.

[5] Yaneer Bar-yam. *Dynamics Of Complex Systems*. Studies in Nonlinearity. Westview Press, 1997.

[6] J R Lawrence, D R Korber, B D Hoyle, J W Costerton, and D E Caldwell. Optical sectioning of microbial biofilms. *Journal of bacteriology*, 173(20):6558–6567, Oct. 1991.

[7] Jintao Liu, Arthur Prindle, Jacqueline Humphries, Marçal Gabalda-Sagarra, Munehiro Asally, Dong-yeon D Lee, San Ly, Jordi Garcia-Ojalvo, and Gürol M Süel. Metabolic codependence gives rise to collective oscillations within biofilms. *Nature*, 523(7562):550, 2015.

[8] Arthur Prindle, Jintao Liu, Munehiro Asally, San Ly, Jordi Garcia-Ojalvo, and Gürol M Süel. Ion channels enable electrical communication within bacterial communities. *Nature*, 527(7576):59, 2015.

[9] Jintao Liu, Rosa Martinez-Corral, Arthur Prindle, D Lee Dong-yeon, Joseph Larkin, Marçal Gabalda-Sagarra, Jordi Garcia-Ojalvo, and Gürol M Süel. Coupling between distant biofilms and emergence of nutrient time-sharing. *Science*, 356(6338):638–642, 2017.

[10] Jacqueline Humphries, Liyang Xiong, Jintao Liu, Arthur Prindle, Fang Yuan, Heidi A Arjes, Lev Tsimring, and Gürol M Süel. Species-independent attraction to biofilms through electrical signaling. *Cell*, 168(1):200–209, 2017.

[11] Nicholas Chia, Carl R Woese, and Nigel Goldenfeld. A collective mechanism for phase variation in biofilms. *Proceedings of the National Academy of Sciences*, 105(38):14597–14602, 2008.

[12] Philip S Stewart and Michael J Franklin. Physiological heterogeneity in biofilms. *Nature reviews. Microbiology*, 6(3):199, 2008.

[13] Nuno M Oliveira, Esteban Martinez-Garcia, Joao Xavier, William M Durham, Roberto Kolter, Wook Kim, and Kevin R Foster. Biofilm formation as a response to ecological competition. *PLoS Biol*, 13(7):e1002191, 2015.

[14] Nicole M Vega and Jeff Gore. Collective antibiotic resistance: mechanisms and implications. *Current opinion in microbiology*, 21:28–34, 2014.

[15] Hannah R Meredith, Jaydeep K Srimani, Anna J Lee, Allison J Lopatkin, and Lingchong You. Collective antibiotic tolerance: Mechanisms, dynamics, and intervention. *Nature chemical biology*, 11(3):182, 2015.

[16] Thien-Fah C Mah and George A O'Toole. Mechanisms of biofilm resistance to antimicrobial agents. *Trends in microbiology*, 9(1):34–39, 2001.

[17] Carey D. Nadell, Joao B. Xavier, and Kevin R. Foster. The sociobiology of biofilms. *FEMS Microbiol Rev*, 33:206–224, 2009.

[18] Jeffrey B Kaplan. Antibiotic-induced biofilm formation. *Int J Artif Organs*, 34(9):737–751, 2011.

[19] Don B Clewell, Michael S Gilmore, Yasuyoshi Ike, and Nathan Shankar. *Enterococci: from commensals to leading causes of drug resistant infection*. Boston: Massachusetts Eye and Ear Infirmary, 2014.

[20] Rodney M Donlan. Biofilms and device-associated infections. *Emerging infectious diseases*, 7(2):277, 2001.

[21] Y. Kuramoto. *Chemical Oscillations, Waves, and Turbulence*. Springer-Verlag, 1984.

[22] Juan A. Acebron, L. L. Bonilla, Conrad J Perez Vicente, Felix Ritort, and Renato Spigler. The kuramoto model: A simple paradigm for synchronization phenomena. *Reviews of Modern Physics*, 77:137–185, 2005.

[23] Steven H. Strogatz. *Sync: How Order Emerges From Chaos In the Universe, Nature, and Daily Life*. Hyperion, 2004.

[24] Steven H. Strogatz. From kuramoto to crawford: exploring the onset of synchronization in populations of coupled oscillators. *Physica D*, 143:1–20, 2000.

[25] A. T. Winfree. Biological rhythms and the behavior of populations of coupled oscillators. *Journal of Theoretical Biology*, 16:15–42, 1967.

[26] F. Grenier, I. Timofeev, and M. Steriade. Neocortical very fast oscillations (ripples, 80-200 hz) during seizures: intracellular correlates. *Journal of Neurophysiology*, 89:841–852, 2003.

[27] Jonathon Shlens, Greg D. Field, Jeffrey L. Gauthier, Martin Greschner, Alexander Sher, Alan M. Litke, and E. J. Chichilnisky. The structure of large-scale synchronized firing in primate retina. *Journal of Neuroscience*, 29(15):5022–5031, 2009.

[28] Qiong Yang, Bernardo F Pando, Guogang Dong, Susan S Golden, and Alexander van Oudenaarden. Circadian gating of the cell cycle revealed in single cyanobacterial cells. *Science*, 327(5972):1522–6, Mar 2010.

[29] J. S. van Zon, D. K. Lubensky, P. R. H. Altena, and P. Rein ten Wolde. An allosteric model of circadian kaic phosphorylation. *Proceedings of the National Academy of Sciences*, 104(18):7420–7425, 2007.

[30] D. Zwicker, D. K. Lubensky, and P. Rein ten Wolde. Robust circadian clocks from coupled protein-modification and transcription–translation cycles. *Proceedings of the National Academy of Sciences*, 107(52):22540–22545, 2010.

[31] Qiong Yang and James E Ferrell, Jr. The cdk1-apc/c cell cycle oscillator circuit functions as a time-delayed, ultrasensitive switch. *Nat Cell Biol*, 15(5):519–25, May 2013.

[32] Steven M Reppert and David R Weaver. Coordination of circadian timing in mammals. *Nature*, 418(6901):935–41, Aug 2002.

[33] Jonathan Bieler, Rosamaria Cannavo, Kyle Gustafson, Cedric Gobet, David Gatfield, and Felix Naef. Robust synchronization of coupled circadian and cell cycle oscillators in single mammalian cells. *Mol Syst Biol*, 10(7):739, 2014.

[34] Igor Segota, Laurent Boulet, David Franck, and Carl Franck. Spontaneous emergence of large scale cell cycle synchronization in amoeba colonies. *Physical Biology*, 11(3):036001, 2014.

[35] T. Danino, O. Mondragon-Palomino, Lev S. Tsimring, and Jeff Hasty. A synchronized quorum of genetic clocks. *Nature*, 463:326–330, 2010.

[36] Arthur Prindle, Jangir Selimkhanov, Howard Li, Ivan Razinkov, Lev S. Tsimring, and Jeff Hasty. Rapid and tunable post-translational coupling of genetic circuits. *Nature*, 508:387–391, 2014.

[37] A. Koseska, E. Ullner, E. Volkov, J. Kurths, and J. Garcia-Ojalvo. Cooperative differentiation through clustering in multicellular populations. *Journal of Theoretical Biology*, 263:189–202, 2010.

[38] Jordi Garcia-Ojalvo, Michael B. Elowitz, and Steven H. Strogatz. Modeling a synthetic multicellular clock: Repressilators coupled by quorum sensing. *Proceedings of the National Academy of Sciences*, 101(30):10955–10960, 2004.

[39] Yu. P. Emelianovaa, A. P. Kuznetsovb, I. R. Sataevb, and L. V. Turukinab. Synchronization and multi-frequency oscillations in the low-dimensional chain of the self-oscillators. *Physica D*, 244:36–49, 2013.

[40] T. Prager, B. Naundorf, and L. Schimansky-Geier. Coupled three-state oscillators. *Physica*, 325A:176, 2003.

[41] K. Wood, C. Van den Broeck, R. Kawai, and K. Lindenberg. Universality of synchrony: Critical behavior in a discrete model of stochastic phase-coupled oscillators. *Physical Review Letters*, 96:145701, 2006.

[42] K. Wood, C. van den Broeck, R. Kawai, and K. Lindenberg. Critical behavior and synchronization of discrete stochastic phase-coupled oscillators. *Physical Review E*, 74:031113, 2006.

[43] K. Wood, C. van den Broeck, R. Kawai, and K. Lindenberg. Effects of disorder on synchronization of discrete phase-coupled oscillators. *Physical Review E*, 75:041107, 2007.

[44] K. Wood, C. van den Broeck, R. Kawai, and K. Lindenberg. Continuous and discontinuous phase transitions and partial synchronization in stochastic three-state oscillators. *Physical Review E*, 76:041132, 2007.

[45] Simone Bianco, Elvis Geneston, Paolo Grigolini, and Massimiliano Ignaccolo. Renewal aging as emerging property of phase synchronization. *Physica A*, 387:1387–1392, 2008.

[46] Xiaohua Cui, Robert J. Rovetti, Ling Yang, Alan Garfinkel, James N. Weiss, and Zhilin Qu. Period-doubling bifurcation in an array of coupled stochastically excitable elements subjected to global periodic forcing. *Physical Review Letters*, 103:044102, 2009.

[47] Fernando Rozenblit and Mauro Copelli. Collective oscillations of excitable elements: order parameters, bistability and the role of stochasticity. *Journal of Statistical Mechanics: Theory and Experiment*, 2011:P01012, 2011.

[48] Vladimir R V Assis, Mauro Copelli, and Ronald Dickman. An infinite-period phase transition versus nucleation in a stochastic model of collective oscillations. *Journal of Statistical Mechanics: Theory and Experiment*, 2011:P09023, 2011.

[49] Vladimir R V Assis and Mauro Copelli. Collective behavior of coupled nonuniform stochastic oscillators. *Physica A*, 2012:1900–1906, 2012.

[50] Bastien Fernandez and Lev S. Tsimring. Athermal dynamics of strongly coupled stochastic three-state oscillators. *Physical Review Letters*, 100:165705, 2008.

[51] D. Escaff, U. Harbola, and K. Lindenberg. Synchronization of globally coupled two-state stochastic oscillators with a state-dependent refractory period. *Physical Review E*, 86:041144, 2012.

[52] D. Escaff, Italo'Ivo Lima Dias Pinto, and K. Lindenberg. Arrays of stochastic oscillators: Nonlocal coupling, clustering, and wave formation. *Physical Review E*, 90:052111, 2014.

[53] Italo'Ivo Lima Dias Pinto, Daniel Escaff, Upendra Harbola, Alexandre Rosas, and Katja Lindenberg. Globally coupled stochastic two-state oscillators: Fluctuations due to finite numbers. *Physical Review E*, 89(5):052143, 2014.

[54] Raymond Cho, Michael Campbell, Elizabeth Winzeler, Lars Steinmetz, Andrew Conway, LIsa Wodicka, Tyra Wolfsberg, Andrei Gabrielian, David Landsman, David Lockhart, and Ronald Davis. A genome-wide transcriptional analysis of the mitotic cell cycle. *Molecular Cell*, 2:65–73, 1998.

[55] Paul Spellman, Gavin Sherlock, Michael Zhang, Vishwanath Iyer, Kirk Anders, Michael Eisen, Patrick Brown, David Botstein, and David Futcher. Comprehensive identification of cell cycle-regulated genes of the yeast saccharomyces cerevisiae by microarray hybridization. *Molecular Biology of the Cell*, 9:3273–3297, 1998.

[56] Alan Sachs. Cell cycle-dependent translation initiation: Ires elements prevail. *Cell*, 101:243–245, 2000.

[57] Bjorn Grunenfelder, Gabriele Rummel, Jiri Vohradsky, Daniel Roder, Hanno Langen, and Urs Jenal. Proteomic analysis of the bacterial cell cycle. *Proceedings of the National Academy of Sciences*, 98:4681–4686, 2000.

[58] Shobha Vasudevan, Yingchun Tong, and Joan Steitz. Switching from repression to activation: Micrornas can up-regulate translation. *Science*, 318:1931–1934, 2007.

[59] Birky CW Jr. The partitioning of cytoplasmic organelles at cell division. *Int Rev Cytol Suppl*, 15:49–89, 1983.

[60] Dann Huh and Johan Paulsson. Random partitioning of molecules at cell division. *Proceedings of the National Academy of Sciences*, 108:15004–15009, 2011.

[61] Y. .A Kuznetsov. *Elements of applied bifurcation theory*, volume v. 112 of *Applied mathematical sciences*. Springer, 3rd ed edition, 2004.

[62] D. Gillespie. Exact stochastic simulation of coupled chemical reactions. *Journal of Physical Chemistry*, 81:2340, 1977.

[63] M. Girvan, D. S. Callaway, M. E. J. Newman, and S. H. Strogatz. Simple model of epidemics with pathogen mutation. *Physical Review E*, 65:031915, 2002.

[64] Rodney M Donlan. Biofilms: microbial life on surfaces. *Emerg Infect Dis*, 8(9), 2002.

[65] Sara Mitri, João B Xavier, and Kevin R Foster. Social evolution in multispecies biofilms. *Proceedings of the National Academy of Sciences*, 108(Supplement 2):10839–10846, 2011.

[66] Lucas R Hoffman, David A D'argenio, Michael J MacCoss, Zhaoying Zhang, et al. Aminoglycoside antibiotics induce bacterial biofilm formation. *Nature*, 436(7054):1171, 2005.

[67] Dan I Andersson and Diarmaid Hughes. Microbiological effects of sublethal levels of antibiotics. *Nature reviews. Microbiology*, 12(7):465, 2014.

[68] Jamal A Mohamed and David B Huang. Biofilm formation by enterococci. *Journal of medical microbiology*, 56(12):1581–1588, 2007.

[69] Lynn E Hancock and Marta Perego. The enterococcus faecalis fsr two-component system controls biofilm development through production of gelatinase. *Journal of bacteriology*, 186(17):5629–5639, 2004.

[70] Vinai Chittezham Thomas, Lance R Thurlow, Dan Boyle, and Lynn E Hancock. Regulation of autolysis-dependent extracellular dna release by enterococcus faecalis extracellular proteases influences biofilm development. *Journal of bacteriology*, 190(16):5690–5698, 2008.

[71] Vinai Chittezham Thomas, Yasuaki Hiromasa, Nathan Harms, Lance Thurlow, John Tomich, and Lynn E Hancock. A fratricidal mechanism is responsible for edna release and contributes to biofilm development of enterococcus faecalis. *Molecular microbiology*, 72(4):1022–1036, 2009.

[72] Pascale S Guiton, Chia S Hung, Kimberly A Kline, Robyn Roth, Andrew L Kau, Ericka Hayes, John Heuser, Karen W Dodson, Michael G Caparon, and Scott J Hultgren. Contribution of autolysin and sortase a during enterococcus faecalis dna-dependent biofilm development. *Infection and immunity*, 77(9):3626–3638, 2009.

[73] Vijayalakshmi S Iyer and Lynn E Hancock. Deletion of $\sigma 54$ (rpon) alters the rate of autolysis and biofilm formation in enterococcus faecalis. *Journal of bacteriology*, 194(2):368–375, 2012.

[74] NS Jakubovics, RC Shields, Nithyalakshmy Rajarajan, and JG Burgess. Life after death: the critical role of extracellular dna in microbial biofilms. *Letters in applied microbiology*, 57(6):467–475, 2013.

[75] Theerthankar Das, Shama Sehar, and Mike Manefield. The roles of extracellular dna in the structural integrity of extracellular polymeric substance and bacterial biofilm development. *Environmental microbiology reports*, 5(6):778–786, 2013.

[76] Mira Okshevsky and Rikke Louise Meyer. The role of extracellular dna in the establishment, maintenance and perpetuation of bacterial biofilms. *Critical reviews in microbiology*, 41(3):341–352, 2015.

[77] Jeffrey B Kaplan, Era A Izano, Prerna Gopal, Michael T Karwacki, Sangho Kim, Jeffrey L Bose, Kenneth W Bayles, and Alexander R Horswill. Low levels of β-lactam antibiotics induce extracellular dna release and biofilm formation in staphylococcus aureus. *MBio*, 3(4):e00198–12, 2012.

[78] Amparo M Gallardo-Moreno, Henny C van der Mei, Henk J Busscher, and Ciro Pérez-Giraldo. The influence of subinhibitory concentrations of ampicillin and vancomycin on physico-chemical surface characteristics of enterococcus faecalis 1131. *Colloids and Surfaces B: Biointerfaces*, 24(3):285–295, 2002.

[79] Amparo M Gallardo-Moreno, Henny C van der Mei, Henk J Busscher, M Luisa González-Martin, José M Bruque, and Ciro Pérez-Giraldo. Adhesion of enterococcus faecalis 1131 grown under subinhibitory concentrations of ampicillin and vancomycin to a hydrophilic and a hydrophobic substratum. *FEMS microbiology letters*, 203(1):75–79, 2001.

[80] Juan Ramón Maestre, Lorenzo Aguilar, María Mateo, María-José Giménez, María-Luisa Méndez, Luis Alou, Juan-José Granizo, and José Prieto. In vitro interference of tigecycline at subinhibitory concentrations on biofilm development by enterococcus faecalis. *Journal of antimicrobial chemotherapy*, 67(5):1155–1158, 2012.

[81] Aaron MT Barnes, Katie S Ballering, Rachel S Leibman, Carol L Wells, and Gary M Dunny. Enterococcus faecalis produces abundant extracellular structures containing dna in the absence of cell lysis during early biofilm formation. *MBio*, 3(4):e00193–12, 2012.

[82] Tiane Martin de Moura, Fabrício Souza Campos, Juliana Caierão, Ana Claudia Franco, Paulo Michel Roehe, Pedro Alves d'Azevedo, Jeverson Frazzon, and Ana Paula Guedes Frazzon. Influence of a subinhibitory concentration of vancomycin on the in vitro expression of virulence-related genes in the vancomycin-resistant enterococcus faecalis. *Revista da Sociedade Brasileira de Medicina Tropical*, 48(5):617–621, 2015.

[83] Julian Davies, George B Spiegelman, and Grace Yim. The world of subinhibitory antibiotic concentrations. *Current opinion in microbiology*, 9(5):445–453, 2006.

[84] Luisa Laureti, Ivan Matic, and Arnaud Gutierrez. Bacterial responses and genome instability induced by subinhibitory concentrations of antibiotics. *Antibiotics*, 2(1):100–114, 2013.

[85] Hannah R Meredith, Allison J Lopatkin, Deverick J Anderson, and Lingchong You. Bacterial temporal dynamics enable optimal design of antibiotic treatment. *PLoS Comput Biol*, 11(4):e1004201, 2015.

[86] Cheemeng Tan, Robert Phillip Smith, Jaydeep K Srimani, Katherine A Riccione, Sameer Prasada, Meta Kuehn, and Lingchong You. The inoculum effect and band-pass bacterial response to periodic antibiotic treatment. *Molecular Systems Biology*, 8(1), 2012.

[87] Jason Karslake, Jeff Maltas, Peter Brumm, and Kevin B Wood. Population density modulates drug inhibition and gives rise to potential bistability of treatment outcomes for bacterial infections. *PLoS Comput Biol*, 12(10):e1005098, 2016.

[88] Fernanda L Paganelli, Rob J Willems, and Helen L Leavis. Optimizing future treatment of enterococcal infections: attacking the biofilm? *Trends in microbiology*, 20(1):40–49, 2012.

[89] Mira Okshevsky, Viduthalai R Regina, and Rikke Louise Meyer. Extracellular dna as a target for biofilm control. *Current opinion in biotechnology*, 33:73–80, 2015.

[90] Eshel Ben-Jacob. From snowflake formation to growth of bacterial colonies ii: Cooperative formation of complex colonial patterns. *Contemporary Physics*, 38(3):205–241, 1997.

[91] Elena O. Budrene and Howard C. Berg. Complex patterns formed by motile cells of escherichia coli. *Nature*, 349, 1991.

[92] James A. Shapiro. The significances of bacterial colony patterns. *BioEssays*, 17(7):597–607, Mar 1995.

[93] Eshel Ben-Jacob, Inon Cohen, Ido Golding, David L. Gutnick, Marianna Tcherpakov, Dirk Helbing, and Ilan G. Ron. Bacterial cooperative organization under antibiotic stress. *Physica A*, 282:247–282, Feb 2000.

[94] R. Tyson, S. R. Lubkin, and J. D. Murray. A minimal mechanism for bacterial pattern formation. *Proc. R. Soc. Lond. B*, 266:299–304, 1999.

[95] Eshel Ben-Jacob, Ofer Schochet, Adam Tenenbaum, Inon Cohen, Andras Czirok, and Tamas Vicsek. Generic modelling of cooperative growth patterns in bacterial colonies. *Nature*, 368:46–49, Mar 1994.

[96] Andrey A. Polezhaev, Ruslan A. Pashkov, Alexey I. Lobanov, and Igor B. Petrov. Spatial patterns formed by chemotactic bacteria escherichia coli. *Int. J. Dev. Biol.*, 2006.

[97] Eugene A Yurtsev, Hui Xiao Chao, Manoshi S Datta, Tatiana Artemova, and Jeff Gore. Bacterial cheating drives the population dynamics of cooperative antibiotic resistance plasmids. *Molecular Systems Biology*, 9(683), 2013.

[98] Robin A. Sorg, Leo Lin, G. Sander van Doorn, Moritz Sorg, Joshua Olson, Victor Nizet, and Jan-Willem Veening. Collective resistance in microbial communities by intracellular antibiotic deactivation. *PloS Biology*, Dec. 2016.

[99] William P. J. Smith, Yohan Davit, James M. Osborne, Wook Kim, Kevin R. Foster, and Joe M. Pitt-Francis. Cell morphology drives spatial patterning in microbial communities. *PNAS*, pages 280–286, Dec. 2016.

[100] Motoo Kimura and George H. Weisss. The stepping stone model of population structure and the decrease of genetic correlation with distance. *Genetics*, 49:561–576, April 1964.

[101] R A Blythe and A J McKane. Stochastic models of evolution in genetics, ecology and linguistics. *Journal of Statistical Mechanics: Theory and Experiment*, 2007, July 2007.

[102] K. S. Korolev, Mikkel Avlund, Oskar Hallatschek, and David R. Nelson. Genetic demixing and evolution in linear stepping stone models. *Reviews of Modern Physics*, 82, May 2010.

[103] Kirill S. Korolev, Joao B. Xavier, David R. Nelson, and Kevin R. Foster. A quantitative test of population genetics using spatiogenetic patterns in bacterial colonies. *the american naturalist*, 178(4), Oct. 2011.

[104] Maxim O. Lavrentovich, Kirill S. Korolev, and David R. Nelson. Radial domany-kinzel models with mutation and selection. *Physical Review E*, 87, 2013.

[105] Irit Levin-Reisman, Ofer Fridman, and Nathalie Q. Balaban. Scanlag: High-throughput quantification of colony growth and lag time. *Journal of Visualized Experiments*, July 2014.

[106] Jordi van Gestel, Franz J Weissing, Oscar P Kuipers, and Akos T Kovacs. Density of founder cells affects spatial pattern formation and cooperation in bacillus subtilis biofilms. *International Society for Microbial Ecology*, 8:2069–2079, April 2014.

[107] Irit Levin-Reisman, Orit Gefen, Ofer Fridman, Irine Ronin, David Shwa, Hila Sheftel, and Nathalie Q Balaban. Automated imaging with scanlag reveals previously undetectable bacterial growth phenotypes. *Nature Methods*, 7(9), Sept. 2010.

[108] Daniel F. Sahm, Jessica Kissinger, Michael S. Gilmore, Patrick R. Murray, Ross Mulder, Joanne Solliday, and Barbara Clarke. In vitro susceptibility studies of vancomycin-resistant enterococcus faecalis. *Antimicrobial Agents and Chemotherapy*, 33(9):1588–1591, Sept. 1989.

[109] Olga G. Gold, H.V. Jordan, and J. van Houte. The prevalence of enterococci in the human mouth and their pathogenicity in animal models. *Archs oral Biol.*, 20:473–477, 1975.

[110] M. S. Guyer, R. R. Reed, J. A. Steitz, and K. B. Low. Identification of a sex-factor-affinity site in e. coli as . *Cold Spr. Harb. Symp. Quant. Biol.*, 45, 1981.

[111] Subach OM, Cranfill PJ, Davidson MW, and Verkhusha VV. An enhanced monomeric blue fluorescent protein with the high chemical stability of the chromophore. *PLoS One*, 6(12), Dec. 2011.

[112] Dan Drecktrah, Seamus Levine-Wilkinson, Tapen Dam, Seth Winfree, Leigh A Knodler, Trina A Schroer, and Olivia Steele-Mortimer. Dynamic behavior of salmonella-induced membrane tubules in epithelial cells. *Traffic*, 9:2117–2129, Dec. 2008.

[113] Simone Aymanns, Stefanie Mauerer, Ger van Zandbergen, Christiane Wolz, and Barbara Spellerberg. High-level fluorescence labeling of gram-positive pathogens. *PLoS One*, 6(6), June 2011.

[114] Karen K. Zscheck and Barbara E. Murray. Nucleotide sequence of the beta-lactamase gene from enterococcus faecalis hh22 and its similarity to staphylococcal beta-lactamase genes. *Antimicrobial Agents and Chemotherapy*, 35(9):1736–1740, Sept. 1991.

[115] Elke Peeters, Hans J. Nelis, and Tom Coenye. Comparison of multiple methods for quantification of microbial biofilms grown in microtiter plates. *Journal of Microbiological Methods*, 72:157–165, 2008.

[116] George A. O'Toole. Microtiter dish biofilm formation assay. *Journal of Visualized Experiments*, 2011.

[117] Ben Langmead, Cole Trapnell, Mihai Pop, and Steven L Salzberg. Ultrafast and memory-efficient alignment of short dna sequences to the human genome. *Genome Biology*, 2009.

[118] Heng Li, Bob Handsaker, Alec Wysoker, Tim Fennell, Jue Ruan, Nils Homer, Gabor Marth, Goncalo Abecasis, Richard Durbin, and 1000 Genome Project Data Processing Subgroup. The sequence alignment/map format and samtools. *Bioinformatics*, pages 2078–2079, 2009.

[119] Cole Trapnell, David Hendrickson, Martin Sauvageau, Loyal Goff, John L. Rinn, and Lior Pachter. Differential analysis of gene regulation at transcript resolution with rna-seq. *Nature Biotechnology*, pages 46–53, 2012.

[120] L. Goff, C. Trapnell, and D. Kelley. cummerbund: Analysis, exploration, manipulation, and visualization of cufflinks high-throughput sequencing data. *R package version 2.14.0*, 2013.

[121] Tim Hulsen, Jacob de Vlieg, and Wynand Alkema. Biovenn – a web application for the comparison and visualization of biological lists using area-proportional venn diagrams. *BMC Genomics*, 2008.